UNIVERSIDADE TÉCNICA DE LISBOA

INSTITUTO SUPERIOR TÉCNICO

2D PHASE UNWRAPPING VIA GRAPH CUTS

Gonçalo Ramiro Valadão Matias

Dissertação para obtenção do Grau de Doutor em
Engenharia Electrotécnica e de Computadores

DOCUMENTO PROVISÓRIO

Julho 2011

Acknowledgments

My first words of gratitude go to my supervisor, Prof. José Bioucas-Dias, for whose guidance, support, and incentive to always excel myself I will always be indebted. I also would like to thank Prof. Mário Figueiredo and Prof. Pedro M. Q. Aguiar for being members of my thesis commitee.

During my studies I met a lot of people, from whom I would like to emphasize my lab mates at Instituto de Telecomunicações: André, Hugo (both of them), João, José and Marta.

I would like to thank my friend and lab mate João for a lot of remarkable moments.

I also thank many other friends, namely: Vasco, Filipa, Nuno, Lena, Padre João, Fechi, João, Paulo, Isabel and many more.

To my parents, my brothers, and my parents-in-law I would like to thank for all the unconditional support.

Finally my greatest thanks goes to my family: Mónica, Mariana, and Francisco, you've made this a beautiful adventure.

This work was supported in part by Fundação para a Ciência e Tecnologia (FCT) through a PhD scholarship, and by Instituto de Telecomunicações through a scholarship in the last stage of the PhD studies.

Abstract

Phase imaging technologies such as interferometric synthetic aperture radar (InSAR), magnetic resonance imaging (MRI), or optical interferometry, are nowadays widespread and with an increasing usage. The so-called *phase unwrapping*, which consists in the inference of the absolute phase from the modulo-2π phase, is a critical step in many of their processing chains, yet still one of its most challenging problems. We introduce an *energy minimization* based approach to 2D phase unwrapping. In this approach we address the problem by adopting a Bayesian point of view and a Markov random field (MRF) to model the phase. The *maximum a posteriori* estimation of the absolute phase gives rise to an integer optimization problem, for which we introduce a family of efficient algorithms based on existing *graph cuts* techniques. We term our approach and algorithms PUMA, for Phase Unwrapping MAx flow. As long as the prior potential of the MRF is convex, PUMA guarantees an exact global solution. In particular it solves exactly all the minimum L^p norm ($p \geq 1$) phase unwrapping problems, unifying in that sense, a set of existing independent algorithms. For non convex potentials we introduce a version of PUMA that, while yielding only approximate solutions, gives very useful phase unwrapping results. The main characteristic of the introduced solutions is the ability to blindly preserve discontinuities. Extending the previous versions of PUMA, we tackle denoising by exploiting a multi-precision idea, which allows us to use the same rationale both for phase unwrapping and denoising. Finally, the last presented version of PUMA uses a *frequency diversity* concept to unwrap phase images having large phase rates. A representative set of experiences illustrates the performance of PUMA.

Keywords: phase unwrapping; Markov random fields; energy minimization; graph cuts; image processing; computer vision.

Resumo

Tecnologias de imagem de fase, tais como, interferometria com radar de abertura sintética, imagem de ressonância magnética, ou interferometria óptica, estão, hoje em dia, popularizadas. O *desenrolamento de fase*, que consiste na inferência da fase absoluta a partir da fase modulo-2π, é um passo crítico em muitas das suas cadeias de processamento e, no entanto, constitui ainda um dos seus problemas mais difíceis. Nesta tese introduzimos uma abordagem ao problema do desenrolamento de fase 2D, com base em *minimização de energia*. Abordamos este problema adoptando um ponto de vista bayesiano e um campo aleatório de Markov para modelar a fase. A estimativa *maximum a posteriori* da fase absoluta dá origem a um problema de optimização inteira, para o qual introduzimos uma família de algoritmos eficientes com base em técnicas de cortes em grafos. À abordagem e algoritmos introduzidos damos colectivamente o nome de PUMA (Phase Unwrapping MAx flow). Desde que o potencial do campo de Markov seja convexo, o PUMA garante uma solução global exacta. Em particular resolve exactamente todos os problemas de desenrolamento de fase da família mínima norma L^p ($(p \geq 1)$). Para potenciais não convexos introduzimos uma versão do PUMA que, embora fornecendo um algoritmo aproximado, produz bons resultados de desenrolamento de fase. A característica principal das soluções introduzidas é a capacidade de preservar descontinuidades de forma cega. Outra extensão introduzida no PUMA reside no atacar do problema da filtragem de ruído, recorrendo a uma ideia de multi-precisão. Esta permite-nos utilizar o racional desenvolvido para o desenrolmento de fase na filtragem de ruído. Finalmente, a última variante apresentada do PUMA emprega o conceito de *diversidade na frequência*, o qual garante a possibilidade de desenrolar imagens de fase contendo gradientes elevados. Um conjunto representativo de experiências ilustra o desempenho do PUMA em cada uma das suas variantes.

Palavras chave: desenrolamento de fase; campos aleatórios de Markov; minimização de energia; cortes em grafos; processamento de imagem; visão por computador.

Table of Contents

List of Figures

List of Tables

Chapter 1

Introduction

This thesis proposes an approach to 2D phase unwrapping (PU), by adopting a Bayesian modeling, using an energy minimization criterion, and introducing a family of graph cuts based algorithms.

1.1 Prelude

1.1.1 Phase imaging

Phase images are nowadays used in a myriad of applications and produced by a wide range of techniques from which the prototype is optical interferometry. In fact, the wave nature of light was demonstrated by Thomas Young with the famous double slit experiment held in 1801 [15]. The phase image then produced, by the interference between crests and troughs, led to a deeper understanding of light. Since then, several *coherent* remote sensing devices have been used to solve innumerable scientific and engineering problems: the basic idea is to measure the coherence between emitted and scattered waves, in order to get geometrical and physical information about the illuminated scenes.

1.1.2 Portfolio of applications

Next we make a very quick browse through some of the most representative coherent phase imaging techniques and applications.

Figure 1.1: Arteriography of the brain. Image courtesy of GE Medical Systems.

Magnetic resonance imaging (MRI)

Clinicians use MRI phase images with several goals: *e.g.*, to make real time thermometry which is crucial in tumor thermo-ablation to mitigate the death of healthy tissues [33]; to make venography [85] or arteriography (see Figure 1.1); to make water/fat separation [90]: this allows quantitative imaging of fat which is useful, *e.g.*, in obesity studies.

Interferometric Synthetic Aperture Radar (InSAR)

InSAR imaging comprises an ensemble of techniques that provide measurements on ground surface topography and deformation. Regarding topography, InSAR generated digital elevation models (DEM) are these days widely employed, the most famous of which is the one obtained by SRTM [(Space) Shuttle Radar Topography Mission]. In February of 2000, during ten days only, SRTM covered most of the Earth surface, yielding a global DEM with 30 m spatial sampling, and 16 m vertical and 20 m horizontal absolute accuracy (90%)[1]. Airborne techniques achieve far more detailed DEMs (however for far smaller areas) with standard commercial available sub-meter accuracy and few meters spacing [75]. Regarding deformation mapping, more recent techniques like (spaceborne based) Permanent Scatterers InSAR (PSInSAR) [39] are able to detect deformations with rates of the order of 1 mm/year. See Figure 1.2.

[1]For accuracy definitions see, *e.g.*, [25].

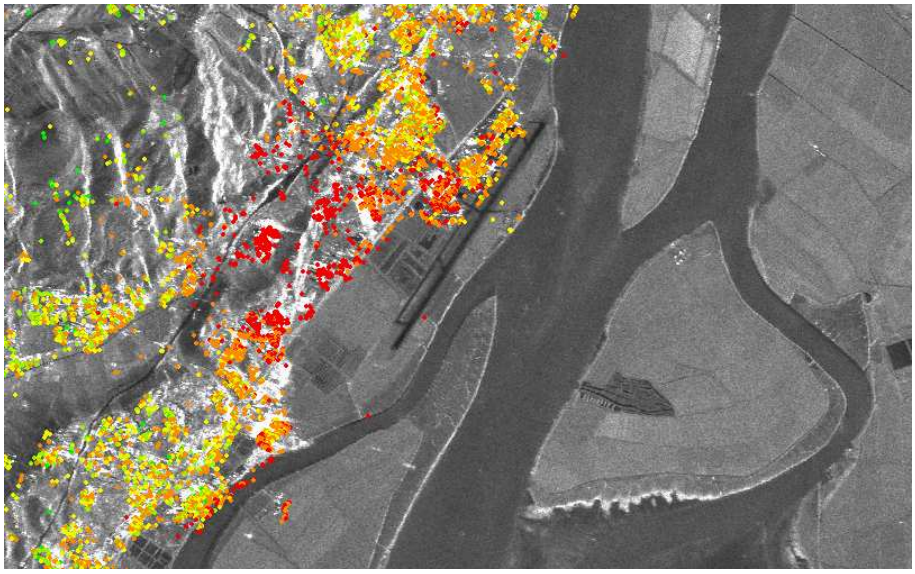

Figure 1.2: Permanent scatterers near Lisbon, Portugal. Color, from red to green, encodes the deformation rate (−10 to 10 millimeters per year, respectively). Image courtesy of Tele-Rilevamento Europa.

Other

Phase imaging is at the core of many other applications and techniques, namely, diffraction tomography, adaptive optics, surface profiling, deformation and vibration measurements, non destructive testing of components and optical quadrature microscopy [35, 82, 87].

1.2 Who cares about *phase unwrapping*?

The vast majority of the above mentioned methods, most of the time, do not measure the phase but only its *modulo*-2π value (2π by considering that the phase is measured in radians). In other words, these phase imaging techniques only measure the remainder of the division of the phase by 2π, the so-called *wrapped* phase. Yet, the physical meaning is attached to the *absolute* phase (we use the term absolute phase to distinguish from wrapped phase). The inference of the absolute phase images from the wrapped ones is known as the 2D *phase unwrapping* problem, which is, then, crucial in many technologies.

1.3 This thesis

1.3.1 Addressed problem

This thesis addresses the 2D phase unwrapping problem (for simplicity we shall drop hereafter the "2D" prefix). We consider a Bayesian formulation having a prior given by a first-order Markov random field (MRF), and an observation mechanism characteristic of many applications for which phase unwrapping is needed. The inference of the absolute phase, given by the *maximum a posteriori* (MAP), is formulated as a discrete energy minimization problem. This energy minimization constitutes the main problem to be addressed by this thesis. Subsidiary topics such as phase denoising, frequency diversity to enhance phase unwrapping, and blind edge preservation are tackled under the same framework.

1.3.2 Motivation

The major motivation for the work in this thesis was the state-of-the-art results, obtained by Bioucas-Dias and Leitão, with the absolute phase estimation algorithm $\mathbb{Z}\pi$M [36]. In that work the authors adopt a Bayesian viewpoint, with a prior for the absolute phase given by a (first-order) Gaussian Markov random field (GMRF). This leads to a phase unwrapping operation (the $\mathbb{Z}$ step), that consists of solving a discrete quadratic optimization problem. In spite of being quadratic, the simple fact of dealing with discrete variables makes of it a very demanding problem, for which the authors propose an exact (and polynomial-time) algorithm based on network programming techniques (furthermore, generally, the operation deals with a large number of variables given by the number of pixels in the phase image).

The fruitfulness of the above mentioned work made "mandatory" the prosecution of further research on phase unwrapping in the same *Bayesian formulation with prior given by a Markov random field* plus *discrete optimization* vein. This is the theme of this thesis.

1.3.3 Our path

The biggest methodological innovation in our approach consists, in our opinion, in bringing graph cuts [19] into the phase unwrapping formulation. Graph cuts techniques have been being, during the last decade, largely employed in several research fields (specially in vision and image processing) which require the solution of high dimensional discrete opti-

mization problems, namely for inference on MRFs. At the very basic level the ideas of our proposed algorithms and the phase unwrapping step of $\mathbb{Z}\pi$M are alike: to solve the formulated discrete optimization problem through a sequence of binary optimizations. However, instead of solving each binary optimization through network programming methods, we employ graph cuts. These are very well suited to solve binary optimization problems (but, by no means, not only) [67].

The use of graph cuts has great impacts. Perhaps the most immediate which we have found is that, unlike the formulation of $\mathbb{Z}\pi$M, we have immediate flexibility on the type of MRFs that we can use. As detailed in Section 3.1, the Bayesian formulation leads us to minimize a so-called *energy* function. We found that our algorithm guarantees a global energy minimum in pseudo polynomial time [1], as long as the MRF potential, which governs the interactions between pairs of interacting variables (we are considering a first-order MRF), is *any* convex function ($\mathbb{Z}\pi$M considers a quadratic potential). This fact alone yields a family of algorithms, in the sense of family of parameterizations of the algorithm that, for instance, solve any minimum L^p norm phase unwrapping problem. See Chapter 2 for a definition of this problem.

In image restoration non-convex potentials have been used with success to preserve edges [16]. In phase unwrapping, edges also play an important role (see next section) and, accordingly, we modified the original algorithm to include these type of potentials (Chapter 4). The resulting algorithm is approximate in nature, which is all that we can expect in this regime, in face of the local minima brought by non convexity (excluding exponential time algorithms such as simulated annealing [45]). The experiments with which we have tested it, have systematically shown state-of-the-art competitive or even state-of-the-art results, with the particularity of being capable of edge preservability without prior information on the edges (some more comments on this in the next section). These results mean that the devised algorithm systematically finds good energy local minima. To our knowledge there is in the literature one previous method that also employs non convex potentials in order to preserve edges [86]. We should mention, however, that it demands a set of parameters to be tuned. Furthermore we make a comparison between our algorithm and that one in a representative experiment illustrated in Chapter 4.

A third distinctive trait of our approach is a denoising procedure (Chapter 5) also based on the same graph cuts based discrete optimization rationale. Our idea consists of sequentially reducing the precisions (the steps) with which we make the variables change,

in the energy minimization task. When one precision no longer allows energy decreasing we change into a smaller one. While this greedy method might sound a bit naive, it is justified by the state-of-the-art competitive results that yields. Unlike traditionally in the phase unwrapping field, we employ denoising only after the unwrapping step. This is made possible thanks to the previous described edge preservation capability which, in particular, allows the existing noise not to compromise the unwrapping procedure. Conversely, not making the denoising step before phase unwrapping has the great benefit of avoiding the denoising to destroy, as a collateral effect, phase information relevant for a proper unwrapping.

Finally, we also adopted into our method a frequency diversity technique. Phase images having high phase rates may compromise the unwrapping task (see Chapter 2). An ingenious and simple technique, used in some fields like Radar signal processing [80], which is called frequency diversity, allows to solve an identical problem. The foundation of the technique can be found in the chinese remainder theorem [59] from which we can, given some assumptions, guess a number given its remainders from the divisions by two other numbers specially chosen. To our knowledge the existing phase unwrapping literature adopting phase diversity is very scarce (Chapter 6). Furthermore, those existing works devise algorithms which, in our opinion, are too simplistic or employ optimization methods like simulated annealing, which are inadequate to the problem by consuming too much time. Again we use graph cuts to implement the algorithm.

For the reasons that were sustained before we, hereafter, shall refer to our method as an energy minimization approach to the phase unwrapping problem.

1.3.4 Motivation *a posteriori*

In the strict sense phase unwrapping is an impossible problem, as to a certain wrapped phase value there correspond an infinite number of possible absolute phase values. In mathematical parlance, this fact translates into phase unwrapping being an ill-posed problem [56]. To work around this fact, and achieve phase unwrapping, some extra information or assumption is required.

It does not take much imagination to assume that some kind of relation might exist between neighbouring pixels. Namely, in the Bayesian formulation the interactions between pixels are governed by a potential and, generally for every formulation, its assumed that in principle, neighboring pixels's absolute phases do not differ by *too much*. In fact,

this assumption is present, more or less explicitly, in all approaches to phase unwrapping under the name of *Itoh condition*, where by *too much* it is intended, exactly, more than π rad. This condition ensures the annihilation of the intrinsic ambiguity present in the wrapped phase values, in the sense that if two neighbors's absolute phases do not differ by more than π, then we can unambiguously tell the absolute phase in one of them given the absolute phase in the other. We will refer to some other arising complications in Chapter 2, when describing certain methods that explicitly lay upon the Itoh condition.

What if in fact the Itoh condition does not apply, and the difference between the absolute phases of two neighboring pixels differs by more than π? In fact, what if such a kind of bad behaved phase difference happens not only between two pixels, but along many other neighboring pairs of pixels defining a curve along some part of the image? This scenario is in fact very much common in real world images, where these *discontinuity* edges are due to boundaries of objects or, generically, regions having some relevant (to the phase images) characteristic (like, *e.g.*, height in InSAR). We can guess that it is likely that a phase unwrapping algorithm will tend to behave poorly around discontinuities. In fact, that is the case for the streamline state-of-the-art or otherwise noteworthy algorithms. However, we have found that our approach tends to behave well, specially while employing non-convex potentials. In Figure 1.3 we illustrate this with an extremely hard phase unwrapping problem. The 3-D mesh of the original phase image corresponds to two intertwined spirals. Such an image has a lot of discontinuities, which induces a very hard phase unwrapping problem. Figure 1.3 (a) shows the corresponding wrapped phase image and Figure 1.3 (b) shows the unwrapped image with Figure 1.3 (c) displaying its 3-D mesh. To our knowledge no other algorithm is able to solve this phase unwrapping problem. To do that other algorithms require that the user feeds in information about the localization of the discontinuities, otherwise the solution will not preserve them. On the contrary, the algorithm proposed in this thesis has the capability of blindly preserve discontinuities, specially while working with non-convex potentials.

This result alone is, in our opinion, one of the nicest features of the presented approach, and justifies the efforts made to accomplish this work.

1.3.5 Energy minimization

In this work we approach the phase unwrapping problem as a labeling task on a 2D grid, where sites in the grid correspond to the image pixels. The label we assign to each site

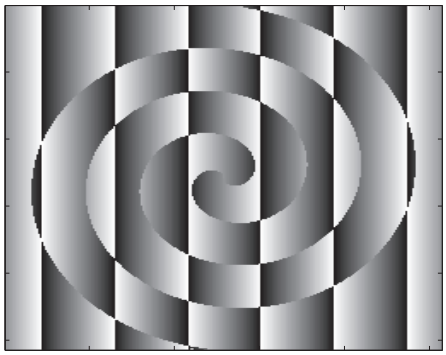

(a)

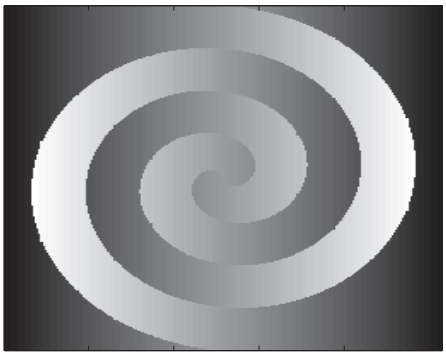

(b)

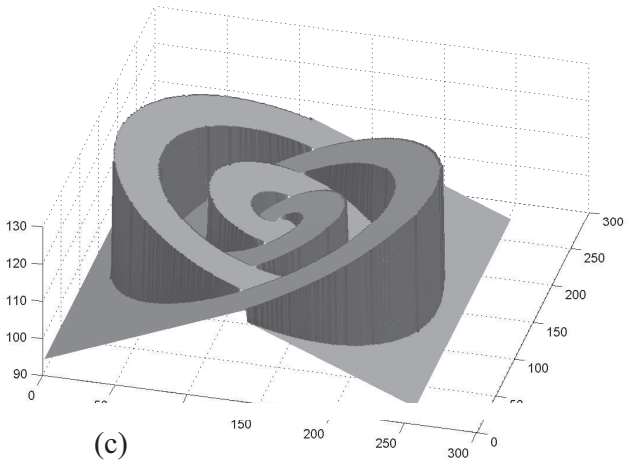

(c)

Figure 1.3: Extremely hard phase unwrapping problem. (a) Wrapped phase image. (b) Unwrapped image. (c) 3-D mesh of the unwrapped image.

corresponds to the estimate quantity that should be added to the respective wrapped phase, in order to obtain the absolute phase. By adopting a Bayesian formulation in which the prior probability for the absolute phase is given by a Markov random field (over the same grid), the *maximum a posteriori* (MAP) estimate for the absolute phase is given by an *energy minimization* [6, 45]. This energy is made of two terms: a data term which penalizes inconsistency between the observed and the estimated phases, and a smooth term which encodes some type of smoothness between the phase of neighboring pixels. More precisely, by defining l to be a labeling, *i.e.*, the set of labels assigned to every pixel p, the energy is:

$$E = E_{data}(l) + \lambda E_{smooth}(l), \tag{1.1}$$

where λ is the so-called regularization parameter that sets the balance between the data term and the smooth term and, defining l_p to be the label of pixel p, we have:

$$E_{data}(l) = \sum_p d_p(l_p),$$

d_p being a data cost for pixel p, and

$$E_{smooth}(l) = \sum_{\{p,q\}\in\mathcal{N}} V_{pq}(l_p, l_q),$$

where $\mathcal{N}$ is the set of all pairs of neighboring pixels (adjacent horizontal and vertical pairs, in our case), and V is the prior potential defined by the Markov random field, penalizing somehow non-smoothness. In our particular case, furthermore, the data term is given by the cosine of the difference between absolute and wrapped phases.

To the above described minimization problem we still add the knowledge that the difference between wrapped and absolute phases is a multiple of 2π. This has two immediate consequences: first the energy turns out to be discrete (in multiples of 2π); second, the data term evaluates to zero as it is, in our case, given by the cosine of the difference between absolute and wrapped phases. We are led to a high dimensional discrete optimization problem (the dimension is the number of pixels, which can be millions) which is, then, usually a hard task.

Energy minimization is considered in several different fields, particularly in computer vision where it proofs to be very powerful and elegant. There, it has been employed in many applications, *e.g.*, image restoration [45, 6], surface reconstruction [14], stereo matching [3], image denoising, segmentation, inpainting and stitching [92], video segmentation [78]

and face matching [2]. The adoption of energy minimization in computer vision was hampered by the lack of powerful enough optimization techniques to efficiently perform it. For many years, the methods of choice were mainly Iterated Conditional Modes (ICM) [6] and simulated annealing [65, 45], which have shown lack of efficiency [92]. As referred in [79], by the beginning of this century a few papers, including namely [61, 17, 20], brought the attention of the computer vision community to the graph cuts techniques, and its extremely efficient performance in energy minimization for computer vision applications (the seminal work using graph cuts for vision had been published more than a decade before [54]). In this work we also propose a graph cuts based set of algorithms to approach our energy minimization, in order to achieve phase unwrapping. In fact, the algorithms which we propose have a close relation with certain energy minimization algorithms in computer vision. We will now briefly refer to this.

Exact algorithm

In Chapter 3 we propose an algorithm to solve the above described energy minimization problem, with the potential V being an arbitrary convex function. As in many applications in vision, the smoothness energy term involves a function which depends on the difference of labels at neighboring pixels: $V_{pq}(l_p, l_q) = V_{pq}(l_p - l_q)$ as a way to somehow penalize big differences between labels of adjacent pixels. This algorithm is exact, has pseudo polynomial complexity [1] and is fast (see Chapter 3). By the time we developed our work, another approach to exact energy minimization was independently developed by Jérôme Darbon and Marc Sigelle [31, 28], by also using graph cuts and by using level sets techniques. In that work the authors consider the existence of a convex data term, which in our approach is also straightforward to consider if we like, and for the potential V in the smoothness term, the potential V is considered to be the (non isotropic) total variation. This energy is clearly more restrictive than ours. In that work, the authors illustrate the power of the approach, by making image denoising considering an energy having an L^2 data term (it represents the square of the difference between the data and the optimal solution) and (non isotropic) TV smoothness term, where TV means the total variation of the optimal solution (total variation has been conjectured to be a good image model since seminal work of Rudin [89] and Rudin, Osher, and Fatemi [68]). This implicitly qualifies our algorithm to also perform that kind of image denoising.

Rather than considering the L^2 as the data term, in our phase unwrapping problem

we know that it is given by a cosine. More precisely, as already referred, the cosine of the difference between the observed and the estimated phases. Thus being, to make denoising, we devised a procedure of going on with the energy minimization by searching for the unwrapped phase with increasing submultiples of 2π, until a certain stopping precision. By, thus, increasing the precision of the steps in the minimization, we expect to make denoising, and so it happens with all the experiments we performed. Obviously, having a data term which is non convex goes out of the scope of our proposed algorithm. To cope with that, we have devised an approximate version of it. We should refer that after we have developed and published our approximate version of the algorithm, two other approaches were published by Vladimir Kolmogorov [66] and by Jérôme Darbon [30] (Darbon published a previous not so powerful result in [29]), which propose efficient global energy minimizers valid as long as the potential V is convex. The main advancement consists of allowing any data term (be it convex or not).

Approximate algorithm

Although we might employ one of the last two cited algorithms to implement the above referred denoising (which uses the non convex data term), the challenge of making phase unwrapping that preserves discontinuities (preserves boundaries of regions) led us to consider discontinuity preserving potentials which, in particular, are non convex [55, 93]. Many of the energy minimization applications in vision also require a non convex potential. Such minimization problems are known to be extremely difficult to solve exactly. In fact, even for one of the simplest non-convex potentials, given by the Potts model, the optimization turns out to be NP-hard [20]. In this thesis we propose an approximate algorithm which is a modification of the exact one, and relies, basically, on a maximization-minimization approach and the enlargement of the moves employed. The phase unwrapping results prove to be state-of-the-art competitive, being sometimes the state-of-the-art. We plan in the future to evaluate the performance of the algorithm in some computer vision problems namely stitching, inpainting, denoising, stereo matching and object recognition.

1.4 Contributions

List of papers

The following papers, which substantiate this thesis, were published in reviewed journals and conferences:

Journal

1. G. Valadão and J. Bioucas-Dias, "CAPE: Combinatorial Absolute Phase Estimation", Journal of the Optical Society of America A (Optics, Image Science and Vision). September 2009 (pp. 2093 - 2106) [96].

2. J. Bioucas-Dias and G. Valadão, "Phase Unwrapping via Graph Cut", IEEE Transactions on Image Processing, March 2007 (pp. 698 - 709) [11].

Conference

3. J. Bioucas-Dias and G. Valadão, "Multifrequency Absolute Phase Estimation via Graph Cuts", in Proceedings of the 17th European Signal Processing Conference - EUSIPCO2009, Glasgow, Scotland, August 24-28, 2009 [13].

4. G. Valadão and J. Bioucas-Dias, "Phase Imaging: Unwrapping and Denoising with Diversity and Multi-Resolution", in Proceedings of the 7th Conference on Telecommunications, ConfTele2009, Santa Maria da Feira, Portugal, May, 2009 [97].

5. G. Valadão and J. Bioucas-Dias, "Phase Imaging: Unwrapping and Denoising with Diversity and Multi-Resolution", in Proceedings of the 2008 International Workshop on Local and Non-Local Approximation in Image Processing, LNLA 2008, Lausanne, Switzerland, August 23-24, 2008 [98].

6. J. Bioucas-Dias and G. Valadão, "Phase Unwrapping via Diversity and Graph Cuts", in Proceedings of the IWSSIP 2008 (15th International Workshop on Signals, Systems and Image Processing), Bratislava, Slovak Republic, June 25- 28 [12].

7. G. Valadão and J. Bioucas-Dias, "PUMA: Phase Unwrapping via Max flows", in Proceedings of the 6th Conference on Telecommunications, ConfTele2007, Peniche, Portugal, May, 2007 [95].

8. J. Bioucas-Dias and G. Valadão, "Discontinuity Preserving Phase Unwrapping using Graph Cuts", in proceedings of the Energy Minimization Methods in Computer Vision and Pattern Recognition EMMCVPR05, St. Augustine, U.S.A, Vol. 1, pp. 268-284, November, 2005 [8].

9. J. Bioucas-Dias and G. Valadão, "Phase Unwrapping: a New Max-flow/Min-cut Based Approach", in Proceedings of the IEEE International Conference on Image Processing - ICIP2005, Genova, Italiy, September, 2005 [9].

10. J. Bioucas-Dias and G. Valadão, "Phase Unwrapping via Graph Cuts", in Proceedings of the 2nd Iberian Conference on Pattern Recognition and Image Analysis - IbPRIA2005, Estoril, Portugal, 2005 [10].

11. G. Valadão and J. Bioucas-Dias, "Phase Unwrapping Via Graph Cuts", in Global Developments in Environmental Earth Observation from Space: 25th EARSEL Symposium, EARSEL2005, Porto, Portugal, June 2005 [94].

Next we list, synthetically, the major contributions of this thesis:

- A new approach to phase unwrapping [10, 94, 11].
- Unification of the minimum L^p norm, $p \geq 1$, phase unwrapping problems [9, 8, 95, 11].
- Proposal of approximate phase unwrapping algorithms able to consider non-convex potentials in the MRF [9, 8, 95, 11].
- Denoising procedure sharing the same discrete rationale of phase unwrapping [98, 97, 96].
- Frequency diversity phase unwrapping [12, 13].
- Development of algorithms that are interesting to other domains such as, *e.g.*, computer vision.

1.5 Dissertation outline

This dissertation is divided into seven chapters. Chapter 2 formulates the phase unwrapping problem, gives a brief overview of the main approaches to solving it, and makes reference to some state-of-the-art or otherwise outstanding algorithms. Following it, Chapter

3 establishes the (Bayesian) adopted modeling, and introduces our aproach, that we name PUMA, to phase unwrapping. Besides experimental results this chapter puts emphasis on theoretical and algorithmic issues. Subsequently, Chapter 4 presents the variant of PUMA that has the ability to blindly preserve discontinuities, and presents some experimental results and benchmarking. Then, Chapter 5 brings out the denoising version of PUMA, also showing some benchmarking and experimental results. Finally, Chapter 6 introduces frequency diversity illustrating it with experiences, and Chapter 7 succintly draws conclusions about the introduced approach setting some future research directions.

Figure 1.4 depicts the main logical interdependences between the chapters of the dissertation.

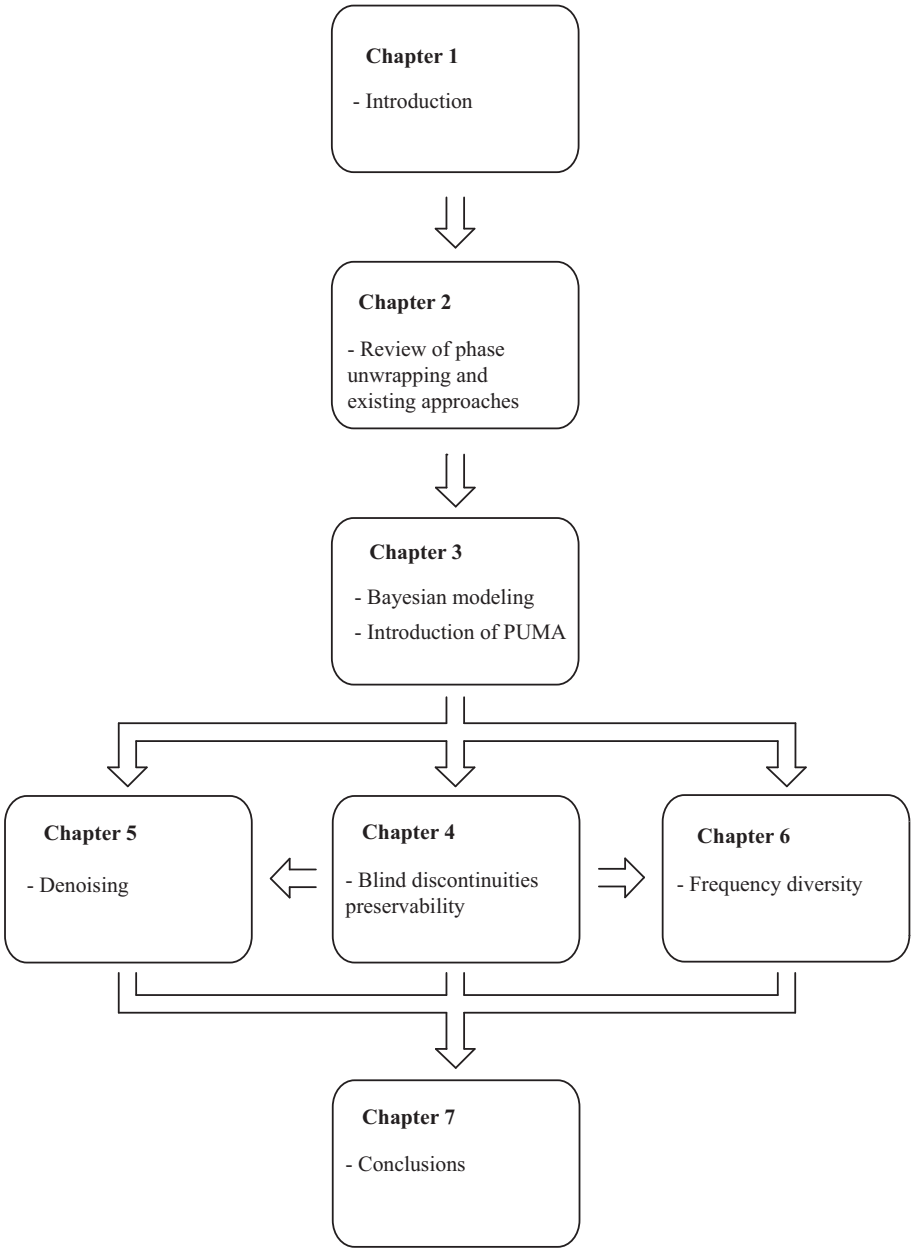

Figure 1.4: Thesis outline.

Chapter 2

Phase Unwrapping

We have alluded, in the previous chapter, to the plethora of instances where phase imaging sensors are only able to retrieve the wrapped phase instead of its absolute (*i.e.*, real) value [47, 49, 82, 91]. This makes phase unwrapping extremely important in the field of phase imaging technologies.

Putting it a bit more formal, let us define the wrapper operator $\mathcal{W}(\cdot)$ by

$$\begin{array}{rccc} \mathcal{W}: & \mathbb{R} & \longrightarrow & [0,\ 2\pi) \\ & \phi & \mapsto & \phi - 2\pi k, \end{array} \tag{2.1}$$

where $k \in \mathbb{Z}$ is such that $\phi - 2\pi k \in [0,\ 2\pi)$. Therefore, $\mathcal{W}$ is simply the modulo-2π operator. The inverse operation, *i.e.*, to get ϕ given $\phi - 2\pi k \in [0,\ 2\pi)$ constitutes the *phase unwrapping* problem. The variable ϕ is the *absolute phase*, which corresponds to some physical quantity that depends on the application, and $\phi - 2\pi k$ is the *wrapped phase*, which is the observed quantity. In this dissertation *phase* is a real variable with the usual physical meaning concerning the waves used in the imaging technique under consideration.

Alternatively, the wrapper operator is, very often, defined according to

$$\begin{array}{rccc} \mathcal{W}: & \mathbb{R} & \longrightarrow & [-\pi,\ \pi) \\ & \phi & \mapsto & \phi - 2\pi k, \end{array} \tag{2.2}$$

where $k \in \mathbb{Z}$ is such that $\phi - 2\pi k \in [-\pi,\ \pi)$. According to (2.2) operator $\mathcal{W}$, thus, wraps any phase ϕ into the *principal interval* $[-\pi,\ \pi)$ and, thus, it is in essence the modulo-2π operator. In what follows we will use both equivalent definitions (2.1) and (2.2); at each time, if relevant, the definition at use will be evident from context.

As previously mentioned, phase unwrapping is an ill-posed problem [56] as to a certain wrapped phase value there corresponds an infinite number of possible, in theory, abso-

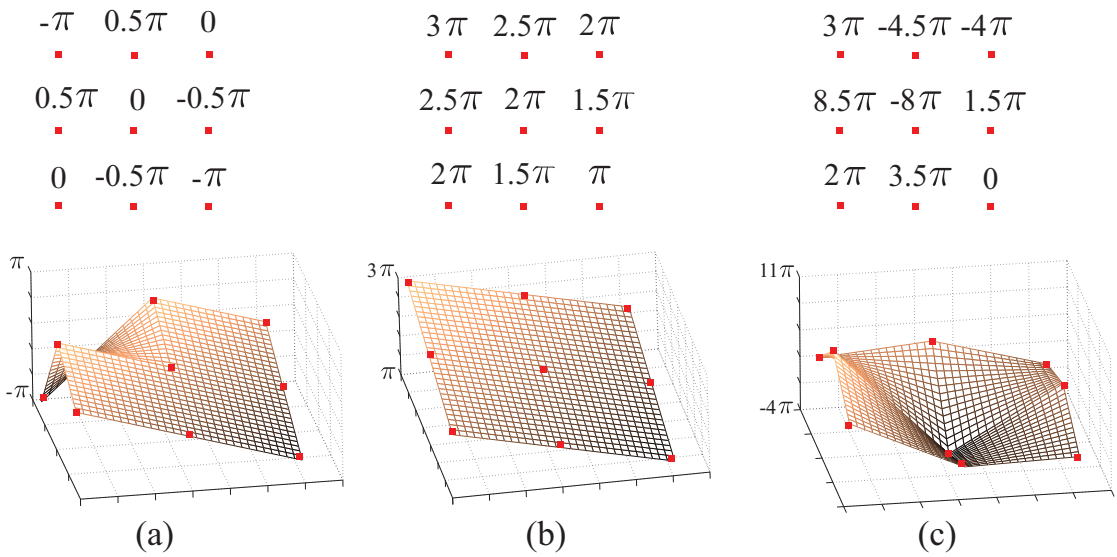

Figure 2.1: (a) Modulo-2π wrapped image and its mesh rendering. (b) Possible unwrapped solution and its mesh rendering. (c) A second possible unwrapped solution and its mesh rendering.

lute phase values. Figure 2.1 illustrates this lack of uniqueness intrinsic to unwrapping, by using a toy example employing 3×3 images. Figure 2.1 (a) shows a wrapped image, together with a corresponding mesh rendering. Figures 2.1 (b) and 2.1 (c) present two different possible corresponding unwrapped images, along with their mesh renderings which emphasize how different those solutions are. To overcome the ill-posedness of phase unwrapping, additional or *a priori* information is needed.

2.1 The Itoh Condition

The Itoh Method

An assumption taken by most phase unwrapping strategies, is that the absolute value of phase differences between neighbouring pixels is less than π rad, the so-called Itoh condition [62]. If this assumption is not violated, it eliminates the ill-posedness of the problem, allowing the absolute phase image to be easily determined up to a constant. Introducing some simple notation, let us consider a sequence $\{\phi_n\}$ of values of neighbouring pixels over an absolute phase image, and define a corresponding sequence of linear differences by

$$\Delta\phi_n = \phi_n - \phi_{n-1}. \tag{2.3}$$

Hereafter, ϕ will always be denoting an absolute (*i.e.*, unwrapped) phase, and ψ a wrapped phase; the Δ operator definition as a linear difference will hold, irrespective of phase being an absolute or a wrapped one.

The Itoh condition can be expressed as

$$|\Delta\phi_n| < \pi. \tag{2.4}$$

From (2.3), it comes immediately

$$\sum_{n=1}^{m} \Delta\phi_n = \phi_m - \phi_0, \tag{2.5}$$

as the intermediate sequence values cancel out each other. Now, from (2.2), we have $\mathcal{W}(\phi_n) = \phi_n - 2\pi k_n$ ($k_n \in \mathbb{Z}$) and so,

$$\Delta\mathcal{W}(\phi_n) = \phi_n - \phi_{n-1} - 2\pi(k_n - k_{n-1}), \tag{2.6}$$

where $k_n, k_{n-1} \in \mathbb{Z}$. We can, thus, introducing (2.3), write

$$\underbrace{\mathcal{W}\left[\Delta\mathcal{W}(\phi_n)\right]}_{a} = \Delta\phi_n \underbrace{-2\pi(k_n - k_{n-1}) - 2\pi k}_{b}, \tag{2.7}$$

where $k_n, k_{n-1}, k \in \mathbb{Z}$, and $2\pi k$ is the proper 2π multiple to bring a into the principal interval. From (2.4) and knowing that by definition $|a| \leq \pi$, we have necessarily $b = 0$, which allows us to write,

$$\mathcal{W}\left[\Delta\mathcal{W}(\phi_n)\right] = \Delta\phi_n. \tag{2.8}$$

Finally, introducing (2.8) into (2.5) we obtain:

$$\phi_m = \sum_{n=1}^{m} \mathcal{W}\left[\Delta\mathcal{W}(\phi_n)\right] + \phi_0, \tag{2.9}$$

which gives us a procedure for obtaining the unwrapped phase on any pixel, ϕ_m, from the wrapped phase values along any path linking that pixel to another, for which the absolute phase value, ϕ_0, is known: the Itoh method. By covering the image with a path, it allows us to unwrap an entire image up to a constant (the absolute phase value for one pixel in the image) given that the Itoh condition is satisfied (on the path).

A Smoothness Assumption

Again referring to Figure 2.1, the image in Figure 2.1 (b) clearly verifies the Itoh condition, while image in Figure 2.1 (c) does not. These two images correspond to very different

absolute phase solutions, the first one showing the smoothness assumption that Itoh condition holds for the absolute images. This is, in fact, the case in many phase imaging applications, where phase is very often spatially smooth or, at least, piecewise smooth.

It is instructive to note that the Itoh condition can also be understood as a version of the Nyquist sampling theorem. Nyquist's theorem states that a continuous, bandwidth-limited, signal[1] can be completely reconstructed from a sampling made, almost everywhere, at a frequency greater than the double of its higher frequency component w [102]. This means that, the "minimum" sampling must have a frequency higher than $2w$, for which the samples present a phase difference less than π radians, which is exactly the Itoh condition (2.4). Furthermore, as stated in Nyquist's theorem, Itoh condition can be relaxed just to be satisfied *almost everywhere* in the image.

Itoh condition lies at the heart of most phase unwrapping techniques, hence the emphasis we have put on it in this section. In the following one, we will briefly review the main phase unwrapping approaches and representative state-of-the-art algorithms.

2.2 Main Phase Unwrapping Approaches and State-Of-The-Art Algorithms

We have seen that Itoh condition immediately provides a phase unwrapping method, which, as explained in the previous section, employs a path following concept. Nevertheless, it is unrealistic to expect it to be applicable everywhere, as phase images very often exhibit *discontinuities*, *i.e.*, neighbour pixels phase differences larger than π radians, which constitute violations to the Itoh condition. Moreover, noise also introduces phase discontinuities.

In this scenario, the phase unwrapping problem is rather more difficult and a great number of solving techniques (exact or approximate) have been proposed in the literature. In this section, we succinctly overview the main approaches and highlight some of the representative algorithms.

2.2.1 Path Following Methods

Path following methods directly apply the concept, introduced in the Itoh algorithm, of discrete phase integration along a path. Given a starting pixel, for which the absolute

[1] A continuous function whose Fourier transform power spectrum is limited [102].

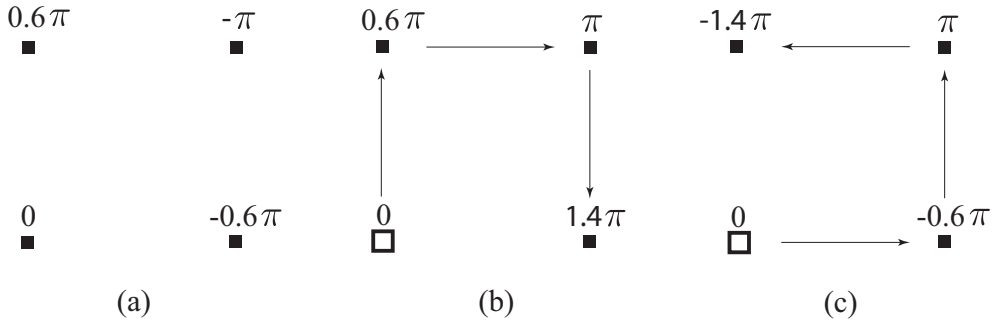

Figure 2.2: (a) Wrapped image. (b) A possible unwrapped solution. (c) Another possible unwrapped solution.

phase is known, Itoh method prescribes on how to compute the absolute phase on any other pixel, without restricting the path linking the two whatsoever. A basic question arises, though, on whether this discrete integration is, in general, path independent. The answer to this question is negative, as is illustrated in Figure 2.2, where a very simple counter-example is given. There, we depict an elementary wrapped image [Figure 2.2 (a)] along with the unwrapped solutions obtained by employing the Itoh condition using two distinct paths linking the start pixel (represented by a hollow square) and the end pixel [Figs. 2.2 (b) and (c) respectively]. In what follows, we call *parallel paths* to any two (or more) paths sharing the same start and end pixels. As can be seen, in this case the integration is path dependent.

Residues

These path dependence phenomena in 2D phase unwrapping were first reported by Ghiglia *et al.* in [48]. There, furthermore, the authors observed that these inconsistencies were restricted to some regions in the phase image.

We note here that path integration dependence among two parallel[2] paths can be tested by reverting the direction of one of them, and then integrating along the resultant closed loop path. Clearly, there is path dependence when that quantity does not evaluate to zero.

Accordingly, to identify in full detail the inconsistencies locations in the image, Ghiglia *et al.* devised the (natural) strategy of path integrating the phase around every elementary 2×2 loop; whenever that sum is not zero, it signals an inconsistency located precisely

[2]By definition, path integration dependence is to be tested between parallel paths.

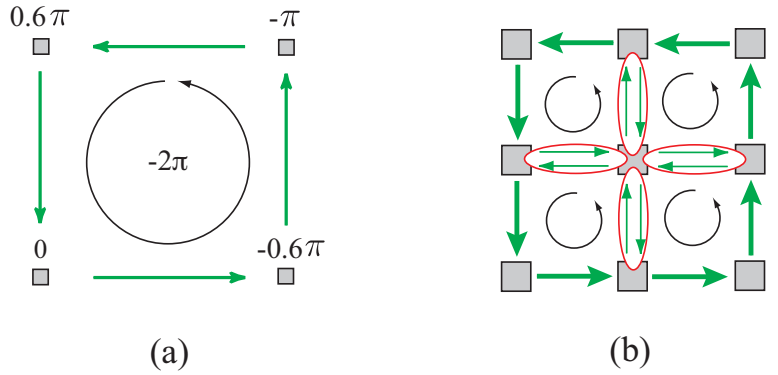

Figure 2.3: (a) An elementary closed loop having a residue. The path integration always sums up to a 2π multiple, and in this case the residue charge is negative. (b) Any closed loop can be given as composition of elementary closed loops. In this sketch each pair of cancelling elementary path components is signalled by a red ellipse. The remaining components constitute the original outer closed path.

on that loop. Later, the term residue[3], instead of inconsistency, was introduced by Goldstein *et al.* in [53], and became the standard term ever since. By convention residues are computed using counter-clockwise closed loops, the absolute value of the sum is always a 2π multiple[4], as illustrated in Figure 2.3 (a), and its signal defines the *residue charge* sometimes also termed *residue polarity*. It should be noted that a 2×2 loop is elementary, in the sense that it is the shortest closed path that we may define and, accordingly, any closed path can be given by a composition of all such elementary loops that it encloses; Figure 2.3 (b) illustrates this issue. Therefore, given two parallel paths and considering again the correspondent closed loop, the sum of the enclosed residues is an effective criterion for inconsistency detection. We must remark at this point that while, as above referred, a residue implies a phase discontinuity existence, the converse implication does not hold. Therefore, additional information is very often, even if implicitly, introduced, as will become apparent in the next sections.

Branch Cuts Algorithms

A strategy to overcome path dependence in path following phase unwrapping methods is to connect opposite charge residues with certain lines with which integration paths are not allowed to have cross-overs. In this way, the net charge of possible residues that may

[3]In a clear resemblance with complex analysis.

[4]It can be easily shown [49, Chap.2].

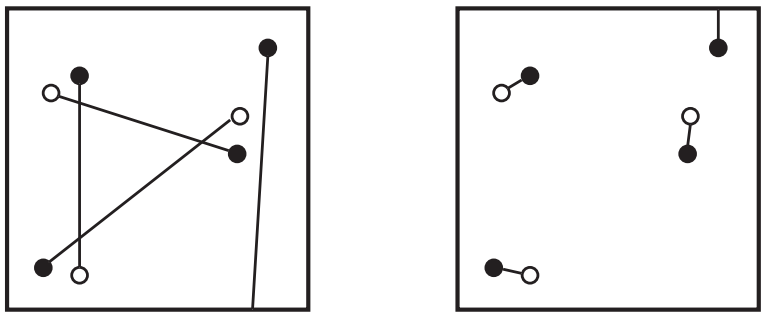

Figure 2.4: Example of residues and respective possible branch cuts configurations (taken from [49]). Positive charged residues are represented by black dots and negative charged ones by white dots. (a) Ill branch cuts configuration. (b) Minimum length branch cuts configuration.

be enclosed on any path, is necessarily zero and, as argued in the previous section, there is no path dependence phenomena (as alluded before, this does not ensure a correct phase unwrapping though). Those lines are the so-called *branch cuts*[5]; other valid branch cuts are those linking a residue to a border of the image (it makes it impossible for any path to encircle the residue). From the many PU algorithms of the branch cuts type published in the literature, we emphasize [53] by Goldstein, Zebker, and Werner, published in 1988, which is one of the earliest to be reported in the 2D phase unwrapping literature.

Choosing the placement for the branch cuts is a critical task, as illustrated in Figure 2.4 taken from [49]. In Figure 2.4 (a), we show a set of opposite charges residues and a certain branch cuts configuration. Clearly, that is an ill choice, as there are large isolated regions which will always remain so[6], and the lengthy branch cuts almost isolate other huge regions as well. The proposed configuration in Figure 2.4(b) is clearly better, suggesting the minimization ot the total branch cuts length as a criterion to the choice of the cuts configuration.

To minimize the total branch cuts length is, by itself, a very difficult problem. That is why Golsdstein's algorithm only solves it approximately. Besides being seminal in the phase unwrapping literature, Goldstein's algorithm is still competitively fast and does not restrict itself to creating dipoles, but also residues clusters[7]. Other branch cuts algorithms

[5]Also termed *residue cuts* by some authors.

[6]As integration paths cannot traverse branch cuts.

[7]More complex structures in which same charge residues are linked together forming charged clusters.

include, *e.g.*, [58], [26].

Quality Guided Algorithms

This class of algorithms employs quality maps to guide the integration paths. By noting that residues tend to be located in low quality regions of the image [49, Chap.4], they use the additional information to avoid residues-originated path dependence without, however, explicitly identifying those residues. In fact, they constitute an attempt to overcome the possible misplacement of branch cuts which, as previously referred, is a difficult problem.

Many of these techniques basically adopt the criterion of letting the quality values to define the order by which phase is unwrapped, giving priority to high quality phase pixels [88], [73].

A further development is the design of algorithms using quality maps to delineate the branch cuts [83], [34], [40]. In doing so, they attempt to employ the additional information contained in the quality maps, as well as retaining the branch cuts guarantee of path integration independence.

When a good quality map is lacking, the performance of the Goldstein's algorithm is found to be superior to the performance of quality guided algorithms [49, Chap. 4].

2.2.2 Minimum Norm Methods

In the previous section, we introduced a seminal phase unwrapping class of methods which rely on path following concepts. Now, we will overview another major approach to phase unwrapping: the minimum norm methods. As will become apparent in what follows, they rely on a completely different concept. While path following methods are local in nature, minimum norm methods adopt a global perspective, addressing the problem via optimization procedures that involve the image as a whole.

The Minimum L^p Norm

Minimum norm methods try to find an absolute phase image solution $\mathbf{\Phi}$[8], for which the L^p norm[9] of the difference between absolute phase's linear differences[10] and wrapped phase's

The opposite charged clusters are then connected by a branch cut to balance charge.

[8]When referring to a whole image, instead of one of its pixels, we will employ boldface types.

[9]This is an analogy with norms defined in L^p spaces, which are measure theory concepts. For further reading see, *e.g.*, [84].

[10]The term *linear difference* is employed here as the difference between neighbour pixels values.

linear differences, horizontal and vertical, is minimized. This kind of methods, thus, look for unwrapped phase images whose local variations match the measured local variations, in a certain sense that is given by the particular L^p norm chosen, as detailed in the next paragraph. So, in fact, they can be considered as surface fitting processes.

More formally, the minimization goal is to yield an unwrapped image solution $\hat{\mathbf{\Phi}}$, and can be expressed by

$$\hat{\mathbf{\Phi}} = \arg\min_{\mathbf{\Phi}} E(\mathbf{\Phi}), \tag{2.10}$$

with $E(\mathbf{\Phi})$ being the above referred L^p norm which is given by

$$E(\mathbf{\Phi}) = \sum_{m=1}^{M}\sum_{n=1}^{N-1}\left|\Delta^h\phi_{m,n} - \Delta^h\psi_{m,n}\right|^p + \sum_{m=1}^{M-1}\sum_{n=1}^{N}|\Delta^v\phi_{m,n} - \Delta^v\psi_{m,n}|^p\,,\ p \geq 0 \tag{2.11}$$

and

$$\Delta^h\phi_{m,n} \equiv \phi_{m,n+1} - \phi_{m,n},\ \ \Delta^v\phi_{m,n} \equiv \phi_{m+1,n} - \phi_{m,n},$$

$$\Delta^h\psi_{m,n} \equiv \mathcal{W}\left(\psi_{m,n+1} - \psi_{m,n}\right),\ \ \Delta^v\psi_{m,n} \equiv \mathcal{W}\left(\psi_{m+1,n} - \psi_{m,n}\right),$$

where $\mathbf{\Phi}$ is a possible unwrapped phase image, $\mathbf{\Psi}$ is the wrapped phase image, M and N denote, respectively, the number of lines and columns in the images, $\Delta^h(\cdot)$ and $\Delta^v(\cdot)$ denote the horizontal and vertical linear differences, respectively, and $\mathcal{W}$ is the wrapper operator introduced in expression (2.2). Let us note here that the presence of the wrapper operator is, again, a way of applying the Itoh condition[11]. Given that by hypothesis $\mathbf{\Phi} = \mathbf{\Psi} + 2\pi\mathbf{k}$, where $\mathbf{k}$ is an integer image, (2.11) turns into

$$E(\mathbf{\Phi}) = \sum_{m=1}^{M}\sum_{n=1}^{N-1}\left|\Delta^h k_{m,n}\right|^p + \sum_{m=1}^{M-1}\sum_{n=1}^{N}|\Delta^v k_{m,n}|^p\,,\ p \geq 0, \tag{2.12}$$

where

$$\Delta^h k_{m,n} \equiv k_{m,n+1} - k_{m,n},\ \ \Delta^v k_{m,n} \equiv k_{m+1,n} - k_{m,n},$$

and where, without loss of generality, we do not care about a 2π factor attached to the integer values. From (2.12) we can see that we are dealing with an optimization problem constrained to the integers.

[11] To illustrate the importance of operator $\mathcal{W}$ in this formula, let us consider two neighbour pixels with phase values $\pi-0.1$ and $\pi+0.1$, respectively. Their correspondent derivative is $\Delta = 0.2$. On the other hand, their wrapped counterparts are $\pi - 0.1$ and $-\pi + 0.1$ respectively, and accordingly, their correspondent derivative is $\Delta = -2\pi + 0.2$. Obviously, it is desirable to fit the derivative of the unwrapped solution to the true $\Delta = 0.2$ and not to $\Delta = -2\pi + 0.2$. It is, therefore, convenient to apply the wrapper operator to annihilate the erroneous introduced 2π ambiguity in the latter derivative value.

Furthermore, when a quality map $\boldsymbol{Q}$ is available, it is possible to derive horizontal and vertical quality measures [41] $\boldsymbol{Q}^h$ and $\boldsymbol{Q}^v$, respectively, and it can be defined a weighted L^p norm analogous to (2.11):

$$E(\boldsymbol{\Phi}) = \sum_{m=1}^{M}\sum_{n=1}^{N-1} q^h_{m,n}\left|\Delta^h\phi_{m,n} - \Delta^h\psi_{m,n}\right|^p + \sum_{m=1}^{M-1}\sum_{n=1}^{N} q^v_{m,n}\left|\Delta^v\phi_{m,n} - \Delta^v\psi_{m,n}\right|^p,\ p \geq 0. \tag{2.13}$$

Namely, in regions where it is known to exist absolute phase discontinuities, or noise corruption, we can set $q_{m,n}$ to low or zero values and, so, reduce the poor quality phase's influence on the unwrapped solution [49, Chap. 4].

Expressions (2.10), (2.11), and (2.13) clearly highlight the global character of these techniques, in the sense that all the observed phases are used to compute a solution. Distinct exponent p values in L^p norms yield distinct properties in the unwrapping performance; usually only $p \leq 2$ values are employed and namely $p = 0, 1, 2$ are the most representative. We will next quickly refer to some of the correspondent algorithms for these p values.

L^2 Norm Algorithms

With $p = 2$ we have a least squares problem. We remark here that the minimization of an L^p norm, as defined above, even just for $p = 2$ is a discrete minimization problem which is very demanding from the computational point of view [49, Chap. 5]. As such, the great majority of the existing algorithms are approximate ones. In addition, a drawback of the L^2 norm based criterion is that it tends to smooth discontinuities, unless they are provided as binary weights.

Fried and Hudgin were the first to propose least squares type phase unwrapping approximate algorithms [42], [57]. Since then, many algorithms have been published, from which we highlight (due to popularity) those approximating the least squares solution by relaxing the discrete domain $\mathbb{Z}^{MN}$ to $\mathbb{R}^{MN}$. In doing so, they intend to overcome the complexity introduced by the discrete nature of the problem. It can be shown that in the continuous domain, the problem is equivalent to solving a Poisson partial differential equation [49, Chap. 5]. This has been solved by applying techniques using fast Fourier or cosine transforms, and then coming back to discrete domain [50]. An exact solution to least squares is developed as a step of the $\mathbb{Z}\pi M$ algorithm in [36], using network programming techniques.

L^1 Norm Algorithms

L^1 norm performs better than L^2 norm in what discontinuity preservability is concerned [68], [77]. Such a criterion has been solved exactly by Flynn [41] and Costantini [24], using network programming concepts. We here highlight with a little more detail Flynn's algorithm, as it is somehow closer to our own approach.

Flynn's Minimum Discontinuity Algorithm

As presented previously, phase unwrapping is an inverse problem with relation to the wrapping process, which in turn, by definition, creates discontinuities in the wrapped image. Given that the discontinuities in the unwrapped image should be limited to noisy areas and to the true absolute image discontinuities, which often can be identified in quality maps, Flynn's algorithm [41] fundamental idea consists in choosing between the possible unwrapped images, the one which minimizes discontinuities. Basically, this algorithm operates by applying iteratively an elementary procedure of partitioning the image in two connected regions and, then, adding a 2π phase to one of them, such that the weighted sum of discontinuities decreases.

Introducing, succinctly, the notation used by Flynn in [41], let us define, respectively, the vertical and horizontal jump counts by:

$$v_{m,n} = \left\lfloor \frac{\phi_{m,n} - \phi_{m-1,n} + \pi}{2\pi} \right\rfloor, \tag{2.14}$$

$$z_{m,n} = \left\lfloor \frac{\phi_{m,n} - \phi_{m,n-1} + \pi}{2\pi} \right\rfloor, \tag{2.15}$$

where (m, n) represents the usual pixel indexing, and $\lfloor x \rfloor$ is the largest integer less or equal than x. A jump count is, then, the multiple of 2π that is required to annihilate a discontinuity (we recall that a discontinuity exists when two neighbouring pixels phase difference is greater than π). The goal of Flynn's algorithm is, thus, to minimize the L^1 norm of the (weighted) jump counts (2.16)

$$E = \sum w^v_{m,n} \left| v_{m,n} \right| + w^z_{m,n} \left| z_{m,n} \right|, \tag{2.16}$$

where $w^v_{m,n}$ and $w^z_{m,n}$ denote vertical and horizontal weights, respectively, which are derived from quality maps. It should be noted that the minimization procedure is guaranteed to reach the global minimum [41].

2.2.3 Low p Valued L^p Norm Algorithms

With $0 \leq p < 1$ the discontinuity preserving ability of the minimum L^p norm algorithms is further increased at stake, however, of highly complex algorithms [21]. In particular, the L^0 norm is generally accepted as the most desirable in practice. The minimization of the $L^p, 0 \leq p < 1$, norm is, however, an NP-hard problem [44], [21], for which approximate algorithms have been proposed in [49, Chap. 5] and [22]. An interpretation for the benefits of the L^0 norm (and, for that matter, the L^p norm with $0 \leq p < 1$) is the sparsity of the solution which, for L^p norms, is highest for $p = 0$. It is accepted (in the phase unwrapping community) that those sparse solutions, which tend to concentrate the discontinuities in a few locations, give the best approximation to ground truth under the minimum L^p norm rationale.

2.2.4 Bayesian and Parametric Methods

The Bayesian approach relies on a data-observation mechanism model, as well as a prior knowledge of the phase to be modelled. This is a probabilistic approach to phase unwrapping, where data-observation mechanism is modelled by a conditional probability density function $P(\mathbf{\Psi}|\mathbf{\Phi})$, and the *a priori* knowledge by the so-called prior probability density function $P(\mathbf{\Phi})$. Here $\mathbf{\Phi}$ is the unwrapped image and $\mathbf{\Psi}$ the wrapped image. Using the Bayes' theorem

$$P(\mathbf{\Phi}|\mathbf{\Psi}) = \frac{P(\mathbf{\Psi}|\mathbf{\Phi})P(\mathbf{\Phi})}{P(\mathbf{\Psi})}, \tag{2.17}$$

we can get the *a posteriori* probability density function and, from there, to infer the unwrapped image $\mathbf{\Phi}$.

For instance in [70], a non-linear optimal filtering is applied, while in [37] an InSAR observation model is considered, taking into account not only the image phase, but also the *backscattering coefficient* and *correlation factor* images, which are jointly recovered from InSAR image pairs. Work [32] proposes a fractal based prior.

Finally, parametric algorithms constrain the unwrapped phase to a parametric surface. Low order polynomial surfaces are used in [43]. Very often in real applications just one polynomial is not enough to describe accurately the complete surface. In such cases the image is partitioned and different parametric models are applied to each partition [43].

Chapter 3

Phase Unwrapping: Convex Scenario

3.1 Bayesian Model

The observation model relating the noisy wrapped phase with the true phase depends on the system under consideration (see, *e.g.*, [49, 36, 64] for an account of observation models in different coherent imaging systems). The essential of most of these observation mechanisms is, however, captured by the relation

$$\begin{aligned} z &= Ae^{j\phi} + n, \quad A > 0, \\ &= |z|e^{j(\phi+\phi_n)}, \end{aligned} \tag{3.1}$$

where ϕ is the true phase value (the so-called absolute phase value), $n = n_I + jn_Q$ is a complex-valued zero-mean circular white additive noise with variance σ^2 (*i.e.*, n_I and n_Q are zero-mean independent Gaussian random variables with variance $\sigma^2/2$), ϕ_n is the phase of noise n, A is an amplitude, and z is a random variable from which, by using the wrapper operator, we get the observed wrapped (and noisy) phase. The wrapper operator was defined through expressions (2.1) and (2.2). A more compact and possibly more familiar definition is given by

$$\psi = \text{angle}(z) = \mathcal{W}(\phi + \phi_n), \quad \psi \in [-\pi, \pi). \tag{3.2}$$

We recall that the operator $\mathcal{W}$ maps the phase $\phi + \phi_n$ into the principal phase interval $[-\pi, \pi)$: our *goal* is to infer the absolute phase ϕ from the wrapped and noisy observed phase ψ.

Let $\mathcal{G} = (\mathcal{V}, \mathcal{E})$ be a directed graph associated to a first order Markov random field (MRF), where the set of nodes $\mathcal{V}$ represents the set of image pixels and the set of directed edges $\mathcal{E}$ represents the set of links between pairs of neighboring pixels. In this work, we consider only first-order MRFs and, therefore, the edges in $\mathcal{E}$ link horizontal and vertical immediate neighbors. Nevertheless, all the concepts and results next presented are valid for any set of pairwise interactions. We will make inference in these random fields.

We follow the Bayesian framework, accordingly, we need to build the posterior density function $p(\boldsymbol{\phi}|\boldsymbol{Z})$ of the phase image $\boldsymbol{\phi} \in \mathbb{R}^{|\mathcal{V}|}$, given the observed complex image $\boldsymbol{Z} \in \mathbb{C}^{|\mathcal{V}|}$ ($\mathbb{C}$ denotes the complex field). Invoking the Bayes' law we have $p(\boldsymbol{\phi}|\boldsymbol{Z}) \propto p(\boldsymbol{Z}|\boldsymbol{\phi})p(\boldsymbol{\phi})$, where $p(\boldsymbol{Z}|\boldsymbol{\phi})$ is the likelihood function measuring the data fit, and $p(\boldsymbol{\phi})$ is the prior density encoding *a priori* knowledge about the absolute phase image $\boldsymbol{\phi}$.

Let us assume conditional independence in the observation mechanism, *i.e.*, $p(\boldsymbol{Z}|\boldsymbol{\phi}) = \prod_{i\in\mathcal{V}} p(z_i|\phi_i)$. This is a standard assumption that is true as long as the resolution volumes that contribute to distinct pixels are disjoint, which is a valid approximation for most imaging systems [23]. Furthermore, let us explicit the knowledge that the prior of an MRF is Gibbsian, *i.e.*, $p(\boldsymbol{\phi}) \propto \exp\{-\mu V(\boldsymbol{\phi})\}$ [45, 5], where $V(\boldsymbol{\phi}) = \sum_{\{i,j\}} V_{i,j}(\phi_i, \phi_j)$, μ is often termed the regularization parameter, $V_{i,j}(\cdot)$ (a real valued function) is the so-called *clique potential* associated with edge $\{i, j\}$, and where we consider $V_{i,j}(\phi_i, \phi_j) \equiv V_{i,j}(\phi_i - \phi_j)$. The usual assumption that, in an MRF, the random variables at neighboring sites have similar realizations, *i.e.*, that neighboring pixels have similar values, is modeled by such set of potentials, which penalize the difference between those values. It is in view of this penalization that we define $V_{i,j}(\phi_i, \phi_j) \equiv V_{i,j}(\phi_i - \phi_j)$. Generally, greater differences between phase values get more penalized, nevertheless, the specific dependence is, obviously, determined by the particular chosen $V_{i,j}$.

Under the Bayesian framework and an MRF prior it is usual to adopt the *maximum a posteriori* (MAP) criterion to estimate the unknown, which in our case is $\boldsymbol{\phi}$. The MAP estimate seeks the mode of the posterior distribution: $\hat{\boldsymbol{\phi}} = \arg\max_{\boldsymbol{\phi}} p(\boldsymbol{\phi}|\boldsymbol{Z})$. Although MAP is not the only criterion available, it has been widely used in reconstruction problems (such as ours) for which it very often seems well suited [45, 72].

MAP estimation

In these circumstances, computing the MAP estimate is equivalent to minimize the negative logarithm of the posterior density, *i.e.*, the *energy*, $E : \mathbb{R}^{|\mathcal{V}|} \to \mathbb{R} \cup \{+\infty\}$ given

by

$$E(\boldsymbol{\phi}) \equiv \underbrace{\sum_{i\in\mathcal{V}} D_i(\phi_i)}_{\text{Data fidelity term}} + \mu \underbrace{\sum_{\{i,j\}\in\mathcal{E}} V_{i,j}\,(\phi_i - \phi_j)}_{\text{Prior term}}, \tag{3.3}$$

where $D_i(\phi_i) \equiv -\log p(z_i|\phi_i)$.

Given the observation mechanism introduced in (3.2), we have (see, *e.g.*, [36])

$$p(z_i|\phi_i) = \frac{1}{\pi\sigma^2} e^{\frac{-|z_i - Ae^{j\phi_i}|^2}{\sigma^2}},$$

and, thus, by dropping some irrelevant constants we get

$$D_i(\phi_i) = -\lambda_i \cos(\phi_i - \psi_i), \quad \text{for } \; i \in \mathcal{V},$$

with $\lambda_i \equiv 2A|z_i|/(\sigma^2)$ and $\psi_i \equiv \text{angle}(z_i)$; *i.e.*, the loglikelihood function is proportional to a shifted cosine of $\boldsymbol{\phi}$. The MAP absolute phase estimate is then obtained by minimizing the negative of the logposterior function given by

$$E(\boldsymbol{\phi}) \equiv \underbrace{\sum_{i\in\mathcal{V}} -\lambda_i \cos(\phi_i - \psi_i)}_{\text{Data fidelity term}} + \mu \underbrace{\sum_{\{i,j\}\in\mathcal{E}} V_{i,j}\,(\phi_i - \phi_j)}_{\text{Prior term}}. \tag{3.4}$$

Notice that μ, the regularization parameter, sets the relative weight between the data fidelity term and the prior term.

We emphasize that the MAP estimation gives place to minimizing the logposterior (3.4). For a given image phase $\boldsymbol{\phi}$ candidate to a MAP solution, this function comprises a data fidelity term, which measures the misfit between the observed data and $\boldsymbol{\phi}$, and a prior term, which measures the lack of plausibility of $\boldsymbol{\phi}$, induced by the potentials $V_{i,j}(\cdot)$; roughly, enforcing smooth surfaces implies convex potentials, whereas enforcing piecewise-smoothness, and thus preserving surface's discontinuities, implies non-convex potentials.

Assume that the noise approaches zero. Then, $\lambda_i \equiv 2A|z_i|/(\sigma^2) \to +\infty$ and any MAP solution satisfies $\cos(\phi_i - \psi_i) = 1$ implying the constraints

$$\phi_i = \psi_i + 2\pi k_i, \quad \text{for } i \in \mathcal{V} \quad \text{and} \quad k_i \in \mathbb{Z}. \tag{3.5}$$

Therefore, computing the MAP solution reduces to minimizing the prior term in (3.4) under the constraints (3.5). This is the strict phase unwrapping problem, which is an integer optimization problem well known to be a difficult task to perform [20]. The phase unwrapping is even more tricky because, usually, the phase images have a large $|\mathcal{V}|$ (*e.g.*, 10^6 variables for a 1000 by 1000 image) and are noisy.

3.2 Problem Formulation

As we have seen in the previous section, the MAP estimation of the absolute phase ϕ in a noiseless scenario reduces to minimize (3.4) under constraints (3.5), *i.e.*, to minimize

$$E(\mathbf{k}|\boldsymbol{\psi}) \equiv \sum_{\{i,j\}\in\mathcal{E}} V_{ij}\left(\Delta\phi_{ij}\right), \tag{3.6}$$

where $\mathbf{k} \equiv \{k_i : i \in \mathcal{V}\}$ is an image with integer values which count 2π multiples, the so-called *wrap-count image*, $\boldsymbol{\psi} \equiv \{\psi_i : i \in \mathcal{V}\}$ is the observed wrapped phase image, $V_{ij}(\cdot)$ is the clique potential, a real valued function, and $\Delta\phi_{ij}$ denotes the difference between neighboring pixels phase given by

$$\Delta\phi_{ij} \equiv \left[2\pi(k_i - k_j) - \Delta\psi_{ij}\right],\ k \in \mathbb{Z} \tag{3.7}$$

$$\Delta\psi_{ij} \equiv \psi_i - \psi_j. \tag{3.8}$$

We can encode the *a priori* availability of knowledge about the location of phase discontinuities, by introducing variables d_{ij} that signal their existence. So, $d_{ij} \in \{0, 1\}$, with $d_{ij} = 0$ meaning that we know that there is a discontinuity between neighboring pixels i and j, and $d_{ij} = 1$ meaning that we do not have such information. The MAP estimation consists then of minimizing (3.9)

$$E(\mathbf{k}|\boldsymbol{\psi}) \equiv \sum_{\{i,j\}\in\mathcal{E}} V_{ij}\left(\Delta\phi_{ij}\right) d_{ij}, \tag{3.9}$$

which is identical to (3.6) except for the terms d_{ij} which we have just introduced, and for which, by default, we have $d_{ij} = 1$.

Our goal is to find the integer image $\mathbf{k}$ that minimizes energy (3.9), $\mathbf{k}$ being such that $\boldsymbol{\phi} = 2\pi\mathbf{k} + \boldsymbol{\psi}$, where $\boldsymbol{\phi}$ is the estimated unwrapped phase image, and $\boldsymbol{\psi}$ is the observed wrapped image.

As will be seen in the next section, this energy minimization approach yields the classical minimum L^p norm formulation, or a more general one, depending on the chosen potential V. We should stress that the variables d_{ij}, conveying discontinuity information, are introduced when available. In the jargon of PU these images are the quality maps. These, can also be used as continuous variables in $[0, 1]$, expressing prior knowledge on phase variability. Quality maps can be derived, for example, from correlation maps in InSAR, or from phase derivative variance in a more general setting [49, Chap. 3].

In the next sections, we present in detail the proposed approach. We show that for convex potentials V, the minimization of $E(\mathbf{k}|\boldsymbol{\psi})$ can be achieved through a sequence of binary optimizations; each binary problem is mapped onto a certain graph and a binary minimization obtained by computing a max-flow/min-cut on it. Finally, we address a set of potentials tailored to phase unwrapping.

3.3 Equivalence Between Local and Global Minimization

Assuming a convex potential V, the following theorem assures that if the minimum of $E(\mathbf{k}|\boldsymbol{\psi})$ is not yet reached, then, there exists a binary image $\boldsymbol{\delta} \in \{0,1\}^{|\mathcal{V}|} \equiv \mathcal{B}$ (*i.e.*, the elements of $\boldsymbol{\delta}$ are 0 or 1) such that $E(\mathbf{k}+\boldsymbol{\delta}|\boldsymbol{\psi}) < E(\mathbf{k}|\boldsymbol{\psi})$. Therefore, if a given image $\mathbf{k}$ is locally optimal with respect to the neighborhood $\mathcal{N}_1(\mathbf{k}) \equiv \{\mathbf{k}+\boldsymbol{\delta} : \boldsymbol{\delta} \in \mathcal{B}\}$, *i.e.*, if $E(\mathbf{k}'|\boldsymbol{\psi}) \geq E(\mathbf{k}|\boldsymbol{\psi})$ for all $\mathbf{k}' \in \mathcal{N}_1(\mathbf{k})$, then $\mathbf{k}$ it is also globally optimal.

Theorem 1 *Let* $\mathbf{k}_1$ *and* $\mathbf{k}_2$ *be two wrap-count images such that*

$$E(\mathbf{k_2}|\boldsymbol{\psi}) < E(\mathbf{k_1}|\boldsymbol{\psi}). \tag{3.10}$$

Then, if V *is convex, there exists a binary image* $\boldsymbol{\delta} \in \mathcal{B}$ *such that*

$$E(\mathbf{k_1}+\boldsymbol{\delta}|\boldsymbol{\psi}) < E(\mathbf{k}_1|\boldsymbol{\psi}). \tag{3.11}$$

Proof: See the Appendix.

3.4 Convergence Analysis

In accordance with Theorem 1, we can iteratively compute $\mathbf{k}^{t+1} = \mathbf{k}^t + \boldsymbol{\delta}$, where $\boldsymbol{\delta} \in \mathcal{B}$ is such that it minimizes $E(\mathbf{k}^t+\boldsymbol{\delta}|\boldsymbol{\psi})$, until the minimum energy is reached. There is of course the pertinent question of whether the algorithm stops[1] and, if it does, in how many iterations. Regarding the second issue, assuming that $\boldsymbol{k}^0 = \mathbf{0}$, the next lemma, which is inspired in the Proposition 3.7 of [27], leads to the conclusion that after t iterations the algorithm minimizes $E(\cdot|\boldsymbol{\psi})$ in $\mathcal{D}_t \equiv \{\mathbf{k}' : 0 \leq k'_i \leq t\}$.

[1] *To stop* is a necessary condition for a set of instructions to be considered an algorithm, in many of the definitions of the concept.

Lemma 1 *Let* $\mathbf{k}^t$ *and* $\mathbf{k}^{t+1}$ *be globally optimal minimizers of* $E(\cdot|\boldsymbol{\psi})$ *on* $\mathcal{D}_t$ *and* $\mathcal{D}_{t+1}$*, respectively. Then*

$$\mathbf{k}^{t+1} - \mathbf{k}^t \in \mathcal{B}.$$

Therefore, $\mathbf{k}^{t+1}$ *can be found by minimizing* $E(\mathbf{k}^t + \boldsymbol{\delta}|\boldsymbol{\psi})$ *with respect to* $\boldsymbol{\delta} \in \mathcal{B}$*.*

Proof: See the Appendix.

Assume that the range of E spans over K wrap-counts. Then its global minimizer is in the set $\mathcal{D}_K$, and therefore Lemma 1 assures that the iterative scheme

$$\begin{aligned} &do \\ &\qquad \mathbf{k}^{t+1} = \mathbf{k}^t + \ \arg\min_{\boldsymbol{\delta}\in\mathcal{B}} E(\mathbf{k}^t + \boldsymbol{\delta}|\boldsymbol{\psi}) \\ &while \quad E(\mathbf{k}^{t+1}|\boldsymbol{\psi}) < E(\mathbf{k}|\boldsymbol{\psi}), \end{aligned}$$

starting with $\boldsymbol{k}^0 = \mathbf{0}$, finds this minimizer in at most K iterations. Its complexity is therefore KT, where T is the complexity of a binary optimization. Regarding the first issue, of whether the algorithm stops, we note that if the energy minimum exists, then it is evident that between $\boldsymbol{k}^0 = \mathbf{0}$ (or any other starting $\boldsymbol{k}^0$) and a minimizer, the number of *configurations* is finite; by *configuration* we mean the set of images having the same difference image (a difference image is one whose entries are given by $\Delta k = k_i - k_j$; we stress that the considered energy depends only on configurations). This implies that the algorithm stops. We note that for the minimum to exist it is enough to consider that the clique potential is coercive, which we consider hereinafter.

3.5 Mapping Binary Optimizations onto Graph Cuts

Let $k_i^{t+1} = k_i^t + \delta_i$ be the wrap-count at time $t+1$ and pixel i. Introducing k_i^{t+1} into (3.7) we obtain

$$\Delta\phi_{ij} = \left[2\pi(k_i^{t+1} - k_j^{t+1}) - \Delta\psi_{ij}\right]. \tag{3.12}$$

After some simple manipulation, we get

$$\Delta\phi_{ij} = \left[2\pi(\delta_i - \delta_j) + a_{ij}\right], \tag{3.13}$$

where

$$a_{ij} \equiv 2\pi(k_i^t - k_j^t) - \Delta\psi_{ij}. \tag{3.14}$$

Now, introducing (3.13) into (3.9), we can rewrite energy $E(\mathbf{k}^t + \boldsymbol{\delta}|\boldsymbol{\psi})$ as a function of the binary variables $\delta_i \in \{0, 1\}$, *i.e.*,

$$E(\mathbf{k}^t + \boldsymbol{\delta}|\boldsymbol{\psi}) = \sum_{\{i,j\}\in\mathcal{E}} \underbrace{V\left[2\pi(\delta_i - \delta_j) + a_{ij}\right] d_{ij}}_{E^{ij}(\delta_i,\delta_j)}. \tag{3.15}$$

We now map the minimization of (3.15) with respect to $\boldsymbol{\delta}$ onto a graph mincut problem. In the last decade a considerable amount of research effort has been devoted to energy minimization by graph cuts methods (among the main contributions we highlight [67], [99], [20], [38], [103], [60]). Namely, the mapping of a pairwise-interaction first order MRF minimization problem into a sequence of binary minimizations, computed by graph cuts techniques, has been addressed in [99] and [20]. Nevertheless, those two works provide approximate solutions only.

Work in [67] gives necessary and sufficient conditions for a binary function with pairwise interactions to be representable on a graph; furthermore, the graph structures therein proposed are simpler and, accordingly, we adopt the method proposed therein. A special reference to [60] should be made: it introduces an exact energy minimization for convex potentials also by using graph cuts. However, in practice, for most problems involving many variables, as is the case with images, the graph there employed can be huge, which imposes heavy computational and storage demands.

Following then [67], we exploit a one-to-one map existing between energy (3.15), as a function of $\boldsymbol{\delta}$, and cuts on $\mathcal{G}$. We further detail that the graph has non negative weights and has two special vertices besides the vertices contained in $\mathcal{V}$, namely the source s and the sink t. An $s-t$ cut $C = \{S, T\}$ is a partition of vertices $\mathcal{V}$ into two disjoint sets S and T, such that $s \in S$ and $t \in T$. The number of vertices is $2 + |\mathcal{V}|$ (two terminals, the source and the sink, plus the number of pixels). The cost of the $s-t$ cut is the sum of costs of all edges that link S to T. Using the notation above introduced, we have

$$\begin{aligned} E^{ij}(0,0) &= V\left(a_{ij}\right) d_{ij}, \\ E^{ij}(1,1) &= V\left(a_{ij}\right) d_{ij}, \\ E^{ij}(0,1) &= V\left(-2\pi + a_{ij}\right) d_{ij}, \\ E^{ij}(1,0) &= V\left(2\pi + a_{ij}\right) d_{ij}. \end{aligned} \tag{3.16}$$

According to [67] we define the class $\mathcal{F}^2$ to be the family of functions that can be written as a sum of functions of up to two binary variables at a time. Clearly energy $E(\mathbf{k}^t + \boldsymbol{\delta}|\boldsymbol{\psi})$

belongs to $\mathcal{F}^2$. Roughly speaking[2], a function of $\mathcal{F}^2$ is *graph representable*, *i.e.*, there exists a one-to-one relation between $\boldsymbol{\delta} \in \{0,1\}^{|\mathcal{V}|}$ [*i.e.*, points in the domain of $E(\mathbf{k}^t + \boldsymbol{\delta}|\boldsymbol{\psi})$] and $s-t$ cuts on that graph, *if and only if* holds

$$E^{ij}(0,0) + E^{ij}(1,1) \leq E^{ij}(0,1) + E^{ij}(1,0). \tag{3.17}$$

For a proof see [67]. In terms of E^{ij} [see expression (3.16)] equation (3.17) can be stated as $[V(-2\pi + a) + V(2\pi + a)]\, d_{ij} \geq 2V(a)d_{ij}$, which is verified due to convexity of V. So, our binary function is graph-representable.

The structure of the graph is as follows: first build vertices and edges corresponding to each pair of neighbouring pixels, and then join these graphs together based on the additivity theorem also given in [67].

So, for each energy term E^{ij} [see expression (3.15)], we construct an "elementary" graph with four vertices s, t, v, and v', where s and t represent the source and the sink, respectively, common to all terms, and v, v', represent the two pixels involved [v being the left (up) pixel and v' the right (down) pixel]. Following very closely [67], we define a directed edge $\{v, v'\}$ with the weight $E(0,1) + E(1,0) - E(0,0) - E(1,1)$. Moreover, if $E(1,0) - E(0,0) > 0$, we define an edge $\{s, v\}$ with the weight $E(1,0) - E(0,0)$ or, otherwise, we define an edge $\{v, t\}$ with the weight $E(0,0) - E(1,0)$. In a similar way for vertex v', if $E(1,1) - E(1,0) > 0$, we define an edge $\{s, v'\}$ with weight $E(1,1) - E(1,0) > 0$ or, otherwise, we define an edge $\{v', t\}$ with the weight $E(1,0) - E(1,1)$. Figure 3.1 (a) shows an example where $E(1,0) - E(0,0) > 0$ and $E(1,0) - E(1,1) > 0$. Figure 3.1 (b) illustrates the complete graph obtained at the end.

We may rewrite each term of energy (3.15) to clarify the mapping between its (binary) minimization and a graph cut. By recalling that $E = \sum_{\{i,j\} \in \mathcal{E}} E^{ij}(x_i, x_j)$, where $x_i, x_j \in \{0,1\}$, and by defining $\bar{x}_i = 1 - x_i$, it is straightforward to verify that the following identity (3.18) holds:

$$E^{ij}(x_i, x_j) = E^{ij}(0,0)\bar{x}_i\bar{x}_j + E^{ij}(1,0)x_i\bar{x}_j + E^{ij}(0,1)\bar{x}_i x_j + E^{ij}(1,1)x_i x_j, \tag{3.18}$$

which in turn we can rearrange into

$$E^{ij}(x_i, x_j) = c + \alpha^i x_i + \alpha^j x_j + \beta^{ij}(x_i - x_j)x_i, \tag{3.19}$$

[2] As defined in [67], a function E of n binary variables is called *graph-representable* if there exists a graph $\mathcal{G} = (\mathcal{V}, \mathcal{E})$ with terminals s and t and a subset of vertices $\mathcal{V}_0 = \{v_1, \ldots, v_n\} \subset \mathcal{V} - \{s, t\}$ such that, for any $\{\delta_1, \ldots, \delta_n\}$, the value of the energy $E(\delta_1, \ldots, \delta_n)$ is equal to a constant plus the cost of the minimum s-t-cut among all cuts $C = \{S, T\}$ in which $v_i \in S$, if $\delta_i = 0$, and $v_i \in T$, if $\delta_i = 1$ $(1 \leq i \leq n)$.

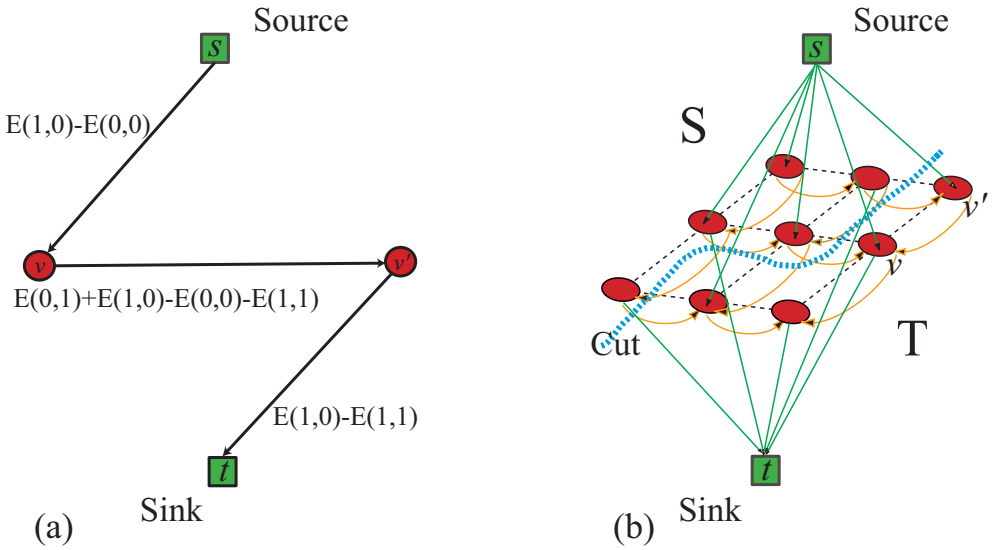

Figure 3.1: (a) Elementary graph for a single energy term, where s and t represent source and sink, respectively, and v and v' represent the two pixels involved in the energy term. In this case $E(1,0) - E(0,0) > 0$ and $E(1,0) - E(1,1) > 0$. (b) The graph obtained at the end results from adding elementary graphs.

by noting that ${x_i}^2 = x_i$, and where $\beta^{ij} = E^{ij}(1,0) + E^{ij}(0,1) - E^{ij}(0,0) - E^{ij}(1,1)$, and c, α^i, and α^j are appropriate coefficients. As already mentioned, this (any) binary energy is graph representable, *i.e.*, can be minimized by computing the min $s-t$ cut of a certain graph, if and *only* if $\beta^{i,j} \geq 0$ [67]. Figure 3.2 clarifies now the aforementioned map between an energy term and an elementary graph $s-t$ cut. One can easily verify that, indeed, the energy values are given by appropriate $s-t$ cuts. We should make two remarks: at the top right quarter of the figure ($\alpha^i < 0$) the value of the cut is equal to the unary term plus a constant. This constant allows us to consider positive weights for the edges of the graph and, obviously, does not change the optimization problem. A second remark concerns the two bottom schemes [configurations $(x_i = 0, x_j = 1)$ and $(x_i = 1, x_j = 0)$, respectively]. In the left scheme the link goes from T to S and, accordingly, it represents a cut whose value is zero (there is no flow from T to S). In the right scheme the link goes from S to T and, accordingly, it represents a cut whose value is β^{ij}. We finally note that the already referred additivity theorem [67] allows to merge all the elementary graphs, corresponding to the E^{ij} terms, and to obtain the energy minimum by computing the min $s-t$ cut of the obtained graph.

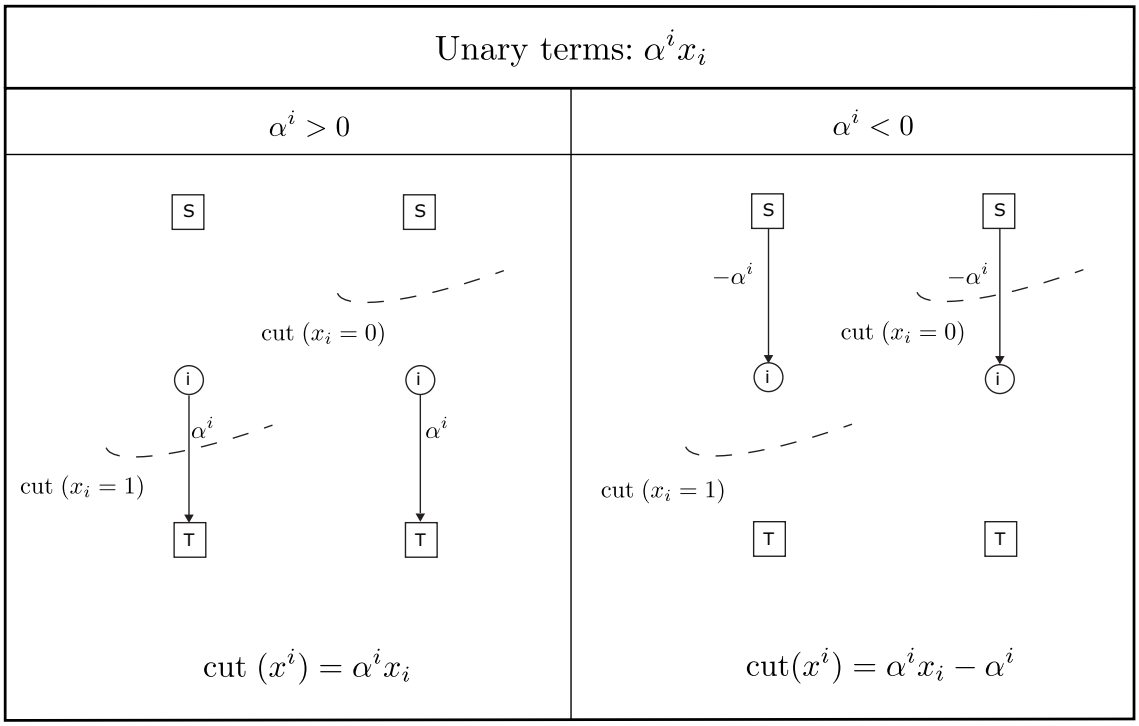

(a)

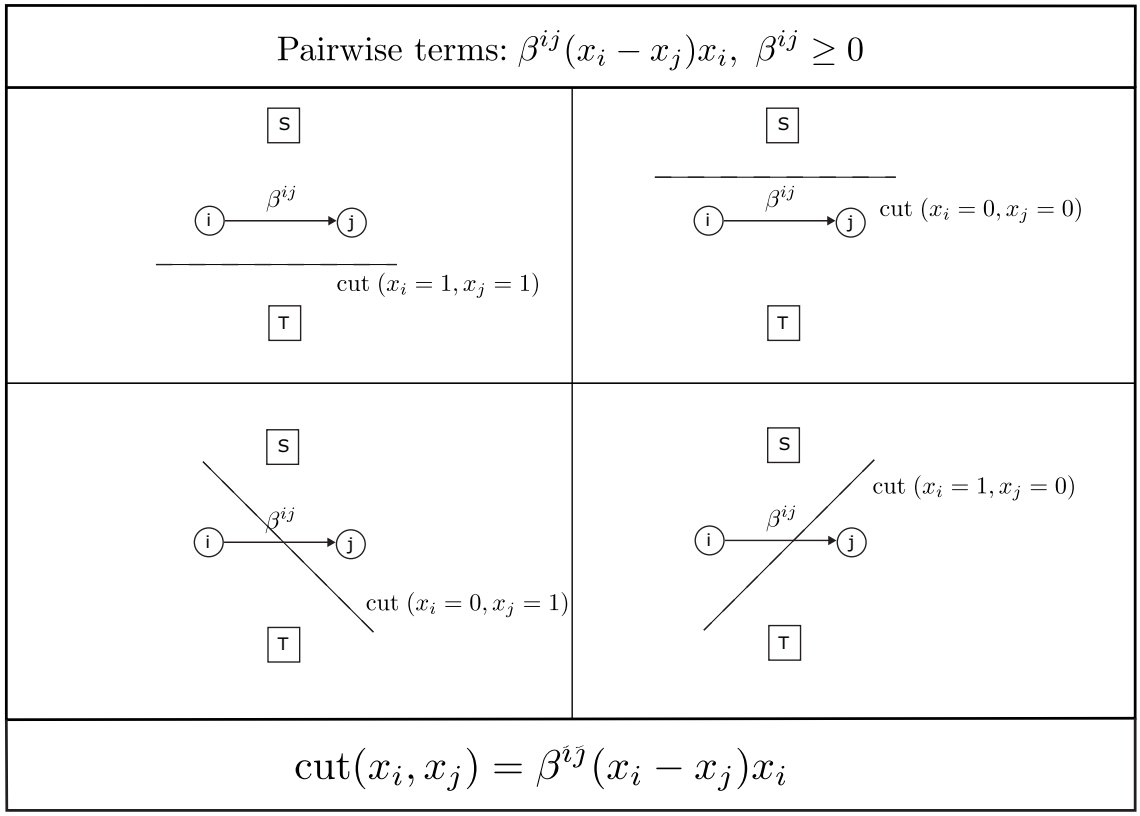

(b)

Figure 3.2: Map between energy (3.19) and a graph cut. (a) Energy's unary terms. (b) Energy's pairwise terms.

3.6 Energy Minimization Algorithm

Algorithm 1 PUMA: Graph cuts based phase unwrapping algorithm.

Initialization: $\mathbf{k} \equiv \mathbf{k}' \equiv \mathbf{0}$, possible_improvement $\equiv 1$

while possible-improvement **do**
  Compute $E(0,0), E(1,1), E(0,1)$, and $E(1,0)$ {for every horizontal and vertical pixel pair}.
  Construct elementary graphs and merge them to obtain the main graph.
  Compute the max-flow/min-cut (S,T) {S- source set; T-sink set}.
  for all pixel i **do**
    if pixel $i \in S$ **then**
      $\boldsymbol{k'}_i = \boldsymbol{k}_i + 1$
    else
      $\boldsymbol{k'}_i = \boldsymbol{k}_i$ {remains unchanged}
    end if
  end for
  if $E(\mathbf{k}'|\boldsymbol{\psi}) < E(\mathbf{k}|\boldsymbol{\psi})$ **then**
    $\mathbf{k} = \mathbf{k}'$
  else
    possible-improvement = 0
  end if
end while

Algorithm 1 shows the pseudo-code for the Phase Unwrapping MAx-flow (PUMA) algorithm. It solves a sequence of binary optimizations until no energy decreasing is possible.

Concerning computational complexity, PUMA takes $N_{bopt} \times N_{mf}$ flops (measured in number of floating point operations), where N_{bopt} and N_{mf} stand for number of binary optimizations and number of flops per max-flow computation, respectively. In Section 3.4 we have proved that the algorithm stops in K iterations, where K is the range of E in wrap-counts. Therefore, $N_{bopt} = K$. Concerning N_{mf}, in the experimental results presented in this work we have used the augmenting path type max-flow/min-cut algorithm proposed in [18]. The worst case complexity for augmenting path algorithms is $O(n^2 m)$ [4], where n and m are the number of vertices and edges, respectively. However, in a huge array

of experiments conducted in [18], authors systematically found out a complexity that is inferior to that of the push-relabel algorithm [52], with the queue based selection rule, which is $O(n^2\sqrt{m})$. Thus, we herein take this bound.

Given that in our graphs $m \simeq 3n$ and N_{bopt} does not depend on n, the worst case complexity of the PUMA algorithm is bounded above by $O(n^{2.5})$. In section 3.8, we run a set of experiments where the worst case complexity is roughly $O(n)$. This scenario has systematically been observed [11].

3.7 Potentials

So far, we have assumed the clique potentials to be convex. This is central in the two main results of the chapter: the Theorem 1 and the regularity of energy (3.4). Both are implied by the inequality (3.20)

$$V(a) + V(c) - V(b) \geq V(a + c - b), \tag{3.20}$$

shown in Appendix (expression (A.10)), where $\min(a, c) \leq b \leq \max(a, c)$. What if we apply a function θ to the arguments of V? Using the notation $\theta(x) = x'$, we get the hypothetical inequality (3.21):

$$V(a') + V(c') - V(b') \geq V[(a + c - b)']. \tag{3.21}$$

Now, noting that, by construction[3], a, b and c differ from each other by multiples of 2π, if we choose $\theta(x) = \mathcal{P}(x) + \alpha x$, where $\mathcal{P}$ is any 2π-periodic real valued function and $\alpha \in \mathbb{R}$, (3.21) becomes,

$$\begin{aligned} V(a') + V(c') - V(b') &\geq V[\mathcal{P}(a + c - b) + \alpha(a + c - b)] \\ &= V[\mathcal{P}(a) + \alpha(a + c - b)] \qquad (3.22) \\ &= V\left[(\mathcal{P}(a) + \alpha a) + (\mathcal{P}(a) + \alpha c)\right. \\ &\quad \left. - (\mathcal{P}(a) + \alpha b)\right] \qquad (3.23) \\ &= V(a' + c' - b'). \qquad (3.24) \end{aligned}$$

Since any 2π-sampling of θ is a monotone sequence, it is guaranteed that $\min(a', c') \leq b' \leq \max(a', c')$; so, inequality (3.24) follows from (3.20). Therefore we have the following result:

[3]Stated in the proof of Theorem 1.

Proposition 1 *The set of clique potentials considered in Theorem 1 can be enlarged by admitting functions of the form $V \equiv C \circ (P + L)$, where C is a convex function, P is a 2π-periodic function, and L is a linear function.*

It should be stressed that for such a potential, the regularity condition (3.17) is also satisfied; it follows directly from (3.24). We can thus conclude that the PUMA algorithm is valid for this broader class of clique potential functions. We next give some examples of possible clique potentials.

3.7.1 The classical L^p norm

As referred back in Chapter 2, the minimum L^p norm methods form one of the main approaches to phase unwrapping. In this context, and referring to [49, p. 181], the L^p norm is given by

$$J = \sum_{\{i,j\}\in\mathcal{E}} |\phi_j - \phi_i - \Delta_{ij}|^p, \tag{3.25}$$

where $\Delta_{ij} = \mathcal{W}(\psi_j - \psi_i)$ [$\mathcal{W}$ defined in (2.2)]. These methods find a phase solution ϕ for which the L^p norm of the difference between absolute phase differences and wrapped value of wrapped phase differences (so a second order difference) is minimized. We note that this is the L^p norm of the $2\pi - quantized$ differences. We clarify this $2\pi - quantization$ operation with an example below.

In our formulation the L^p norm is given by the potential $V(\Delta\phi) = |\Delta\phi - \mathcal{W}(\Delta\psi)|^p$. Since $\Delta\phi$ and $\Delta\psi$ differ by a multiple of 2π, then $|\Delta\phi - \mathcal{W}(\Delta\psi)|^p = |\Delta\phi - \mathcal{W}(\Delta\phi)|^p$. Therefore, in our setting, we identify immediately $C(x) = |x|^p$, $\mathcal{P}(x) = -\mathcal{W}(x)$, and $L(x) = x$.

We note that the identity $V(\Delta\phi) = |\Delta\phi - \mathcal{W}(\Delta\phi)|^p$, above emphasized, may suggest that PUMA does not take data, which is given by ψ, into account. We stress that this is not the case as, in fact, PUMA (in this chapter) considers ϕ to be given, iteratively, by $\phi = 2\pi k + \psi$, $k \in \mathbb{Z}$. In particular, this means that ϕ is 2π congruent with ψ and, thus, that data is really accounted for by noting that $\mathcal{W}(\Delta\phi) = \mathcal{W}(\Delta\psi)$.

From above, we see that C is convex given that $p \geq 1$. Therefore, we conclude that, for this range of p values, PUMA exactly solves the classical minimum L^p norm phase unwrapping problem.

We refer to $Q_{2\pi}(x) \equiv -\mathcal{W}(x) + x$ as the 2π-*quantization function* and denote $V_{2\pi}(x) \equiv V\left[Q_{2\pi}(x)\right]$. Figure 3.3 plots the potential $C(x) = |x|^{1.4}$, the quantization function $Q_{2\pi}(x)$,

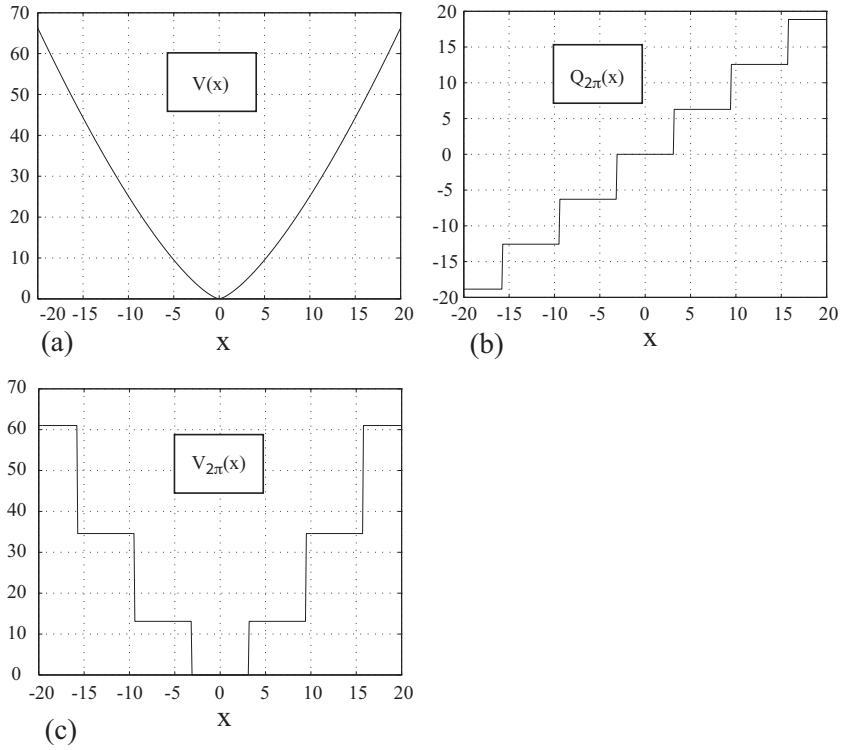

Figure 3.3: (a) The convex function $C(x) = |x|^{1.4}$; (b) $Q_{2\pi}(x) = x - \mathcal{W}(x)$; (c) The classical $L^{1.4}$ norm potential given by $V_{2\pi}(x) = C[Q_{2\pi}(x)]$.

and the classical $L^{1.4}$ norm given by $V_{2\pi}(x) = |Q_{2\pi}(x)|^{1.4}$.

3.7.2 Convex potential

Choosing any convex $C(x)$, $P(x) = 0$ and $L(x) = x$, we obviously get back to the convex potential case. For example, the quadratic clique potential $V(x) = x^2$ was used in work [36], under a Bayesian approach and a Markovian prior for the absolute phase. As already stated, this potential tends to smooth phase discontinuities.

3.8 Experimental Results

We remark that, for each of the following presented experiments, the Matlab (mixed with C++) code has been run in a 2.2 GHz Intel dual core processor, in a maximum of few dozens of seconds.

Figure 3.4 (a) displays the phase data for an MRI image (256×256 pixels) of the knee (data distributed with [49]); as we can see this is a wrapped phase image, and a phase unwrapping procedure is needed in order to obtain the desired physical information (in

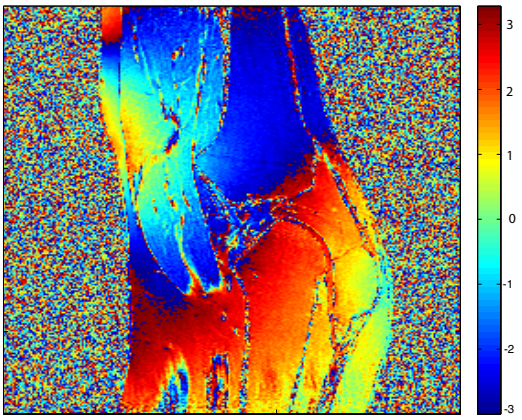

(a)

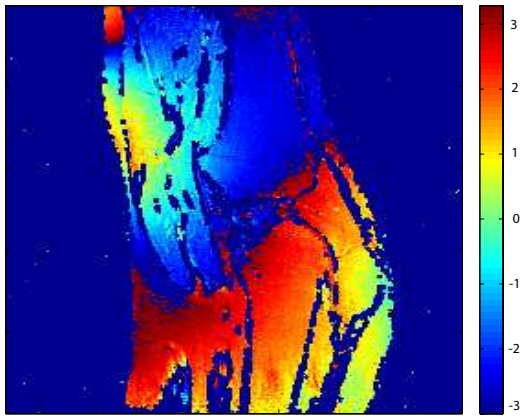

(b)

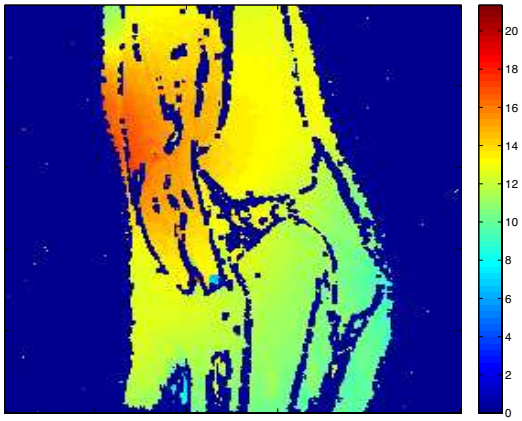

(c)

Figure 3.4: (a) MRI image of the knee (water/fat separation problem [49, 51]). (b) Image in (a) visualized with a mask (dark blue) to omit main noisy areas. (c) Unwrapped image visualized with the mask used in (b).

this example it is water/fat separation [49, 51]). The background is noisy, which poses one of the main challenges for the phase unwrapping: obtain the unwrapped solution in spite of the great amount of noisy area which might destroy it. Figure 3.4 (b) shows the same data as in (a) but now we have applied a mask only to see the phase image in areas where noise is low (dark blue means masked out area). Figure 3.4 (c) shows the unwrapped solution; for better visualization we also apply the mask used in (b). We can see that PUMA is successful at unwrapping this phase image, despite the original wide noisy area (includes mainly the background but also some regions in the interior). For this unwrapping we have chosen a quantized L^2 norm potential, which proofed to be successful.

Figure 3.5 is similar to Figure 3.4, but now it deals with an MRI image of the head (data distributed with [49]). Besides the noise, this head image, Figure 3.5 (a), has several

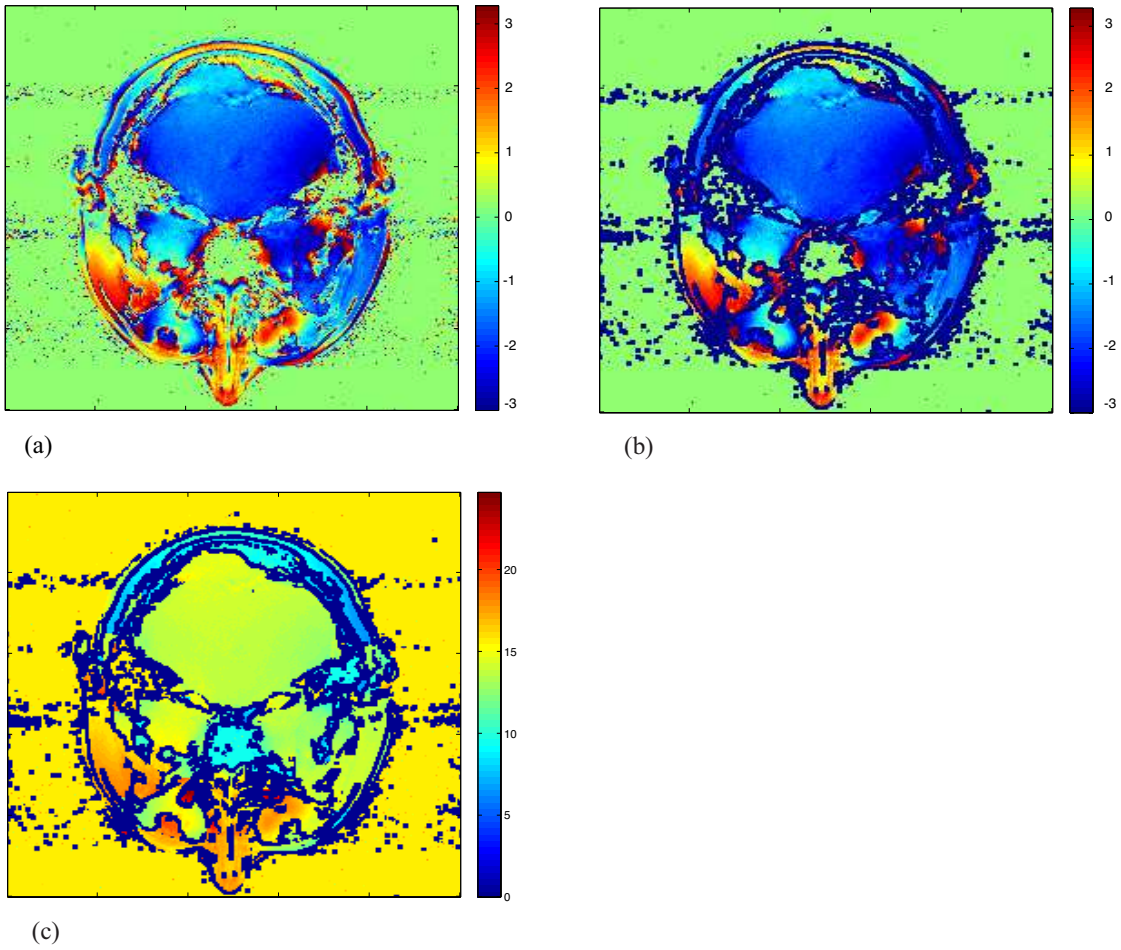

Figure 3.5: (a) MRI image of the head (water/fat separation problem [49, 51]). (b) Image in (a) visualized with a mask (dark blue) to omit main noisy areas. (c) Unwrapped image visualized with the mask used in (b).

phase regions which are almost isolated (also because of noise) from the remaining part of the image and, accordingly, pose a difficult problem. Figure 3.5 (b) shows the same data as in (a) but now we have applied a mask only to see the phase image in areas where noise is low (dark blue means masked out area). Figure 3.5 (c) shows the unwrapped solution; for better visualization we also apply the mask used in (b). PUMA is successful at unwrapping this phase image in defiance of the almost isolation of several areas inside the head. For this unwrapping we have chosen a quantized L^2 norm potential, which proofed to be successful.

Figures 3.6 (a) and 3.7 (a) display two phase images (256×256 pixels) to be unwrapped; they are synthesized from original absolute phase surfaces formed by Gaussian elevations with heights of 25π and 50π radians, respectively, and common standard deviations $\sigma_v =$

25 pixels and $\sigma_h = 40$ pixels, in the vertical and horizontal dimensions, respectively. They are represented in a linear gray scale.

The first image [Figure 3.6 (a)] has a noise whose standard deviation is 1.07 rad, thus inducing a large number of phase jumps (*residues*), making the unwrapping a hard task. Figure 3.6 (b) shows the corresponding unwrapped surface by PUMA using a non-quantized L^2 norm potential. Even with the noise induced discontinuities, PUMA successfully accomplishes a correct unwrapping (error free). We emphasize that our algorithm seeks the correct wrap-count image, so it does not intend to get rid of the possible existing noise, whatsoever. Regarding the image in Figure 3.7 (a), although there is no noise, it presents phase rates large enough to produce aliasing, such that the unwrapping becomes a hard task. Figure 3.7 (b) shows the corresponding unwrapped surface by PUMA using again a non quantized L^2 norm potential. Even with aliasing induced discontinuities, PUMA successfully accomplishes a correct unwrapping (error free). For both the unwrappings we have chosen the non quantized L^2 norm potential, as it shows a good performance regarding the unwrapping of this kind of noisy/aliased wrapped surfaces [36]. Figure 3.6 (c) shows the residues existing in the image shown in Figure 3.6 (a); white pixels are positive residues and black pixels are negative residues. We point out that it was not supplied any discontinuity information to the algorithm. Figure 3.7 (c) shows the regions of the original image, from which the image in Figure 3.7 (a) is the wrapped version, having aliasing (white pixels region). Figures 3.6 (d) and 3.7 (d) show the energy evolution along the fifteen and twenty-six iterations taken by the algorithm to perform the unwrapping of the images in Figures 3.6 (a) and 3.7 (a), respectively. It is noticeable a major energy decreasing in the first few iterations.

The last illustrating experiment for phase unwrapping with PUMA (in the convex regime) aims to characterize its performance amidst different levels of noise, different amounts of phase discontinuities, as well as benchmarking it against noteworthy phase unwrapping algorithms. Figure 3.8 (a) displays a phase image (512×512 pixels) which corresponds to "Peaks", the Matlab's example function of two variables, which is obtained by translating and scaling Gaussian elevations. In this experiment we scale the default elevations by a factor of 4. While the range of phase values for such an image is approximately 18π rad only, and it does not present any phase discontinuities, we add to it different levels of (Gaussian) noise which indeed produce phase discontinuities. Figure 3.8 (b) shows the wrapped version of the image in (a), while Fig. 3.8 (c) displays a wrapped

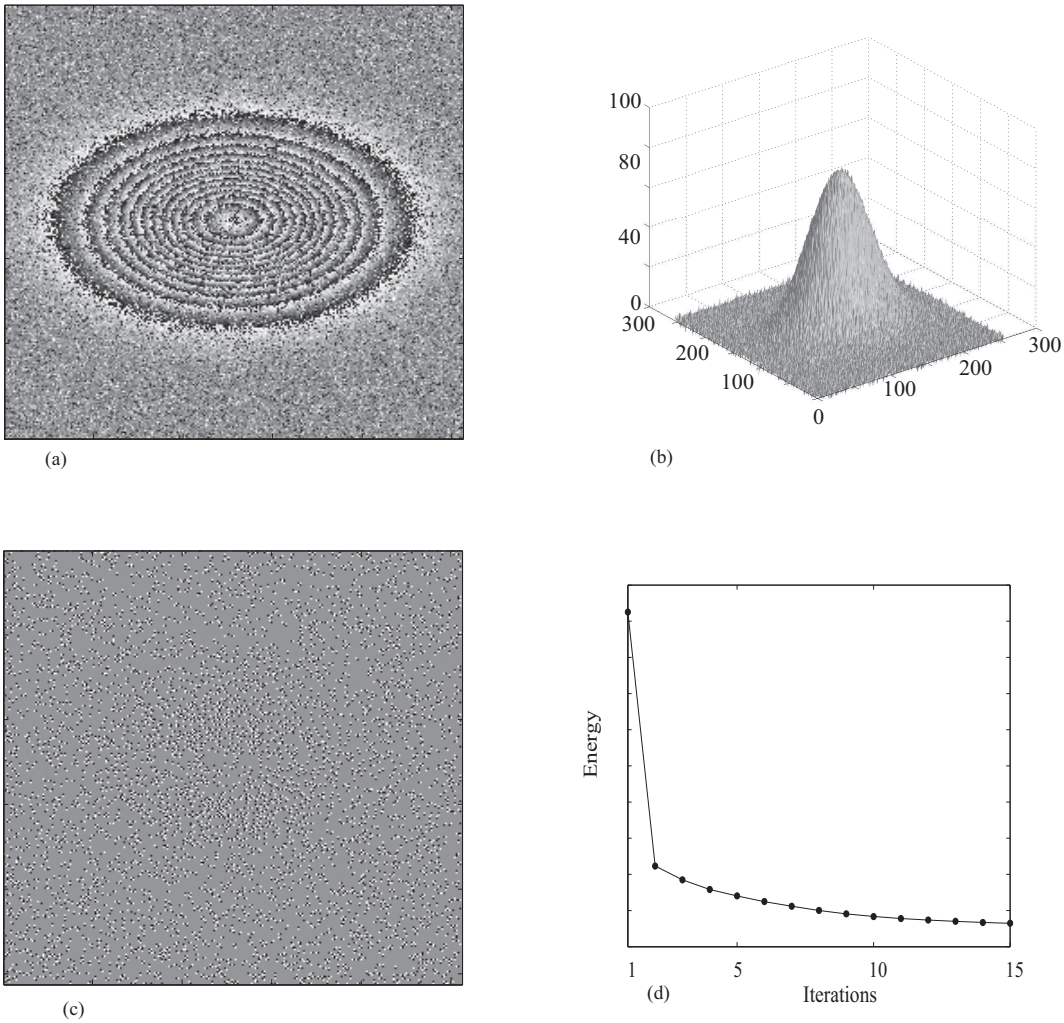

Figure 3.6: (a) Wrapped Gaussian elevation with 25π height. The associated noise standard deviation is 1.07 rad. (b) Image in (a) unwrapped by PUMA. (c) Residues in the image presented in (a): white and black pixels means positive and negative residues, respectively. (d) Energy decreasing for the unwrapping of image in (a).

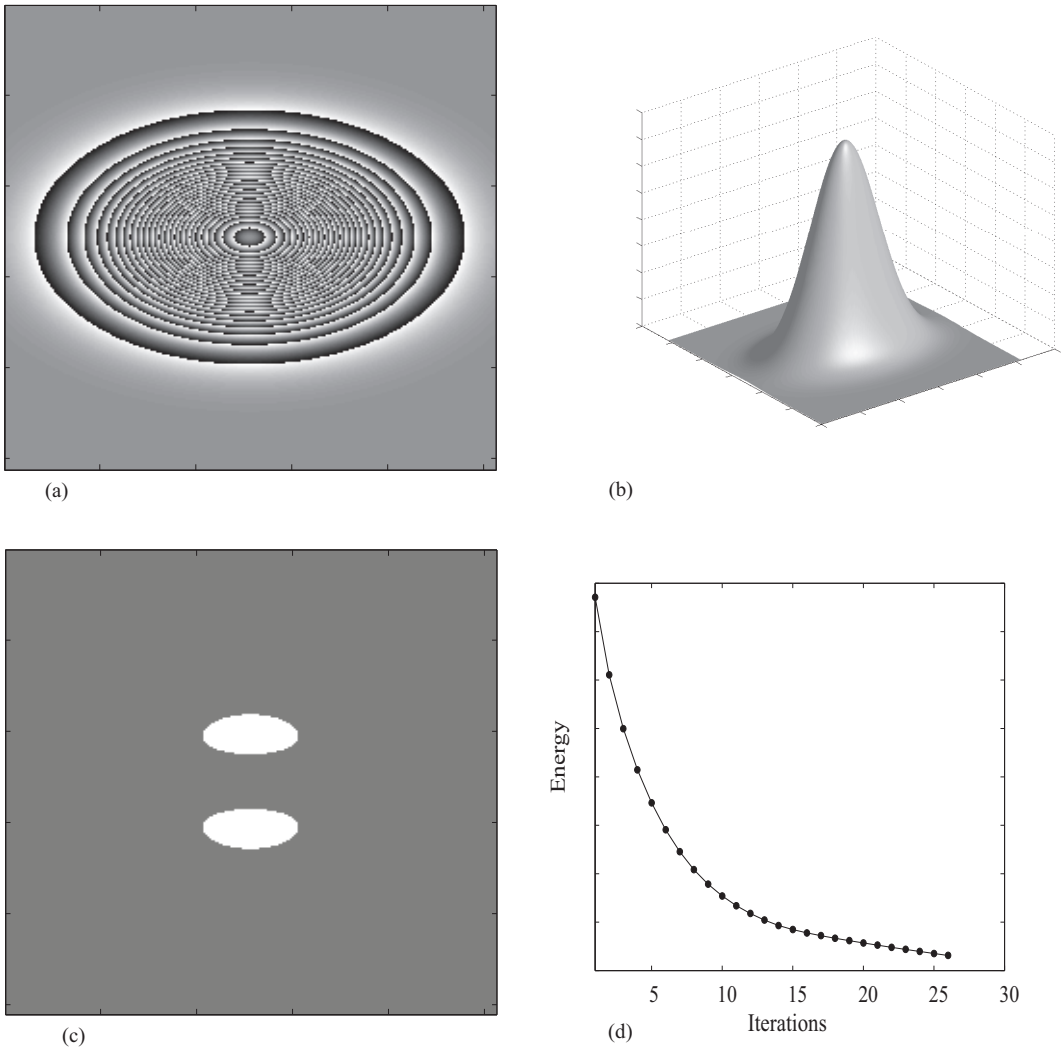

Figure 3.7: (a) Wrapped Gaussian elevation with 50π height. The associated noise standard deviation is 0 rad. (b) Image in (a) unwrapped by PUMA. (c) Aliased regions (signalled by white pixels) of the original image corresponding to the image in (a). (d) Energy decreasing for the unwrapping of image in (a).

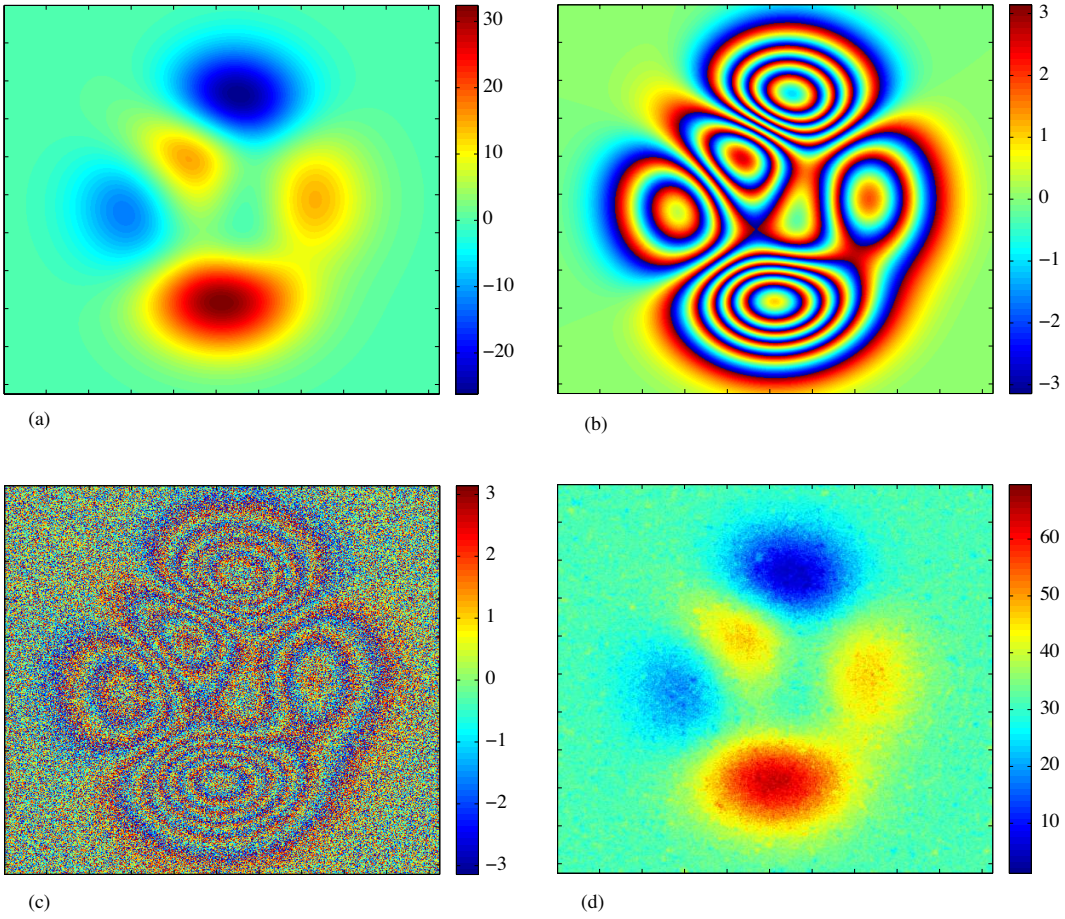

Figure 3.8: (a) The scaled Matlab's "Peaks" image. (b) Wrapped version of the previous image. (c) Noisy version of the image in (b). The standard deviation of the error is 2.14 rad (d) Unwrapped solution by PUMA: RMSE = 1.89 rad.

and highly noisy (RMSE = 2.14 rad, where RMSE stands for root mean square error, which corresponds to the standard deviation of the error image where, in this case, the error image is the difference image between noisy and noiseless wrapped images) version of that image. For such a high level of noise PUMA is still able to yield a correct unwrapping, which we show in Fig. 3.8 (d). The error, with relation to the noiseless original image, of the obtained image solution is RMSE = 1.89 rad, which is similar (lower) to the original noise.

With the aim of benchmarking we compare PUMA with noteworthy phase unwrapping algorithms, namely:

- **Path following type:** Goldstein's branch cut (GBC) [53]; quality guided (QG) [74]; and mask cut (MC) [40].

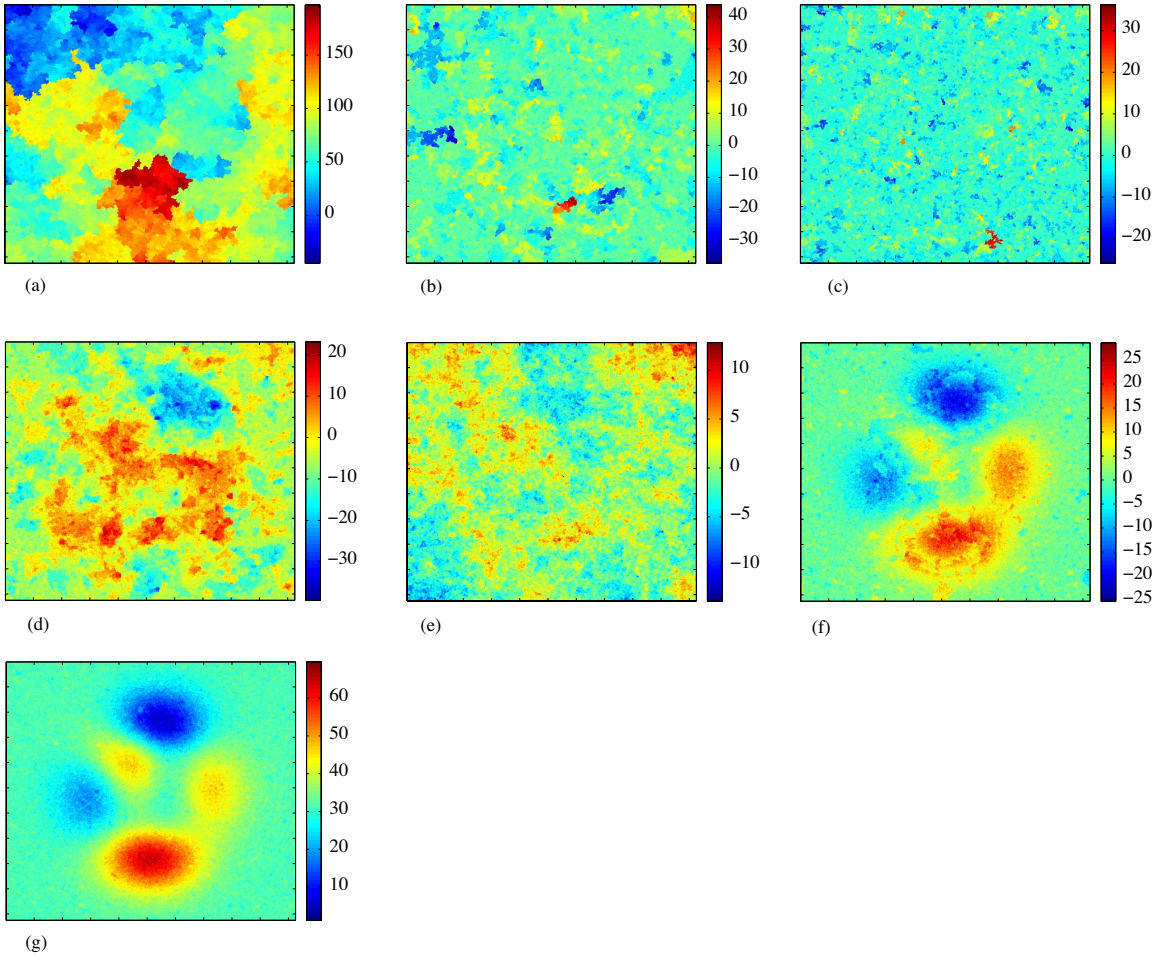

Figure 3.9: List of the phase unwrapping solutions obtained with comparing algorithms working on the scaled and wrapped "Peaks" image in a high noise scenario (std = 2.14 rad): (a) QG. (b) GBC. (c) MC. (d) FMD. (e) WLS. (f) L0N (g) PUMA. Only PUMA is able to yield a correct unwrapping.

- **Minimum norm type:** Flynn's minimum discontinuity (FMD) [41]; weighted least-squares (WLS) [50]; and L^0 norm (L0N) (see [49, Chap. 5.5]).

For such a high level of noise as the one illustrated in Fig. 3.8, std = 2.14 rad, and amongst the comparing algorithms, PUMA was the only one able to achieve a correct phase unwrapping. This is summarized in Figure 3.9, which lists the solutions yield by each algorithm. We note that, in the experiments that we have performed, all the algorithms fail for a noise higher than std = 2.14 rad. On the other hand, as we lower the noise all the comparing algorithms are progressively able to yield correct unwrappings, L0N being consistently the closest to PUMA in performance.

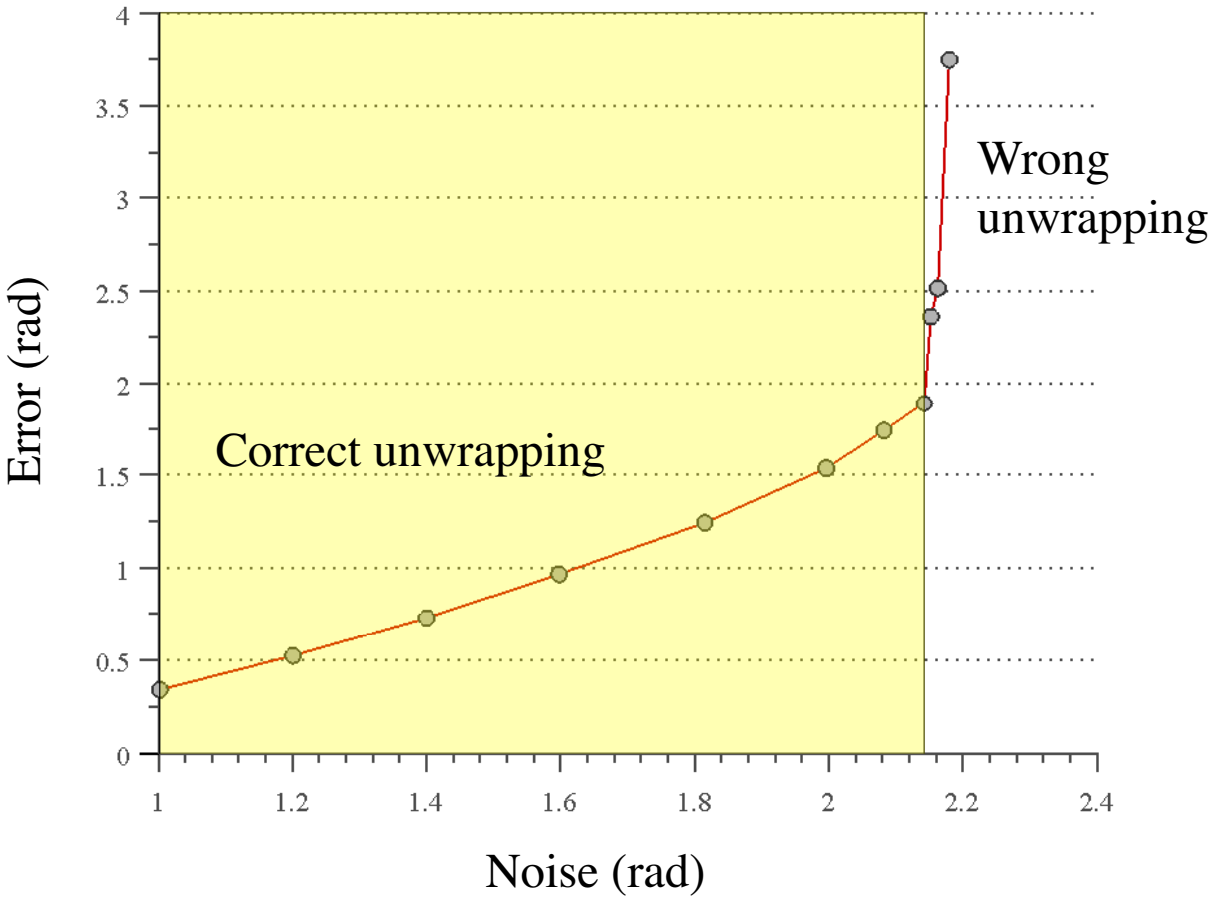

Figure 3.10: Error of the PUMA solutions for various amounts of noise in the initial wrapped images.

Figure 3.10 shows a plot of the error of the PUMA solutions for several levels of noise. The yellow shaded area corresponds to successful unwrappings. We can notice that for a noise level higher than 2.14 rad the error of the solutions grows steeply. On the other hand, in the shaded region the error of the PUMA solutions is always smaller than the noise of the correspondent wrapped images.

Finally, we observe the performance of PUMA for different amounts of aliased areas in the "Peaks" image. Figure 3.11 (a) displays the aliasing present in scaled versions of the "Peaks" image having different scale factors (from 4 to 13). White pixels correspond to the presence of aliasing. Figure 3.11 (b) shows the corresponding unwrapping PUMA solutions, which are correct for the images in the first row and wrong for the images in the second row. The error of these ten solutions is plotted in Fig. 3.12. Again the shaded

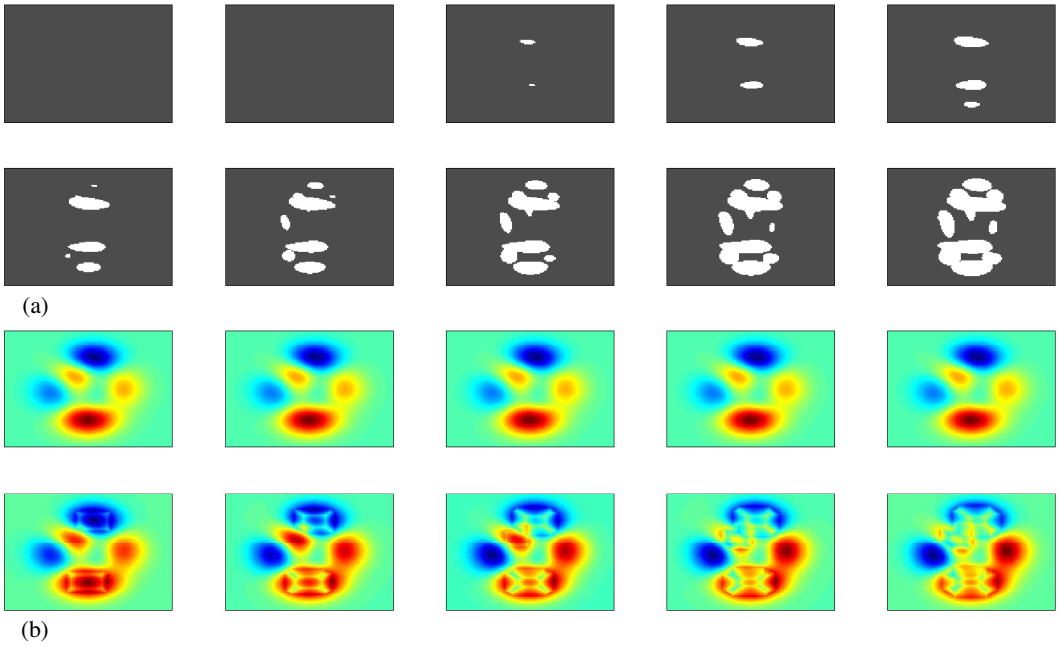

Figure 3.11: PUMA performance in the presence of aliasing. (a) Aliasing (white pixels), in ten different scaled versions of the "Peaks" image. (b) PUMA solutions for the wrapped versions of the images in (a).

area corresponds to correct unwrapping. As we can see PUMA admits some robustness to aliasing, however, from a certain point the unwrapping gets compromised in the aliasing areas.

As referred in Section 3.6, we have observed approximately an $O(n)$ complexity (where n is the size of the input image) in the experiences we have run with PUMA. Figure 3.13 illustrates this for the unwrapping of the Gaussian surface with and without noise, and employing two kinds of clique potentials.

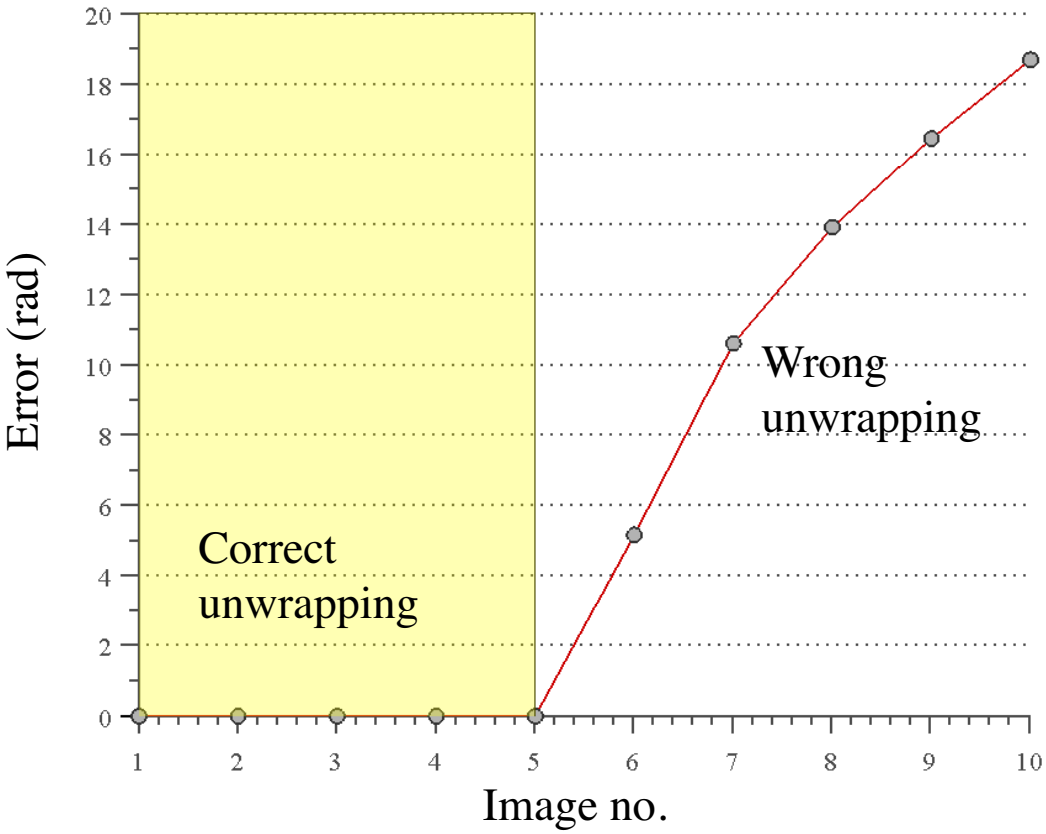

Figure 3.12: Error of the PUMA solutions listed in Fig. 3.11 (b).

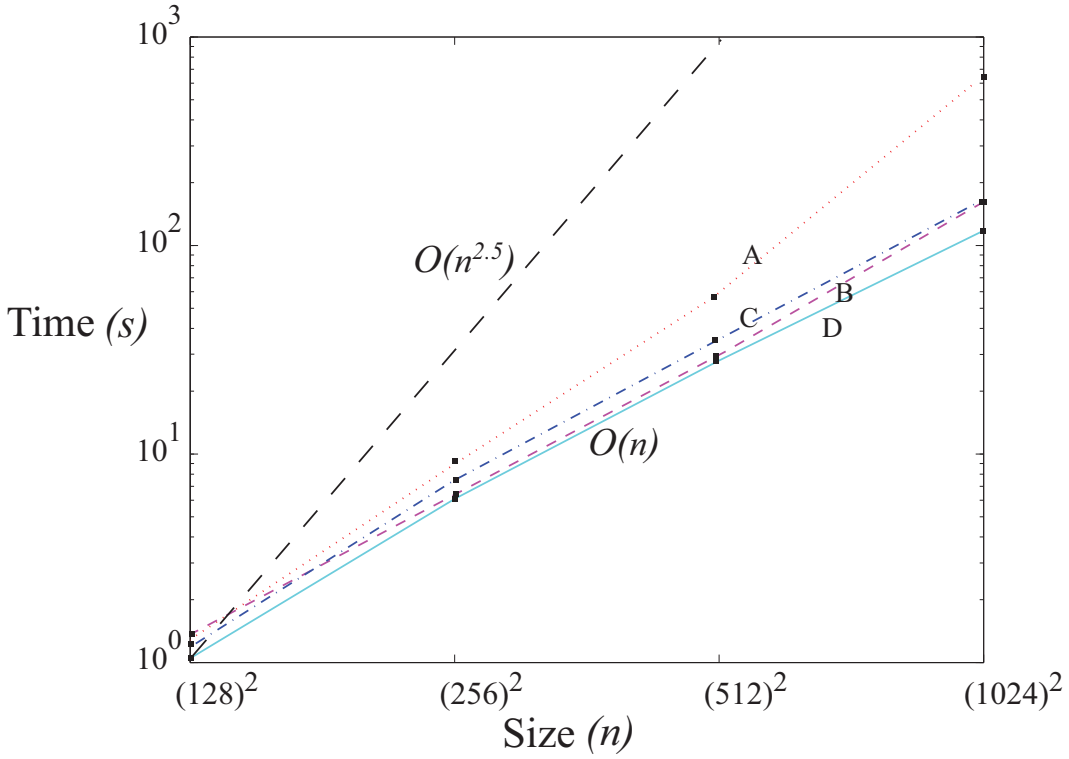

Figure 3.13: Unwrapping times of a 14π height Gaussian surface with PUMA, using a PC workstation equipped with a 2.2 GHz Intel dual core processor: time (s) vs image size (n). Time grows roughly as $O(n)$ in all the four shown experiments. An $O(n^{2.5})$ line is shown for reference. (A) Gaussian surface with 1.07 rad interferometric noise unwrapped with a non-quantized L^2 norm. (B) Gaussian surface without interferometric noise unwrapped with a non-quantized L^2 norm. (C) Gaussian surface with 1.07 rad interferometric noise unwrapped with a classical (quantized) L^2 norm. (D) Gaussian surface without interferometric noise unwrapped with a classical (quantized) L^2 norm.

Chapter 4

Phase Unwrapping: Nonconvex Scenario

4.1 Why to Use Nonconvex Potentials

In image reconstruction, and in phase unwrapping in particular, images usually show a piecewise smooth spatial arrangement; this is a consequence of the smoothness of the imaged objects themselves, and of the discontinuities introduced by their borders. These discontinuities encode, then, relevant information that should be preserved in the reconstructed image.

It is well known that, in an energy minimization framework for image reconstruction, nonconvex potentials are desirable to allow discontinuity preservation (see, *e.g.*, [71, Chap. 3] for discussion about discontinuity adaptive potentials). Figure 4.1 illustrates some examples of such edge preserving potentials, namely, a Huber potential (Figure 4.1 (a)) which is quadratic around the origin and linear elsewhere; an L^1 potential (b); a quadratic truncated potential (c); and an $L^p, (0 <= p < 1)$ potential (d). The idea of employing such potentials consists of incurring approximately in the same cost, whether the phase differences between neighboring pixels are big or small, given that they are above a certain threshold. In fact, the first two depicted potentials (Figures 4.1 (a) and (b)) are convex, yet they possess some edge preserving capabilities as, in some sense, they are almost non convex.

We should note here that, as we have shown in Section 3.7, formally, a nonconvex potential is allowed in the proposed algorithm, as long as every 2π-periodic sampling is

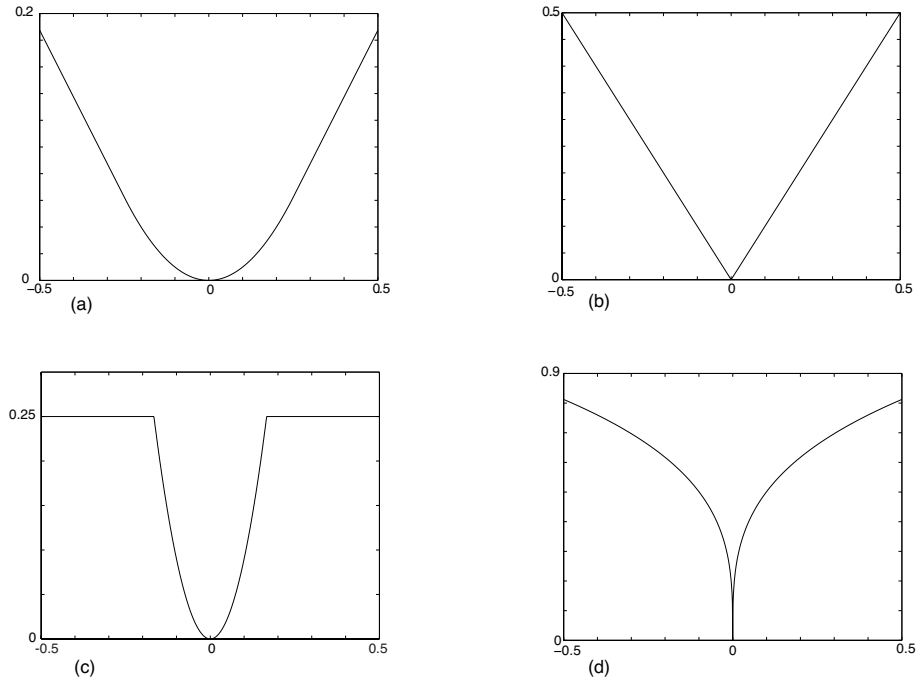

Figure 4.1: Edge preserving potentials: (a) Huber potential. (b) L^1 potential. (c) Truncated quadratic potential. (d) L^p, $0 \leq p < 1$, potential.

convex (about the issue of convex functions on discrete domains see, *e.g.*, [76]). It is, however, a trivial reasoning to conclude that this kind of nonconvex potentials are not discontinuity preserving, in our case. The alternative to nonconvex potentials, in order to preserve discontinuities, is to explicitly supply their location, which is allowed as we have already mentioned regarding expression (3.9). That is why it is said that (some) nonconvex potentials allow *blind* discontinuity preservation, *i.e.*, they preserve them without knowing where they are.

4.2 An Approximate Solution

A general nonconvex potential, nevertheless, makes the above introduced algorithm not valid and the reason is twofold. First, Theorem 1 demands a 2π-periodically convex V, *i.e.*, a potential V such that every 2π-periodic sampling of it is convex. Let us use the terminology of [99] and call a $1-$jump move the operation of adding a binary image $\boldsymbol{\delta}$; so, if V is nonconvex it is not possible, in general, to reach the minimum through 1-jump moves only. Second, as we emphasize in the sequence, it is trivial to show that, with a general nonconvex V, condition (3.17) does not hold with generality for every horizontal

and vertical pairwise interaction. This means that we *cannot* apply the energy graph-representation used in the binary optimization employed on Algorithm 3.6.

We now devise an approximate algorithm as a minor modification of PUMA to handle those two issues.

Regarding the latter, as the problem relies on the non-regularity of some energy terms $E^{ij}(\delta_i, \delta_j)$, *i.e.*, they do not verify (3.17), our procedure consists in approximating them by regular ones. We do that by leaning on majorize minimize MM [69] concepts. Assume that we still want to minimize $E(\mathbf{k}^t + \boldsymbol{\delta}|\boldsymbol{\psi})$ given by (3.15). $E(\mathbf{k}^t|\boldsymbol{\psi})$ corresponds to $\boldsymbol{\delta} = 0$ and, therefore, to $\delta_i = 0$. Consider the regular energy $E'^{ij}(\delta_i, \delta_j)$ such that

$$\begin{cases} E'^{ij}(\delta_i, \delta_j) & \geq & E^{ij}(\delta_i, \delta_j), & \text{if} \quad (\delta_i, \delta_j) \neq (0,0) \\ E'^{ij}(\delta_i, \delta_j) & = & E^{ij}(\delta_i, \delta_j), & \text{if} \quad (\delta_i, \delta_j) = (0,0), \end{cases} \tag{4.1}$$

i.e., E'^{ij} majorizes E^{ij}. Define $Q(\boldsymbol{\delta}) = \sum_{(i,j)\in\mathcal{E}} E'^{ij}(\delta_i, \delta_j)$ and $\boldsymbol{\delta}^* = \min_{\boldsymbol{\delta}} Q(\boldsymbol{\delta})$. Then,

$$E(\mathbf{k}^t + \boldsymbol{\delta}^*|\boldsymbol{\psi}) \leq Q(\boldsymbol{\delta}^*) \leq Q(\mathbf{0}) = E(\mathbf{k}^t|\boldsymbol{\psi}).$$

Therefore, the sequence $\left\{E(\mathbf{k}^t|\boldsymbol{\psi}),\, t = 0, 1, \cdots\right\}$ is decreasing.

A possible solution to obtain the replacement terms is, for instance, to increase term $E^{ij}(0,1)$ until $\left[E^{ij}(0,1) + E^{ij}(1,0) - E^{ij}(0,0) - E^{ij}(1,1)\right]$ equals zero; the corresponding graph of the Figure 3.1 has no more negative edge weights. This solution, while may not be the best (concerning energy decreasing), is the simplest to implement: by observing that $E^{ij}(0,1)$ does not enter into any of the source/sink edges in the graph, it suffices to set the (v, v') inter-pixel edge (see Section 3.5) weight to zero (thus assuring regularity).

In Figure 4.2 we illustrate this energy approximation. We recall that, using a notation abuse, $E^{ij}(\delta_i, \delta_j) = E^{ij}(\delta_i - \delta_j)$ [see (3.4) and (3.15)]. The regularity condition (3.17), thus, can be written as

$$E^{ij}(0) \leq \frac{E^{ij}(-1) + E^{ij}(1)}{2}, \tag{4.2}$$

which, being a convexity expression, means that regularity and convexity are equivalent for the energy that we are considering. Continuous convex and concave functions are shown to emphasize the regular/convex and nonregular/nonconvex parallel[1]. We note again that other energy approximations are possible and eventually even better; for instance, equally

[1]It should be noted that discrete functions $f : \mathbb{Z} \longrightarrow \mathbb{R}$ are convex *iff* there exists an extension of f, $\overline{f} : \mathbb{R} \longrightarrow \mathbb{R}$, that is also convex.

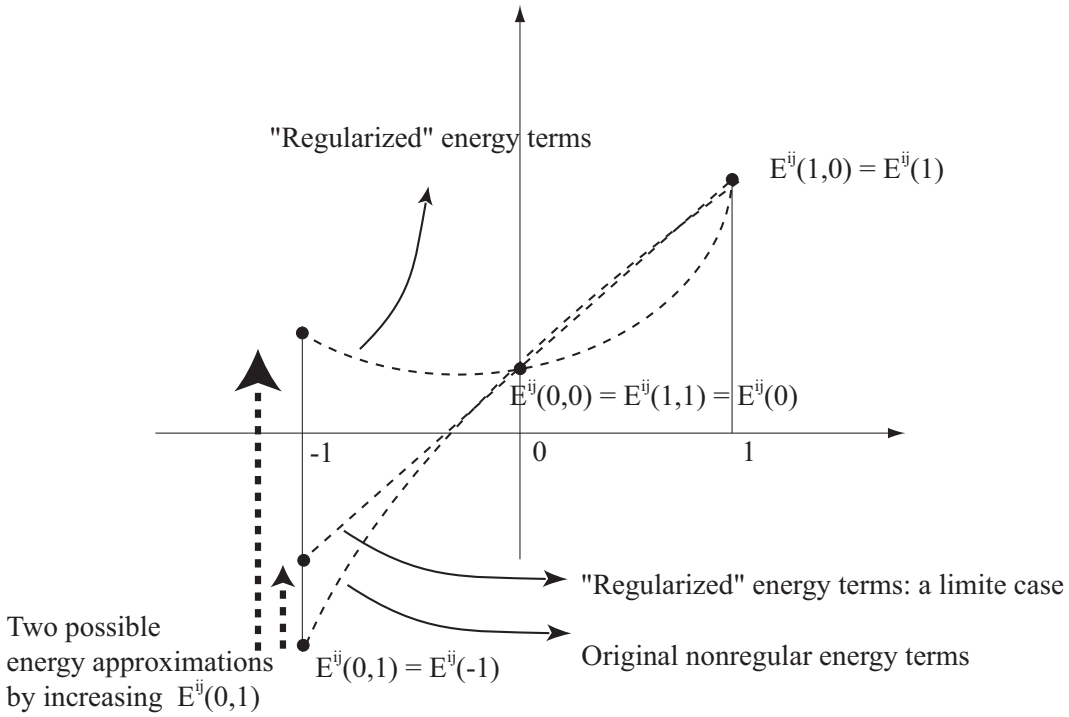

Figure 4.2: Replacing nonregular energy terms by regular ones; we end-up with an approximate energy. One of the possible approximations is to increase $E^{ij}(0,1)$.

increasing $E^{ij}(0,1)$ and $E^{ij}(1,0)$ until condition (4.2) is satisfied. This issue is however out of the scope of this work.

With respect to the first referred reason for non validity of PUMA, our strategy is to extend the range of allowed moves. Instead of only 1-jumps we now use sequences of s-jumps, which correspond to add an $s\boldsymbol{\delta}$ image (increments can have 0 or s values).

4.3 An approximate algorithm

The above presented approximate algorithm has proved outperforming results in all the experiments we have put it through; in the next section we illustrate some of that experiments. Algorithm 2 shows its pseudo-code[2].

It should be noted that the question of what particular nonconvex potential to choose is a relevant one. The main problems, in phase unwrapping, arise both from noise and from discontinuities presence. The small amplitude noise (variance smaller than π) is well described by a Gaussian density, meaning that the potentials near the origin should be

[2]We note that, preferably, the maximum jump size should be chosen to be equal to the range of values of the unwrapped surface divided by 2π. Most of the times a smaller maximum jump size is enough.

Algorithm 2 PUMA (nonconvex potentials to preserve discontinuities).

Initialization: $\mathbf{k} \equiv \mathbf{k}' \equiv \mathbf{0}$

for $s := [1, 2..., m, 1, 2, ..., m]$ (m is the maximum jump size) **do**
  possible-improvement $\equiv 1$
  while possible-improvement **do**
    Compute $E(0,0), E(1,1), E(0,1)$, and $E(1,0)$ {for every horizontal and vertical pixel pair}.
    Find non-regular pixel pairs $[E(0,1) + E(1,0) - E(0,0) - E(1,1) < 0]$. If there is any, regularize it using the MM method (for instance, set the linking edge weight to zero).
    Construct elementary graphs and merge them to obtain the main graph.
    Compute the max-flow/min-cut (S, T) {S- source set; T-sink set}.
    for all pixel (i, j) **do**
      if pixel $(i, j) \in S$ **then**
        $\boldsymbol{k'}_{i,j} = \boldsymbol{k}_{i,j} + s$
      else
        $\boldsymbol{k'}_{i,j} = \boldsymbol{k}_{i,j}$ {remains unchanged}
      end if
    end for
    if $E(\mathbf{k}'|\boldsymbol{\psi}) < E(\mathbf{k}|\boldsymbol{\psi})$ **then**
      $\mathbf{k} = \mathbf{k}'$
    else
      possible-improvement $= 0$
    end if
  end while
end for

quadratic. In what relates to larger amplitude discontinuities, they should not be too much penalized and, as such, it makes sense to employ potentials growing much slower than the quadratic. This is why it makes sense to choose half-quadratic potentials like, *e.g*, the truncated quadratic [14] and the potential used by Geman and McClure [46].

4.4 Experimental Results

In this section we present some experimental results that illustrate the performance of the above introduced algorithm. All the experiences regard very hard phase unwrapping problems, derived from both synthetic and real data. We should refer that in all the figures presenting phase images we employ a linear gray scale; we do not show a colorbar legend in the figures of this section in order to facilitate their understanding. We remark that the Matlab (mixed with C++) code has been run in a 2.2 GHz Intel dual core processor, in a maximum of few dozens of seconds.

Figure 4.3 (a) displays a phase image (150×100 pixels) to be unwrapped; it is synthesized from an original phase surface formed by a Gaussian with a 14π rad height and a clipped quarter. This quarter causes many discontinuities, which renders a very difficult phase unwrapping problem. It should be noted that we do not provide any discontinuity information to PUMA in this experiment. Figure 4.3 (b) shows the tentative unwrapped image with a classical L^2 norm. With such a potential, the computed phase is useless. Figure 4.3 (c) displays a successful, with an error of $3 \times 2\pi$ in just one pixel (the dark among white ones in the border), unwrapping in 12 iterations, for which the energy decreasing is shown in Figure 4.4 (d). Figure 4.3 (d) displays the mesh corresponding to 4.3 (c). This unwrapping was obtained using the approximate version of PUMA with the nonconvex potential depicted in Figure 4.4 (c), and a maximum jump size $m = 1$. In Figures 4.4 (a) and 4.4 (b) we show, respectively, the nonregular horizontal and vertical cliques during the first iteration of the algorithm (signalled as white). The number of nonregular cliques is relatively small (235 and 243, respectively).

Figure 4.5 (a) shows a phase image (152×458 pixels) to be unwrapped. It was obtained from an original absolute phase surface that corresponds to a (simulated) InSAR acquisition for a real steep-relief mountainous area inducing, therefore, many discontinuities and posing a very tough PU problem. This area corresponds to Long's Peak, Colorado, USA, and the data is distributed with book [49]. The wrapped image is generated ac-

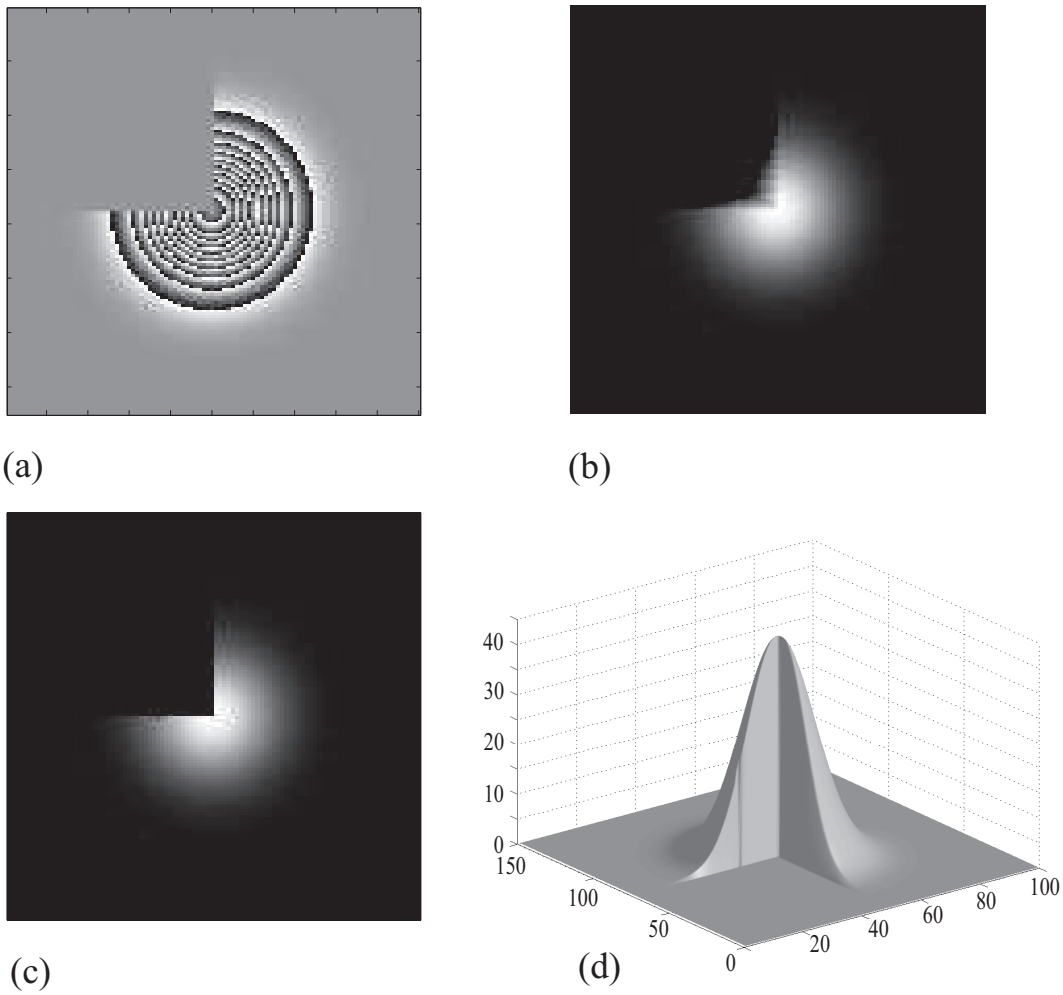

Figure 4.3: (a) Wrapped Gaussian elevation with a clipped quarter. (b) Image in (a) tentatively unwrapped with a classical L^2 norm potential. (c) Image in (a) successfully unwrapped ($3 \times 2\pi$ error in one pixel) using a nonconvex potential. (d) A "3-D" rendering of the unwrapped image.

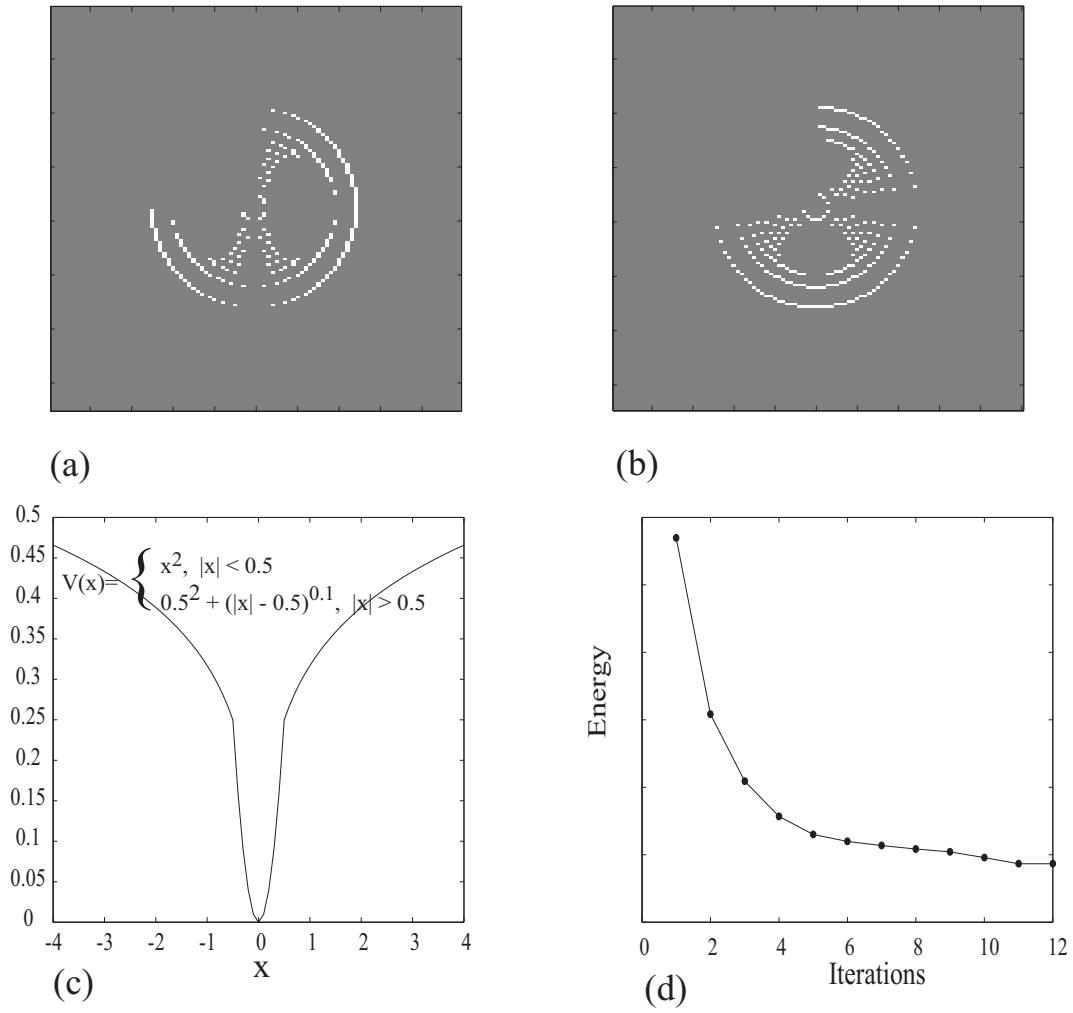

Figure 4.4: This figure refers to the unwrapping illustrated in Figure 4.3 (successful unwrapping). (a) Nonregular horizontal cliques (white signalled) during the first iteration. (b) Nonregular vertical cliques (white signalled) during the first iteration. (c) Nonregular potential employed in the unwrapping. (d) Energy decreasing along the successful unwrapping.

cording to an InSAR observation statistics (see, *e.g.*, [63]), producing an interferometric pair; by computing the product of one image of the pair by the complex conjugate of the other and finally taking the argument, the wrapped phase image is then obtained. Figure 4.5 (d) shows a quality map (also distributed with book [49]) computed from the InSAR coherence estimate (see [49, Chap.3] for further details). However, to illustrate the discontinuity blind detection and preservation ability of the PUMA method with nonconvex potentials, we have reduced, substantially, the number of supplied discontinuities to the algorithm. The corresponding quality map is shown in Figure 4.5 (c). The PU problem thus obtained is far more difficult than the original (*i.e.*, using the complete quality map) and a nonconvex potential is able to solve it. The resulting phase unwrapped is "3-D" rendered in Figure 4.5 (b), corresponding to an error norm (standard deviation of the, one dimensionally considered, image given by the difference between original and unwrapped phase images) of 0.3 radians. The unwrapping was obtained using the approximate version of PUMA, with $m = 2$. In Figure 4.5 (f) the employed non-convex and quantized potential is depicted. The correspondent analytical expression is given by $V_{2\pi}(x) = [Q_{2\pi}(x)]^{0.002}$. Figure 4.5 (e) illustrates the energy evolution with the algorithm iterations.

Figure 4.6 (a) shows another phase image (257×257 pixels) to be unwrapped, which was synthesized from an original surface (distributed with the book [49]) consisting of two "intertwined" spirals built on two sheared planes. It should be noticed that the original phase surface has many discontinuities, which make this an extremely difficult unwrapping problem, if no information is supplied about their location. The approximate version of PUMA is able to blindly unwrap this image as is shown in Figure 4.6 (b), by using a maximum jump size $m = 7$ and a nonconvex potential given by the following analytical expression:

$$V(x) = \begin{cases} 0.5^{(0.001-2)}x^2, & |x| \leq 0.5 \\ |x|^{0.001}, & |x| > 0.5 \, . \end{cases} \tag{4.3}$$

Figure 4.6 (c) shows a "3-D" rendering of the unwrapped surface and Figure 4.6 (d) shows the decreasing of the energy, along 31 iterations, in the unwrapping process.

We emphasize that we obtained a correct (error free) unwrapping except for a few (ten or so) pixels; these are pixels that in image 4.6 (a) are in the border of the two spirals and furthermore present continuity with both vertical and horizontal neighbours. This is considered an image artifact and not an error of the algorithm. We further stress that, to our knowledge, PUMA is the only algorithm able to perform this unwrapping perfectly,

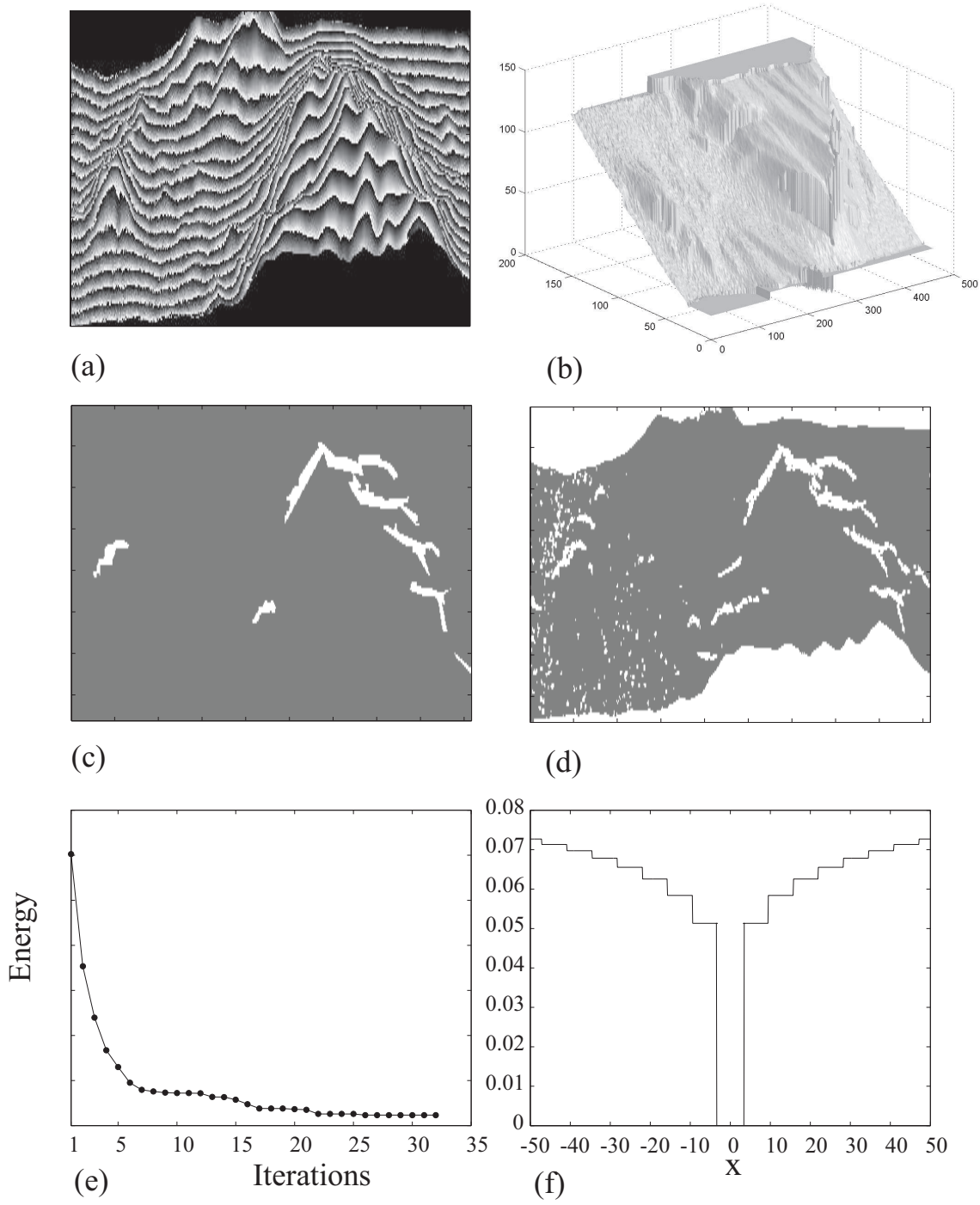

Figure 4.5: (a) Wrapped phase image obtained from a simulated InSAR acquisition from Long's Peak, Colorado, USA (Data distributed with [49]). (b) Image in (a) unwrapped by PUMA (32 iterations). (c) Discontinuity information given as input to the unwrapping process. White pixels signal discontinuity locations. (d) The total discontinuity information at disposal. White pixels signal discontinuity locations. (e) Energy decreasing for the unwrapping of image in (a). (f) The potential employed.

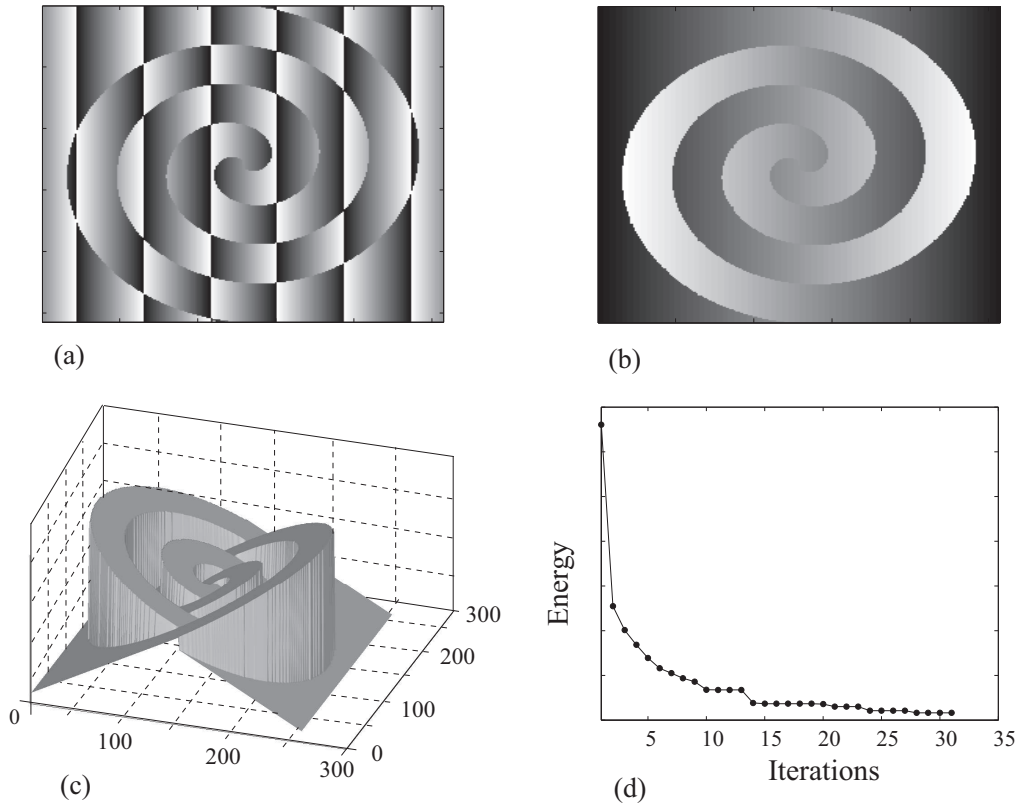

Figure 4.6: (a) Wrapped phase image corresponding to an original phase surface of two intertwined spirals in two sheared planes (Data distributed with [49]). (b) Image in (a) blindly unwrapped by PUMA (31 iterations). (c) A "3-D" rendering of the unwrapped image. (d) Energy decreasing for the unwrapping of image in (a). Notice that no discontinuities are supplied to the algorithm.

without recurring to the use of information about the location of discontinuities.

Figure 4.7 (a) shows another phase image (256×256 pixels) to be unwrapped. As in [86], it corresponds to a kind of cylinder upon a ramp and has a uniform noise of 3 radians. The result of unwrapping this image using the approximate version of PUMA is shown in Figure 4.7 (b). It was employed the nonconvex potential

$$V(x) = \begin{cases} 2^{(0.01-2)}x^2, & |x| \leq 2 \\ |x|^{0.01}, & |x| > 2 \end{cases} \tag{4.4}$$

and a maximum jump size of $m = 9$. Figure 4.7 (c) shows the pixels where the unwrapping went wrong (white pixels); it amounts to only 0.39% of the total pixels. It should be noticed that no discontinuity information was supplied to the algorithm, which employed 43 iterations along nearly 100 seconds. Figure 4.7 (d) depicts the employed potential. The results here presented show an apparent more accurate and fast phase unwrapping than those reported in [86] (note that we use 4 neighbors for each pixel).

Given the quite different problems presented above, in this and in the preceding chapter, a natural question arises: given a certain particular PU problem, what potential, scheduling and regularization parameter should be taken? Firstly, we stress that a proper answer to this question is out of the scope of the present work. However, let us remark that for the problems in Figures 3.6 and 3.7 any kind of non-quantized potential proved to work in all the experiences we have put it through; regarding Figure 4.3, we found that most of the potentials with exponent less than one are suitable; with respect to Figures 4.5 and 4.7, a more fine tuning of an appropriate potential had to be carried out, and finally, to attain a successfull solution of the difficult problem presented in Figure 4.6, an even more thorough fine tuning was required. Regarding scheduling, a similar pattern of tuning needs was found; the values presented in this work proved to give the smallest schedules good enough to solve the problems. Finally, the regularization parameter was also hand tuned to get the best results. Although we put emphasis in that PUMA algorithm allows a large family of potentials and move spaces, which gives flexibility to address different phase unwrapping problems, the question of finding the most suitable ones (as well as the best balance between the data and prior terms, *i.e.*, the best regularization parameter) is relevant and to be addressed in the future.

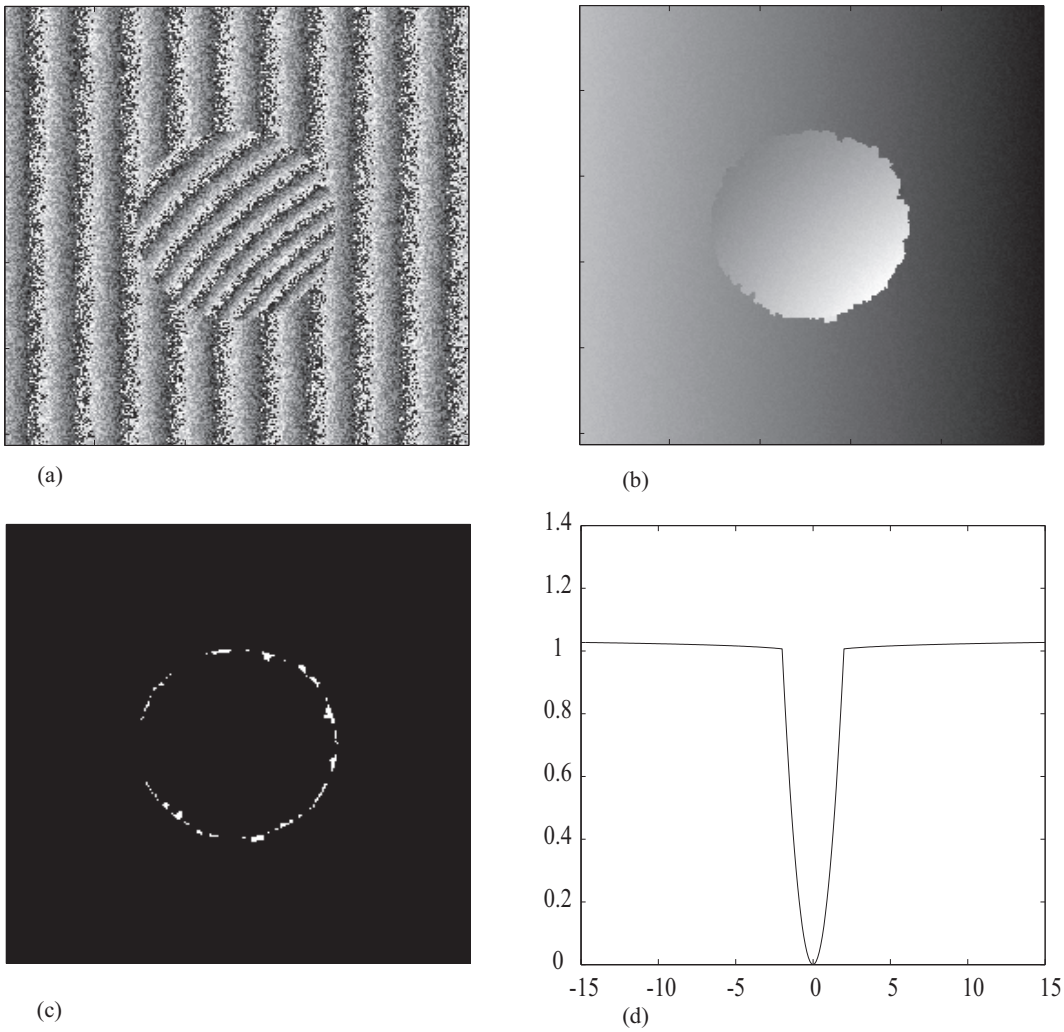

Figure 4.7: (a) Wrapped phase image corresponding to an original phase surface given by a kind of cylinder upon a ramp. In all the image there is a uniform noise of 3 radians (data reported in [86]). (b) Image in (a) blindly unwrapped by PUMA (43 iterations). (c) 0.39% of the total number of pixels (shown in white) had a wrong unwrapping. (d) The potential employed.

Table 4.1: Root Mean Square Error (rad).

Experiments	Algorithms						
	PUMA	GBC	QG	MC	FMD	WLS	L0N
Clipped Gaussian	0.15	1.08	0.36	2.16	1.23	5.99	5.41
Long's Peak	0.30	8.12	12.02	14.77	0.50	1.14	0.48
Spirals	0	29.36	33.50	33.57	33.51	33.80	33.44
Cylinder on plane	1.53	6.07	12.34	16.95	8.61	14.82	12.00

4.4.1 Benchmarking

In this section we benchmark the version of PUMA approach introduced in this chapter (Algorithm 2) against several state-of-the-art and representative algorithms. The benchmarks are evaluated on the experiments addressed in the previous sections. Table 4.1 summarizes the quantitative results obtained for the benchmarks. The performances of the algorithms are measured by the RMSE (root mean squared error), *i.e.*, the standard deviation of the absolute error between original and unwrapped phase images. The comparing algorithms are the same that were considered in Chapter 3, namely:

- **Path following type:** Goldstein's branch cut (GBC) [53]; quality guided (QG) [74]; and mask cut (MC) [40].
- **Minimum norm type:** Flynn's minimum discontinuity (FMD) [41]; weighted least-squares (WLS) [50]; and L^0 norm (L0N) (see [49, Chap. 5.5]).

The obtained results clearly illustrate the competitiveness of PUMA with relation to state-of-the-art algorithms.

We note the following:

1. PUMA's performance is systematically the best for the shown experiments.
2. PUMA is the only algorithm that is able to unwrap the intertwined spirals image. Furthermore, it does that perfectly, while all the other fail totally. We emphasize that this is an extremely hard phase unwrapping problem as no information on the tricky discontinuities is given.
3. The only algorithm which is able to unwrap the *cylinder on plane* image is PUMA. All the other benchmarked algorithms fail, which is reflected on their RMSE values.

We emphasize that this is also a very difficult phase unwrapping problem, as it presents many original discontinuities plus noise derived ones; moreover, the non-alignment with horizontal and vertical directions brings additional difficulties.

Chapter 5

Phase Unwrapping and Denoising

5.1 Motivation

We have presented, in the two previous chapters, two algorithms for our PUMA approach (tackling convex and nonconvex potentials, respectively). For both we have shown experimental results involving noisy data, in which the phase unwrapping was successful and *in that sense* we dealt with noise. Regarding some of the resulting unwrapped images, they appear noisy which is far from the ideal for usual real applications. This brings us to consider denoising. The pertinence of this operation is transversal to all imaging technologies and constitutes by itself a broad independent research topic. Being so, our interest goes beyond applying the existing state-of-the-art techniques: we seek an extension of the PUMA approach that yields useful denoising. The main two characteristics of the proposed solution are the following:

1. Contrarily to the majority of the phase unwrapping formulations that also perform denoising, the so-called absolute phase estimation methods, we opt for applying unwrapping before denoising. By using a discontinuity preserving prior, PUMA not only infers the 2π multiples of the absolute phase, but also, implicitly, detects the discontinuity locations as we have shown in Chapter 4. This is a crucial information for the effectiveness of the phase denoising, that would eventually not be available if this step was applied prior to unwrapping. This way, we avoid the denoising step to erroneously take important phase information by noise.

2. Both phase unwrapping and denoising share the same rationale. This is achieved through the proposal of a multiprecision version of the optimization algorithms previ-

ously presented. The multiprecision principle improves the performance by decreasing the complexity of the algorithm. The denoising inherits the fast performance from the max-flow algorithms.

5.2 Multiprecision Solution

Revisiting Section 3.1 we can see that the MAP estimation of the absolute phase is given by minimizing the *energy* given by (5.1),

$$E(\boldsymbol{\phi}) \equiv \underbrace{\sum_{i\in\mathcal{V}} -\lambda_i \cos(\phi_i - \psi_i)}_{\text{Data fidelity term}} + \mu \underbrace{\sum_{\{i,j\}\in\mathcal{E}} V_{i,j}\,(\phi_i - \phi_j)}_{\text{Prior term}}, \tag{5.1}$$

which we emphasize as being a hard task as both data fidelity and prior terms are non-convex (in general).

We note that $\boldsymbol{\phi}$ represents the set of optimization variables, and $\boldsymbol{\psi}$ stands for the noisy observations. These two sets are linked through the data fidelity terms (the observation model). Our purpose is to reconstruct the observed phase $\boldsymbol{\psi}$, mitigating the perturbation of noise. In order to achieve that, we address the MAP estimation problem considering that $\boldsymbol{\phi}$ is a set of continuous variables, whose (MAP) estimate is tackled via a greedy and multi-precision technique, which yields an approximate solution.

First unwrap then denoise

Sometimes we may be just interested in computing the 2π multiple in the representation $\phi_i = \psi_i + 2\pi k_i$, which amounts to be the phase unwrapping problem. A way of thinking about how to obtain the unwrapped solution is that, since the data fidelity term, $D_i(\phi_i = \psi_i + 2\pi k_i) = -\lambda_i$, does not depend on k_i, then the unwrapping optimization problem consists in minimizing the prior term of (5.1) with respect to $\phi \in \prod_{i\in\mathcal{V}}\{\psi_i + 2\pi k_i \,:\, k_i \in \mathbb{Z}\}$. In Chapters 3 and 4 we have introduced a descent method that, depending on the potentials, yields exact (in the case of convex potentials) or approximate (in the case of nonconvex potentials) solutions. Each step of the method solves a binary problem by computing the min-cut of an appropriate graph. We apply this method in this chapter, first for phase unwrapping and then similarly for multiprecision schedules, as will be clear in the sequence.

Multiprecision optimization

We note that the basic phase unwrapping step can be viewed as a discretization of the original domain, using a sampling interval of 2π. A consequence of this discretization is that the resulting objective function is easier to deal with since, for $\phi \in \prod_{i\in\mathcal{V}}\{\psi_i + 2\pi k_i : k_i \in \mathbb{Z}\}$, it does not depend on the nonconvex data terms $-\lambda_i \cos(\phi_i - \psi_i)$.

After the unwrapping step, we get absolute phase estimates given by $\widehat{\phi}_i = \psi_i + 2\pi\widehat{k}_i$. Even if the integer image estimate is exact, we still have error in $\widehat{\phi}_i$ due to the noise present in ψ_i [see expression (3.2)]. In order to filter out the noise, we compute a sequence of binary descent optimizations using a multi-precision schedule. The precision $q \in \{0, 1, \ldots, N\}$, corresponds to a sampling interval of $\Delta = 2\pi/2^q$. Thus, the coarser precision implements phase unwrapping and the following denoising. Each of these binary descent optimizations is achieved through the graph mincut method used in the previous two chapters.

We highlight the following qualitative characteristics of the approach just described:

1. The PUMA algorithm proposed in Chapter 4, used for phase unwrapping, is able to deal with discontinuities and implicitly locate them.

2. The PUMA solution for phase unwrapping yields an error much smaller than π in magnitude in most of the pixels.

3. Given that for precisions $q > 0$, we have, for most $i \in \mathcal{V}$, $|\phi_i - \psi_i| \ll \pi$, then most of the unary terms $-\lambda_i \cos(\phi_i - \psi_i)$ behave as convex functions, rendering a much easier optimization problem.

One expectable advantage of coarse-to-fine multi-precision schedule is computation time. However, in our scenario this may not be, perhaps, the most important feature: owing to the nonconvexity of the problem, the algorithm would have, very likely, got stuck in a local minimum if we had begun with the highest precision.

5.3 Multiprecision algorithm

Algorithm 3 shows the pseudo-code for the multiprecision optimization, where we use the following sets:

$$\begin{aligned} M^U(\phi', \Delta) &\equiv \left\{\phi \in \mathbb{R}^{|\mathcal{V}|} : \phi_i = \phi'_i + \delta_i\Delta\right\}, \\ M^D(\phi', \Delta) &\equiv \left\{\phi \in \mathbb{R}^{|\mathcal{V}|} : \phi_i = \phi'_i - \delta_i\Delta\right\}, \end{aligned}$$

$\delta_i \in \{0,1\},\ \Delta \in \mathbb{R}$, and where we use $\tilde{E}(\phi)$ to represent the energy approximation introduced in chapter 4 (a regular approximation), which is needed to allow the energy to be graph representable. The construction of $\tilde{E}(\phi)$ is illustrated in Figure 4.2.

Algorithm 3 PUMA (phase unwrapping plus denoising).

Initialization: $\phi = \psi$ {Interferogram}, successup = false, successdown = false

for $\Delta = 2\pi \times \left\{2^0, 2^{-1}, \ldots, 2^{-N}\right\}$ **do**
  while (successup = false OR successdown = false) **do**
    if successup = false **then**
      $\hat{\phi} = \arg\min_{\hat{\phi} \in M^U(\phi,\Delta)} \tilde{E}(\hat{\phi})$
      if $E(\hat{\phi}) < E(\phi)$ **then**
        $\phi = \hat{\phi}$
      else
        successup = true
      end if
    end if
    if successdown = false **then**
      $\hat{\phi} = \arg\min_{\hat{\phi} \in M^D(\phi,\Delta)} \tilde{E}(\hat{\phi})$
      if $E(\hat{\phi}) < E(\phi)$ **then**
        $\phi = \hat{\phi}$
      else
        successdown = true
      end if
    end if
  end while
end for

Our algorithm engages in a greedy succession of up and down binary optimizations. The precision interval Δ starts with the value 2π and ends with the value $2\pi/(2^N)$, where N is a depth of precision. In order to characterize the algorithm, we start assuming $E(\phi) = \tilde{E}(\phi)$ and the terms D_i and $V_{i,j}$ in expression (5.1) to be convex. Then, for each precision interval Δ, Algorithm 3 finds, in finite time, a minimizer of E in a grid of size Δ. More precisely, we have

Theorem 2 *If the unary and pairwise terms of E, defined in (5.1), respectively, $D_i(\cdot)$, for*

$i \in \mathcal{V}$, and $V_{ij}(\cdot)$, for $(i,j) \in \mathcal{E}$, are convex, then, at a given precision interval $\Delta = 2\pi/2^q$, for $q \in \{0,\ldots,N\}$, the following holds:

1. *The output of the loop "***while***" is a minimizer of $E(\phi)$ in the set $\left\{\phi \in \mathbb{R}^{|\mathcal{V}|} : \phi_i = \psi_i + z_i\Delta,\ z_i \in \mathbb{Z}\right\}$.*

2. *The number of "***while***" iterations at each precision $q \in \{0,\ldots,N\}$ is bounded by $K_q + 1$, where $K_q = K_0 2^q$ is the range of the 2π multiples variables at precision q.*

Proof: See the Appendix.

Complexity

As already pointed out, we solve the binary minimizations displayed in lines 5 and 14 of Algorithm 3 by computing min-cuts on appropriate graphs. Denoting by $T(n,m)$ the worst-case complexity of the used min-cut algorithm, where n is the number of graph nodes and m the number of edges, and recalling from Theorem 2 that K_q represents the range of the 2π multiples variables at precision q, then Algorithm 3 takes the worst-case pseudo-polynomial time $O\left(K_q T\left(n,m\right)\right)$ to find a minimum of E at the precision q.

The rationale underlying the multi-precision minimization is that of a minimum length search for a minimizer of E. Still considering the convex scenario, given a minimizer at a precision q, say ϕ^q, there exists a minimizer at the precision $q+1$ such that $\|\phi^q - \phi^{q+1}\|_\infty < n$ [76, Theorem 7.18], where $\|x\|_\infty \equiv \max_i |x_i|$ is the l^∞-norm of x. Therefore, the algorithm takes at most n iterations to find a minimizer at resolution $q+1$ (see Chapter 3). Consequently, the number of iterations to find a minimizer of E is bounded by $O(n \log K_N)$. In practice, we have observed systematically $\|\phi^q - \phi^{q+1}\|_\infty \ll n$, and very often we have $\|\phi^q - \phi^{q+1}\|_\infty < 2$, making the algorithm highly efficient from the time complexity point of view. This behavior is illustrated in Figure 5.1 (c), where we show the evolution of Algorithm 3 in a convex scenario, both with and without multi-precision. Notice that in the former case the number of "up and down"iterations (lines 6 and 14 of Algorithm 3) to find a minimum, in a given precision, is $2 \times (K_q + 1)$.

5.4 Experimental Results

We remark that matlab (mixed with C++) code has been run in a 2.2 GHz Intel dual core processor, in a maximum of few dozens of seconds.

5.4.1 Illustrating multi-precision

Figures 5.1 and 5.2 illustrate the virtues of employing a multi-precision approach. In Figure 5.1 we intend to illustrate the pure effect of algorithm's speed enhancing. Let us recall the general energy expression (3.3)

$$E(\phi) \equiv \underbrace{\sum_{i \in \mathcal{V}} D_i(\phi_i)}_{\text{Data fidelity term}} + \mu \underbrace{\sum_{\{i,j\} \in \mathcal{E}} V_{i,j}\left(\phi_i - \phi_j\right)}_{\text{Prior term}}, \tag{5.2}$$

for which we now set $D_i(\phi_i) = |\phi_i - \psi_i|^2$, instead of the sinusoidal nonconvex observation data model, and $V_{i,j}\left(\phi_i - \phi_j\right)$ as being a convex prior potential. Therefore, we are dealing with a convex energy. In this example, ψ plays the role of a noisy observation of ϕ in a Gaussian additive model. Figure 5.1 (a) shows an image that corresponds to a discretized pyramid with additive Gaussian noise ($\sigma = 1$). Figure 5.1 (b) shows the image in Figure 5.1 (a) denoised by applying Algorithm 3; the result is very good. Fig. 5.1 (c) illustrates the energy decreasing versus iterations. The curve with marks on it represents the energy evolution by using multi-precision; each mark corresponds to a change of precision. The other curve corresponds to a performance of the algorithm in the finest precision from the beginning. It can be seen that both ways we end up with the same energy (and in fact the same denoised image), as expected by using a convex energy function; however, multi-precision turns the algorithm much faster. In Figure 5.2 we illustrate the phase unwrapping plus denoising by getting back to the energy (5.1) employed for phase unwrapping (with the sinusoidal observation data model), and a prior potential identical to a truncated quadratic [14]. Figure 5.2 (a) shows the wrapped phase corresponding to a true phase given by a clipped Gaussian with 14π rad height. Figure 5.2 (b) shows a perfect unwrapping obtained by Algorithm 3 using the multi-precision approach. Figure 5.2 (c) displays the completely failed unwrapping that one obtains by running the algorithm with the finest precision from the very beginning. Finally, Figure 5.2 (d) displays the energy evolutions either with and without multi-precision; the curve with marks on it corresponds to the multi-precision run (each mark represents a precision change). These plots illustrate that multi-precision avoids the poor energy local minima that are obtained without multi-precision. Again multi-precision enhances the speed of the algorithm.

In the next section, we present a series of experiments illustrating the effectiveness of the proposed approach in absolute phase estimation (phase unwrapping plus denoising).

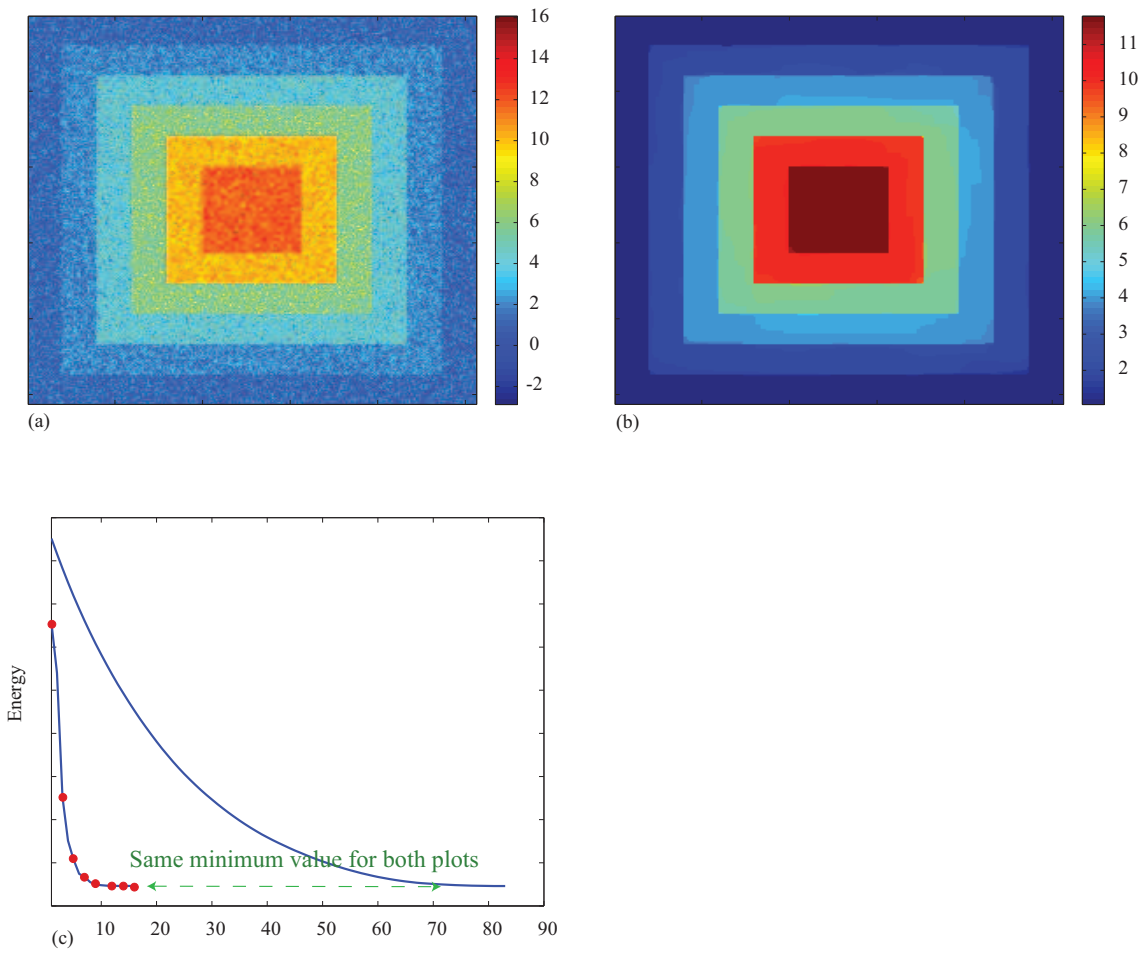

Figure 5.1: (a) Discretized pyramid with additive Gaussian noise ($\sigma = 1$). (b) Image in (a) denoised by Algorithm 3 (convex energy). (c) Energy decreasing vs iterations regarding (b): marks mean increase of precision; the other curve corresponds to using the finest precision only.

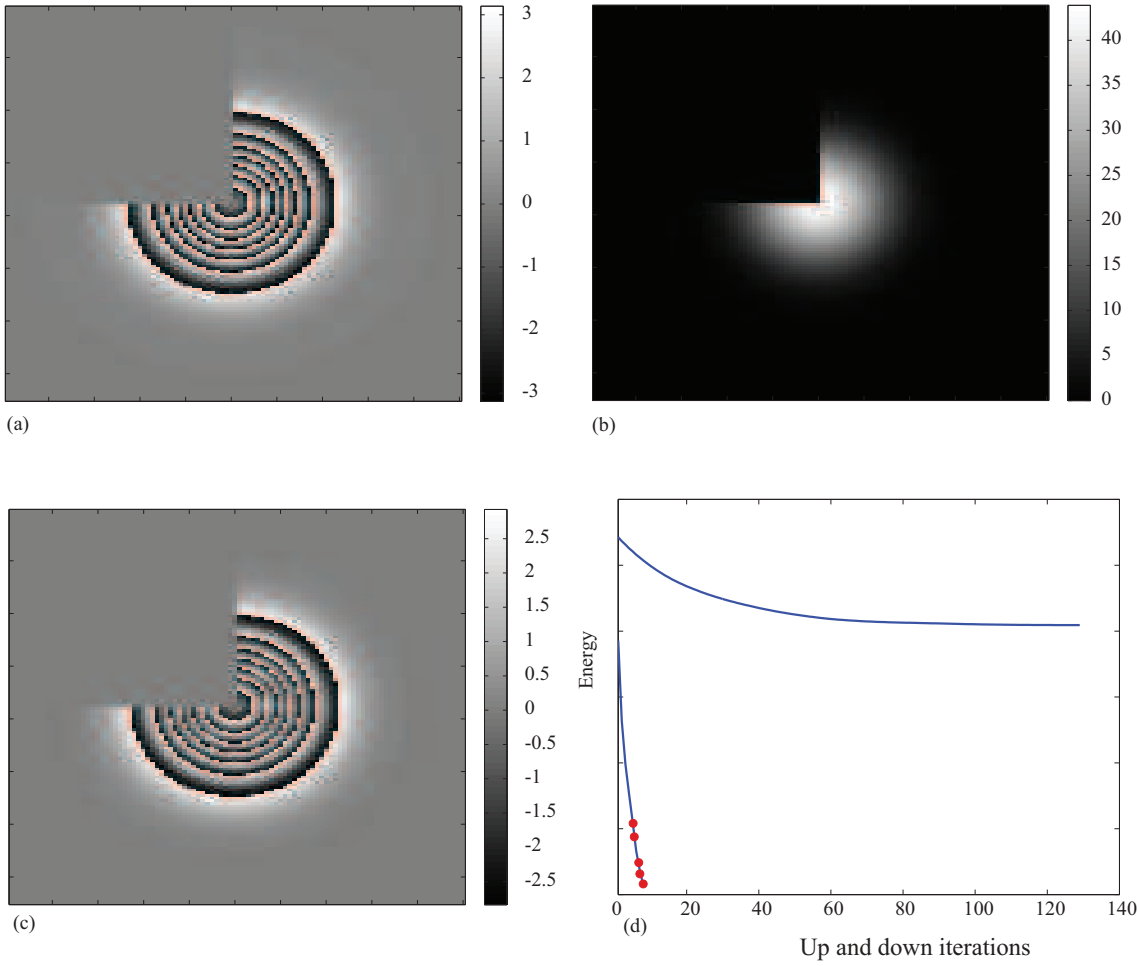

Figure 5.2: (a) Wrapping of a clipped Gaussian with 14π rad height. (b) Perfect unwrapping obtained by Algorithm 3 using multi-precision approach. (c) Completely failed unwrapping by running the algorithm with finest precision only. (d) Energy evolution either with and without multi-precision [(b) and (c) respectively]; marks mean increase of precision; the other curve corresponds to using the finest precision only.

5.4.2 Phase unwrapping plus denoising

We present four experiments illustrating the performance of the proposed algorithm. With the exception of the first one, all of them concern absolute phase surfaces which have appeared in the experimental results shown in previous chapters. We made such a choice in order to simplify future benchmarkings. The first three concern synthetic data [generated according to the model shown in (3.1) and with $A = 1$] and the fourth deals with the InSAR data distributed with [49], which is a commonly used benchmark to score absolute phase estimation algorithms. In all the experiments, we employ a depth of precision (see Algorithm 3) $N = 8$, which gives a minimum precision interval of $2\pi/2^8$ rad $\simeq 2.5 \times 10^{-3}$ rad. The regularization parameter μ [see (3.4)] was hand tuned for the best performance. Regarding the potentials we use half-quadratic type potentials (5.3),

$$V(x) = \begin{cases} |x|^2 & \text{if} \quad |x| \leq \pi \\ \pi^2 - \pi^p + |x|^p & \text{if} \quad |x| > \pi \end{cases}, \tag{5.3}$$

with $0 < p < 1$ and thus nonconvex, or either, quadratic potentials (given by the same expression by choosing $p = 2$). We furthermore refer that in the four experiments the regularization parameter was chosen to take values in the set $[0.2, 0.4]$, and that the exponent p was chosen to take values close to 0.5, when the original absolute phase has discontinuities, and equal to 2 when there are no discontinuities. These values of p conform with the introduced rationale: to preserve discontinuities, the exponent p of the half quadratic potential, must satisfy $p < 1$, and thus the potential is non-convex. On the other hand, if there are no discontinuities to preserve, convex potentials are preferable, (*e.g.*, $p = 2$), as they impose smoothness on the estimated surfaces and lead to easier optimization problems.

We consider the following error measures:

1. $\text{RMSE} \equiv \text{std}(\hat{\phi} - \phi)$,
2. $\text{ISNR} \equiv 10 \log 10 \frac{\left\| e^{j\phi} - e^{j\psi} \right\|^2}{\left\| e^{j\hat{\phi}} - e^{j\psi} \right\|^2}$,

where, as usual, ϕ is the true absolute phase, ψ the noisy wrapped phase, $\hat{\phi}$ the estimated absolute phase, and $\text{std}(\cdot)$ denotes the sample standard deviation. RMSE (root mean squared error) is a measure of the total error, whereas this definition for ISNR (improvement in signal to noise ratio), introduced in [7], is a measure of the noise reduction independent of the phase unwrapping.

Synthetic data

In this section, the standard deviation of the Gaussian noise is set to $\sigma = 0.5$ which corresponds to a signal to noise ratio SNR $\equiv 1/\sigma^2$ [see generation model (3.1)] of 6.02 dB. We should remark that in this scenario, which poses a very hard task given the amount of noise, we have run for each experiment a *Monte-Carlo* simulation with ten iterations.

Figure 5.3 (a) displays an image (100×150 pixels) corresponding to an absolute phase surface formed by two equal sized planes with slopes, respectively, of 1 and 0 rad/pixel: the so-called sheared ramp (maximum height difference is 99 rad); Figure 5.3 (b) displays the image shown in (a) wrapped and noisy; Figure 5.3 (c) shows the image in (b) unwrapped and denoised, and Figure 5.3 (d) displays a wrapped version of estimated phase shown in (c). For this experiment, we set the prior parameter $\mu = 0.4$ and the potential with exponent $p = 0.4$.

The original absolute phase image displays a vertical discontinuity between the two planes. Thus, from the absolute phase estimation point of view, the two planes correspond to two disconnected images, rendering a hard estimation problem, if no external discontinuity information is used. Assuming that the phase estimation algorithm is able to blindly detect discontinuities, the most we can hope for is to obtain two planes correctly estimated, up to an unknown 2π multiple constant phase difference between them. The proposed algorithm accomplishes that, almost perfectly, without any external discontinuity information. The total root mean square error RMSE $= [(n_1 \text{var}_1 + n_2 \text{var}_2)/(n_1 + n_2)]^{1/2}$, where n_i and var_i are, respectively, the number of pixels and the sample variance of the error regarding the estimated absolute phase surface $i = 1, 2$, is RMSE = 0.14 rad. The improvement in signal to noise ratio, as defined above, is ISNR = 8.99 dB. The number of wrong wrap counts (number of wrong multiples of 2π throughout the image) is 0 (Monte-Carlo simulation).

Figure 5.4 illustrates some more the experiment presented in Figure 5.3. Figure 5.4 (d) displays the discontinuities that the unwrapping step is able to blindly detect. Figure 5.3 (d) shows the re-wrapped image shown in 5.3 (c). As already referred to, the shear discontinuity plus the noise poses a very hard task; it is noticeable the good unwrapping and denoising. Figure 5.4 (a) shows a 3D rendering of the image shown in Figure 5.3 (c); Figure 5.4 (b) shows a corresponding 3D rendering after unwrapping and before denoising. Figure 5.4 (d) shows the descending energy function along the iterations of the

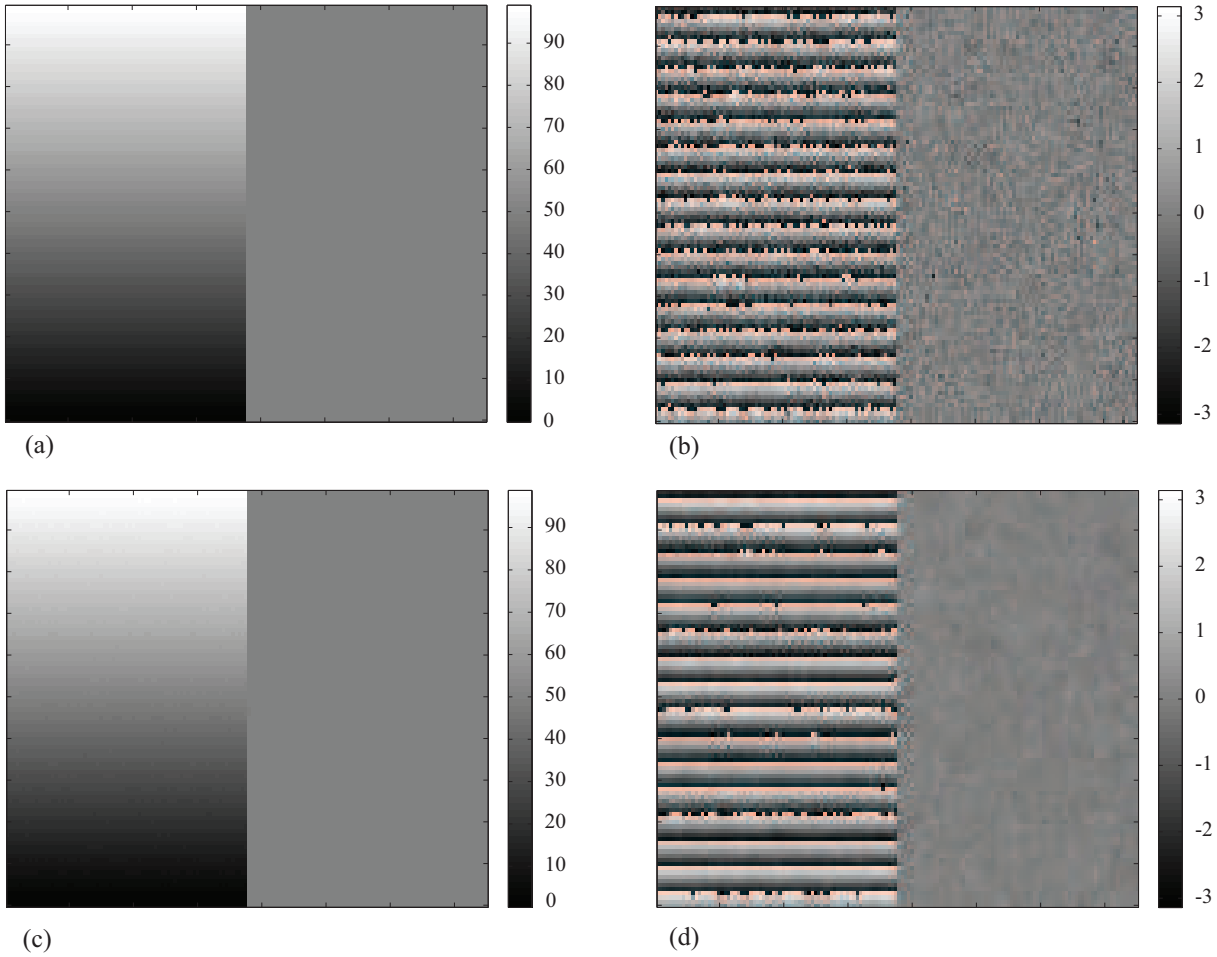

Figure 5.3: (a) Sheared ramp image (99 rad height) (b) Wrapped and noisy image shown in (a). (c) Image in (b) unwrapped and denoised by our algorithm (RMSE = 0.14 rad). (d) Image in (c) re-wrapped.

minimization algorithm.

Figures 5.5 and 5.6 are analogous to Figures 5.3 and 5.4, respectively, but now the original absolute phase surface is a, 100×100 pixels sized, Gaussian elevation with a height of 14π rad and standard deviations $d = 15$ pixels (vertically) and $d = 10$ pixels (horizontally); additionally, in a quarter of the plane the Gaussian has zero height, introducing surface discontinuities. We stress that this is a hard absolute phase estimation problem given these discontinuities plus the noise. For this experiment, we used the prior parameter $\mu = 0.4$ and the potential with exponent $p = 0.4$. The absolute phase estimate shown in Figure 5.5 (c) has RMSE = 0.7 rad and ISNR = 7.85 dB. The number of wrong wrap counts in the image is 20.4 (Monte-Carlo simulation). The obtained reconstruction

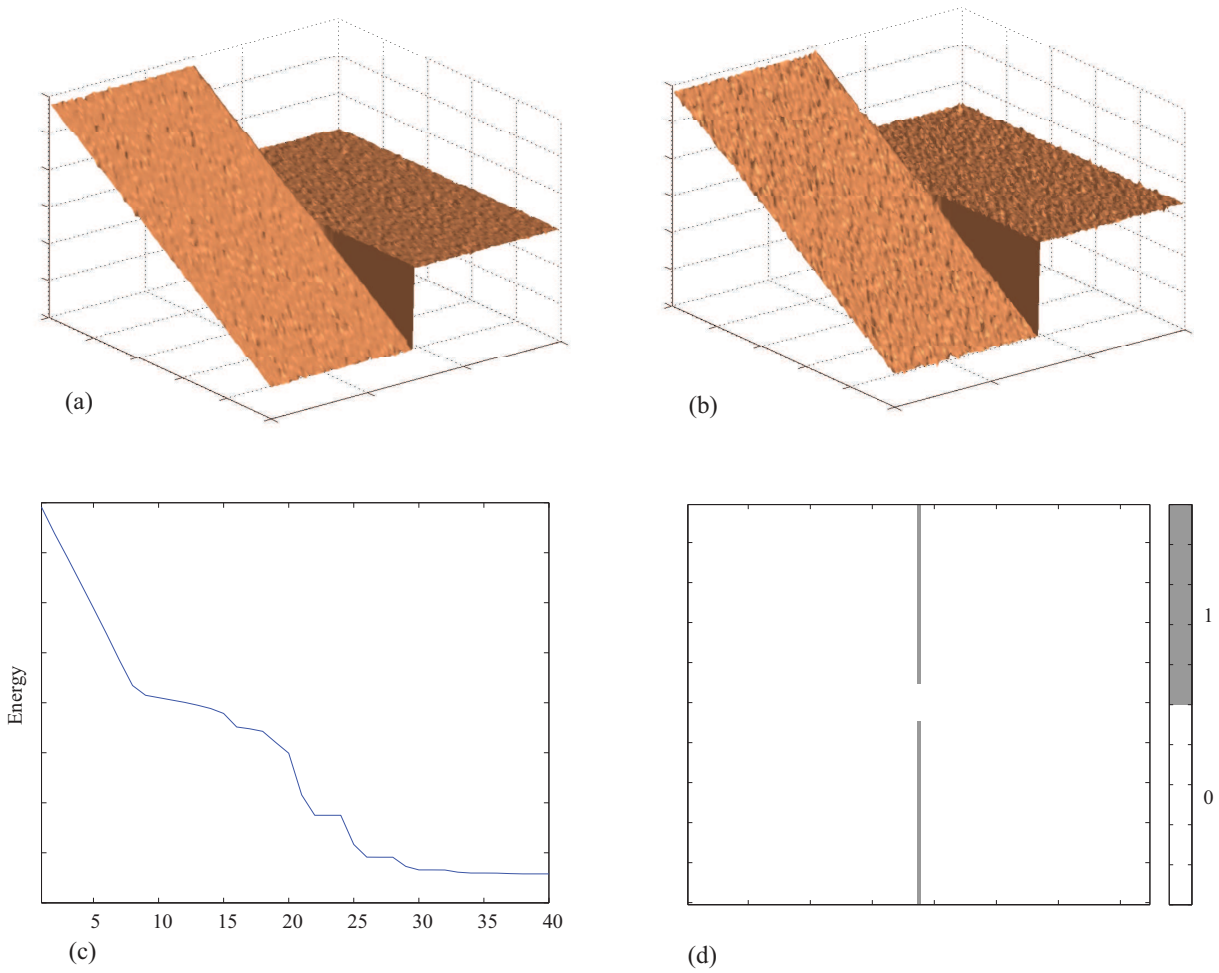

Figure 5.4: This figure illustrates, some more, the experiment presented in Figure 5.3. (a) 3D rendering of image in Figure 5.3 (c). (b) 3D rendering of the image in Figure 5.3 (c) before denoising. (c) energy function evolution along the iterations of the algorithm. (d) discontinuities blindly detected by the algorithm.

is almost perfect.

Contrarily to the shear ramp, there is just one connected component in this example, and then, up to a 2π multiple constant phase, the solution is unique. The reason is that, for a given data mismatch, the adopted potential minimizes the number of discontinuities and any other solution having the same data mismatch would have more discontinuities.

We emphasize that the quarter of the Gaussian having zero height, plus the noise, introduces a lot of discontinuities, which the unwrapping algorithm is able to detect (the algorithm also marks other pixels as discontinuities due to noise plus high phase rate effects) as shown in Figure 5.6 (d). The denoising effect is quite evident in Figure 5.5 (d). The 3D rendering of Figures. 5.5 (a) and 5.5 (b) illustrates the unwrapping plus denoising and unwrapping effects respectively; in 5.6 (c) is shown the evolution of the objective function along with the iterations.

Figures 5.7 and 5.8 are similar to Figures 5.5 and 5.6, respectively, but now the original absolute phase surface is a, 100×100 pixels sized, Gaussian elevation with a height of 14π rad and standard deviations $d = 15$ pixels (vertically) and $d = 10$ pixels (horizontally). For this experiment we used a prior parameter $\mu = 0.4$ and the potential with exponent $p = 2$. We found out better results with such a relatively high exponent p (compared to the p used in the last presented results); this can be explained by the fact that the original surface does not have discontinuities, although it has high phase rates that may create problems when noise is added. Figure 5.5 (c) exhibits an almost perfect unwrapping and RMSE = 0.15 rad. This denoising corresponds to ISNR = 5.74 dB and is quite evident in Figure 5.5 (d) where we show the rewrapped denoised image. The 3D rendering of Figures 5.8 (a) and (b) illustrates the unwrapping [(b)] and unwrapping plus denoising effects [(a)]. In Figure 5.8 (c) we show the evolution of the energy along with the iterations. The number of wrong wrap counts is 0 (Monte-Carlo simulation).

5.4.3 Real data

Finally, we illustrate the performance of the algorithm on a (152×458 pixels) InSAR image (the same as employed in Figure 4.5 in Chapter 4). We have employed a prior parameter $\mu = 0.2$, and a quadratic potential $p = 2$. Figure 5.9 (a) displays an image corresponding to an absolute phase surface generated by a (simulated) InSAR acquisition for a real steep-relief area (Long's Peak, Colorado, USA. Data distributed with book [49]), thus inducing many discontinuities and posing a very hard absolute phase estimation problem.

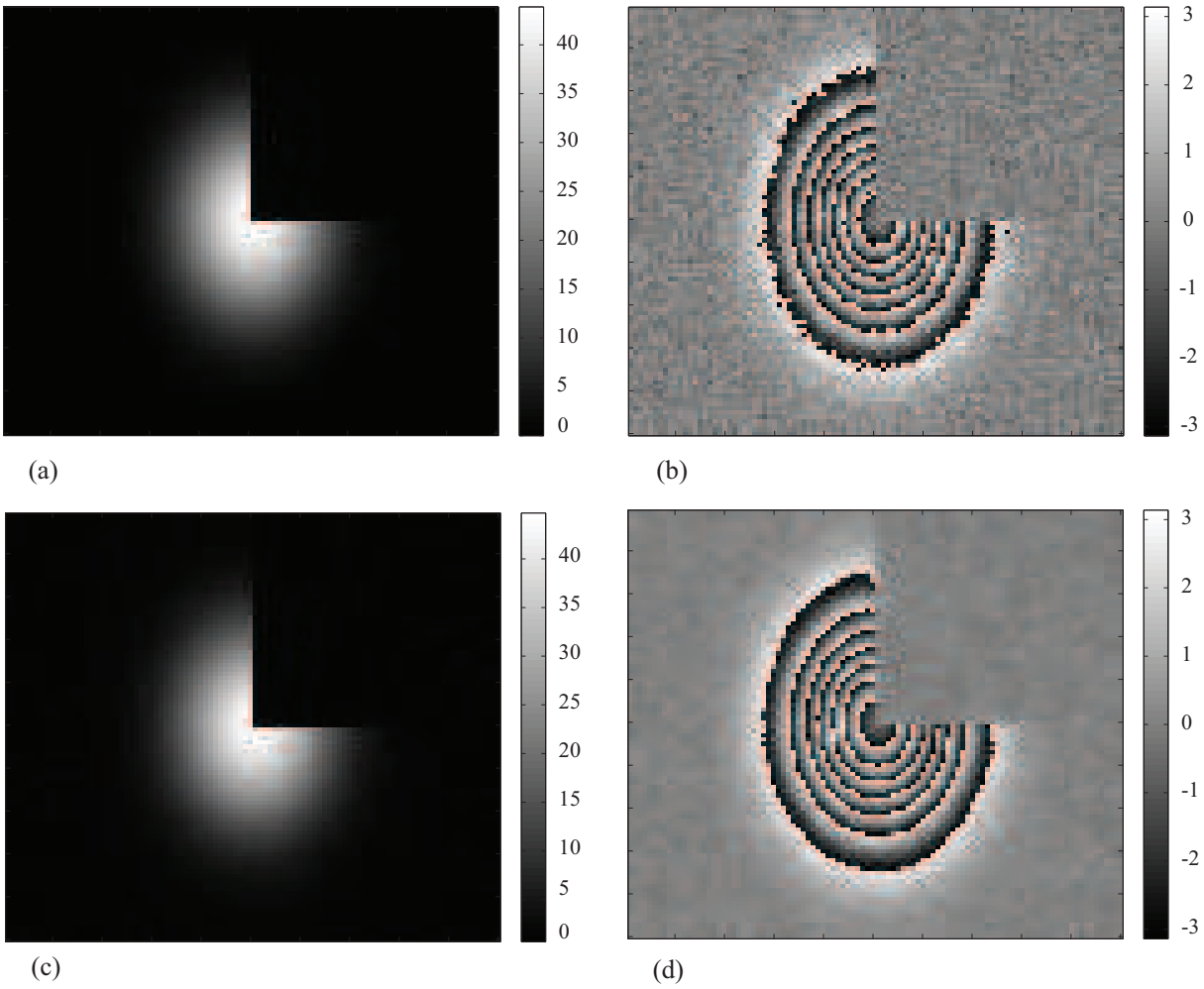

Figure 5.5: (a) Gaussian image with 14π maximum height and with a quarter set to zero. (b) Wrapped and noisy image shown in (a). (c) Image in (b) unwrapped and denoised (RMSE = 0.7 rad). (d) Image in (c) re-wrapped.

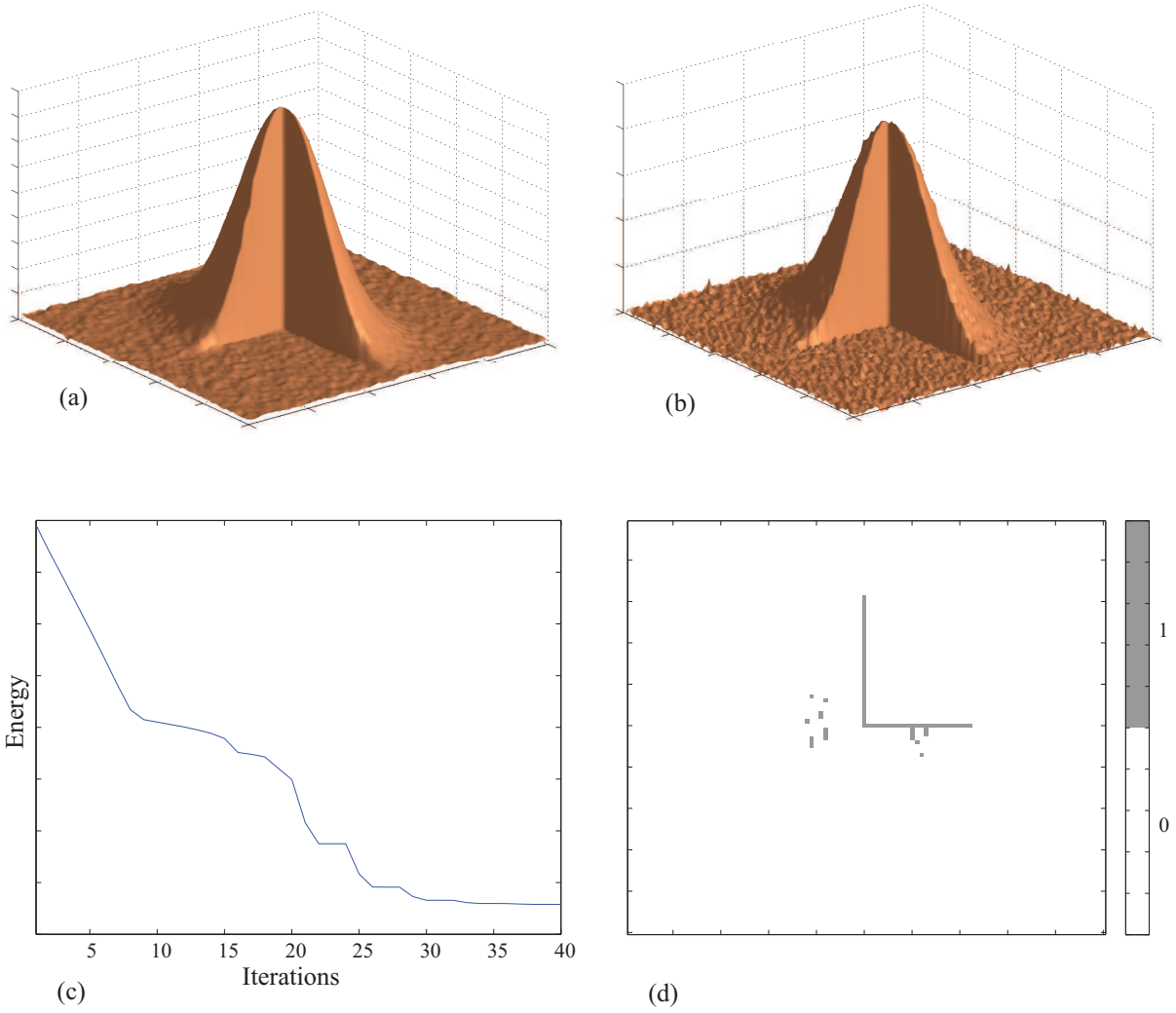

Figure 5.6: This figure illustrates, some more, the experiment presented in Figure 5.5. (a) 3D rendering of the image in Figure 5.5 (c). (b) 3D rendering of the image presented in Figure 5.5 (c) before denoising. (c) Energy evolution along the iterations of the algorithm. (d) Discontinuities blindly detected by the algorithm.

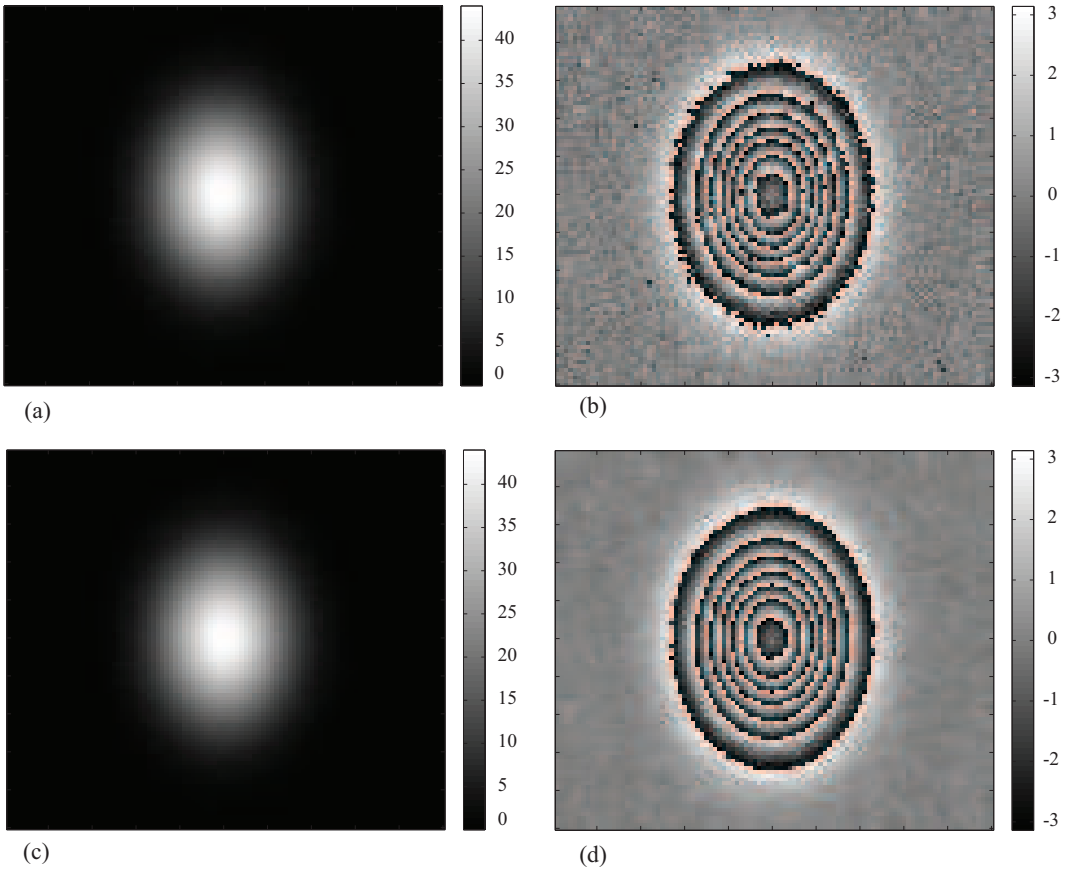

Figure 5.7: (a) Gaussian image with 14π rad maximum height. (b) Wrapped and noisy image shown in (a). (c) Image in (b) unwrapped and denoised (RMSE = 0.15 rad). (d) Image in (c) re-wrapped.

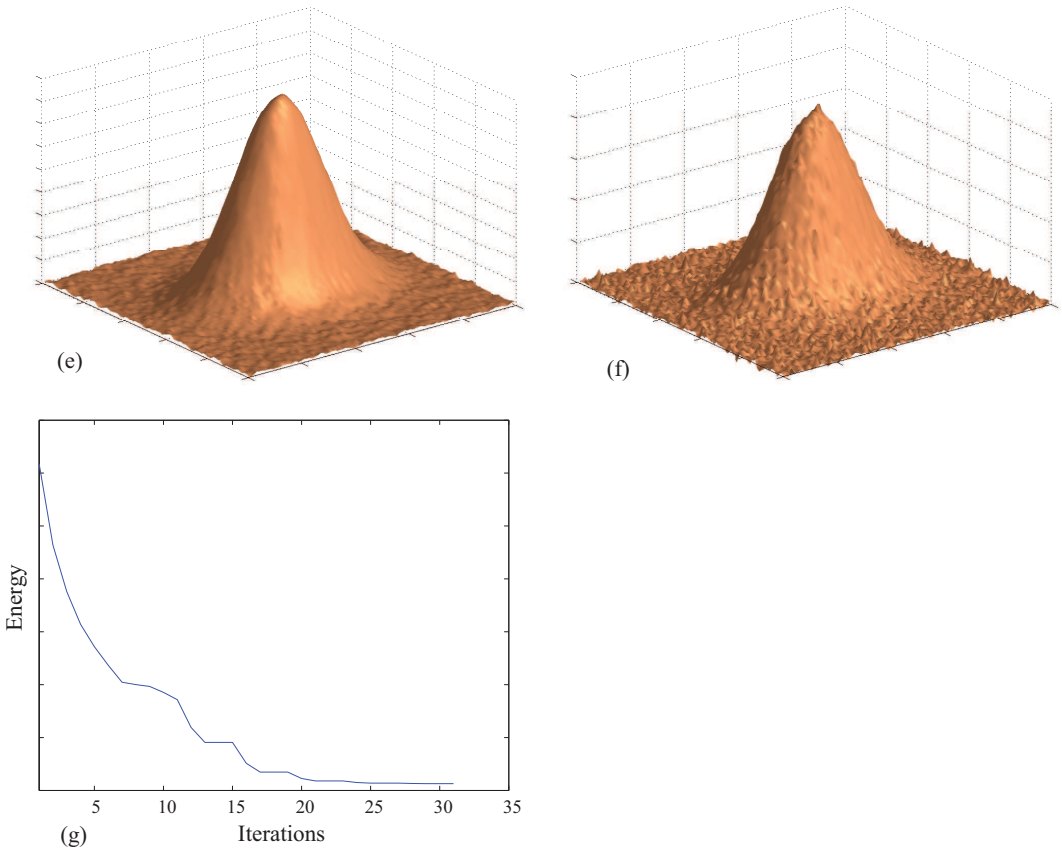

Figure 5.8: (a) 3D rendering of image in Figure 5.7 (c). (b) 3D rendering of the image in Figure 5.7 (c) before denoising. (c) Energy function evolution along the iterations of the algorithm.

Figure 5.9 (b) displays a corresponding wrapped and noisy image. In some areas the characteristic fringes are destroyed due to typical phenomena as shadowing and layover (see, *e.g.*, [49]). Figure 5.9 (f) shows a quality map that is an input to the algorithm: white color corresponds to pixels whose phase value is meaningless and gray corresponds to the rest of the pixels. This information accounts for jamming phenomena such as, the above mentioned, layover and shadowing. PUMA is able to screen those white pixels from the absolute phase estimation process (therefore those pixels do not "contaminate" the results for the rest of the image), and this is the reason why we employ a non discontinuity preserving quadratic potential. Obviously the error values here presented refer only to gray image areas on the quality map (in fact we also do not count with pixels at the border of the gray image, as well as those pixels from the first and the last columns of the image; this is so because such values are outliers driven by data acquisition artifacts). Figure 5.9 (c) shows the unwrapped and denoised resulting image, with RMSE = 0.18 rad corresponding to ISNR = 3.8 dB. Figure 5.9 (d) displays the image in (c) rewrapped. Comparing it with image shown in (b), it is apparent the denoising effect; this is quite clear comparing the zoomed patches in (b) and (d). Figure 5.9 (e) displays a 3D rendering of the image in (c). We further add that the performance took 35 iterations (within Algorithm 3) and we got one wrap-count error.

5.4.4 Benchmarking

In this section, we benchmark the version of PUMA approach introduced in this chapter (Algorithm 3) against the state-of-the-art competitors PEARLS, introduced in [7], and LPN0, presented in [49, Chap.5]. The benchmarks are evaluated on the experiments addressed in the previous sections, with the exception that we run them for a set of noise values $\sigma = \{0.1, 0.3, 0.5\}$ (see Section 3.1 for the definition of σ). We emphasize that we do not benchmark against $\mathbb{Z}\pi$M [36] (algorithm that we have already mentioned above and which is state-of-the-art in absolute phase estimation) because both PEARLS and PUMA can be considered as extensions to it.

Table 5.1 summarizes the quantitative results obtained for the benchmarks. The bullets mean that, for our purposes, that experiment is not relevant. In fact LPN0 aims at achieving (minimum L^0 norm[1]) phase unwrapping (not denoising) and, being so, it is not

[1]Commonly considered as the most desirable minimum L^p norm criterium, in practice, for phase unwrapping purposes.

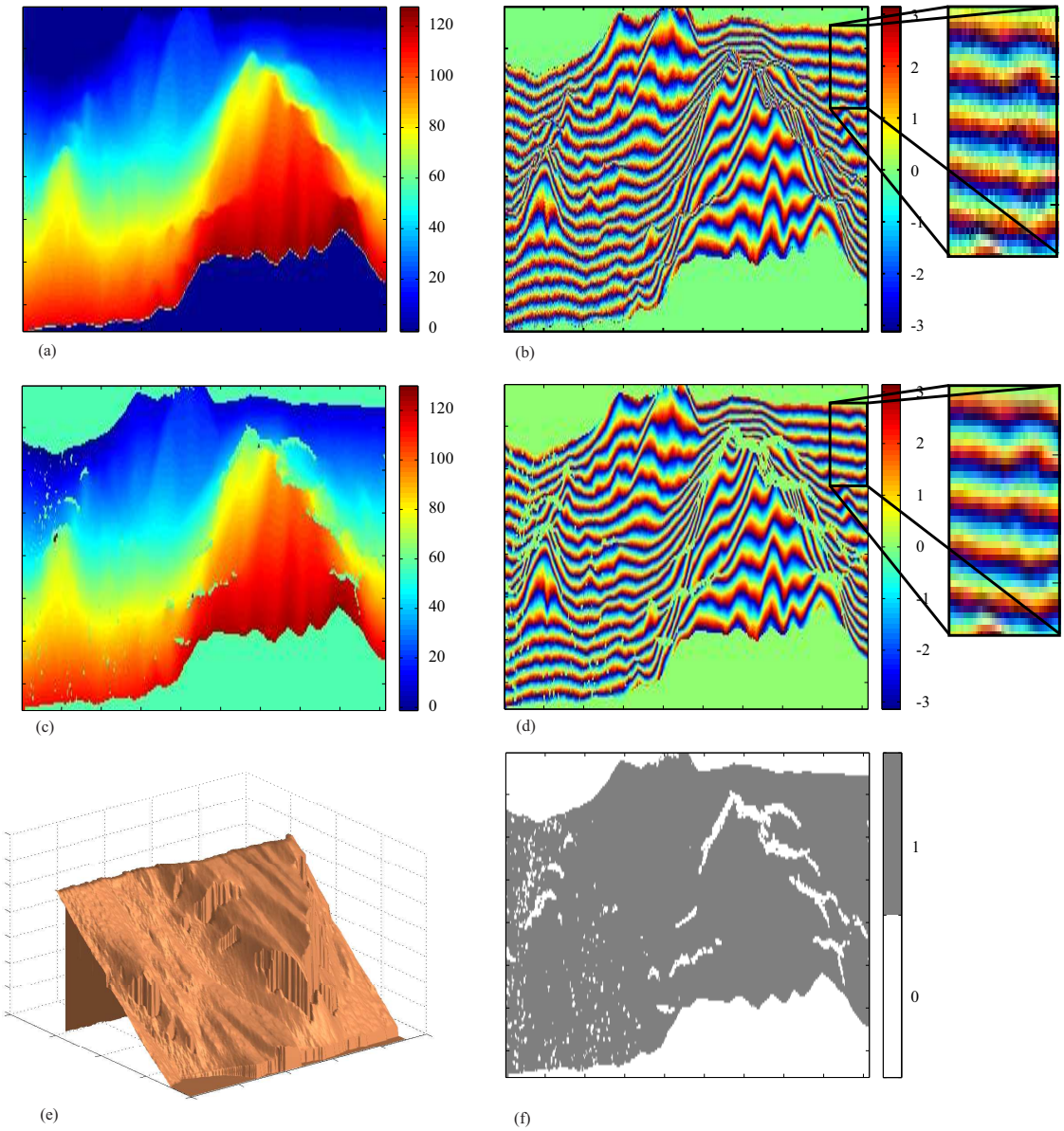

Figure 5.9: (a) Absolute phase gray level image generated by a (simulated) InSAR acquisition for a real steep-relief area. (b) Wrapped and noisy image shown in (a). (c) Image in (b) unwrapped and denoised by our algorithm (RMSE = 0.18 rad). (d) Image in (c) re-wrapped. (e) 3D rendering of the image in (c). (f) Quality map that is an input to the algorithm: white color corresponds to pixels whose phase value is meaningless and gray corresponds to the rest of the pixels.

Table 5.1: Root Mean Square Error (rad).

	Algorithms		
Experiments	PUMA	PEARLS	LPN0
Gaussian			
$\sigma = 0$	0	0	0
$\sigma = 0.1$	0.05	0.05	•
$\sigma = 0.3$	0.11	0.08	•
$\sigma = 0.5$	0.15	0.11	•
Shear Ramp			
$\sigma = 0$	0	0	1.21
$\sigma = 0.1$	0.06	0.07	•
$\sigma = 0.3$	0.10	0.09	•
$\sigma = 0.5$	0.14	0.11	•
Clipped Gaussian			
$\sigma = 0$	0	0	5.48
$\sigma = 0.1$	0.13	0.85	•
$\sigma = 0.3$	0.4	0.90	•
$\sigma = 0.5$	0.7	0.98	•
Long's Peak	0.18	0.20	•

fair to apply it to noisy phase images.

We further add that for noiseless cases ($\sigma = 0$) both PUMA and PEARLS run in the phase unwrapping mode, *i.e.*, PUMA runs as described in [11], and PEARLS also runs as PUMA in this case [7].

We note the following:

1. Both PUMA and PEARLS tend to outperform LPN0 in phase unwrapping ($\sigma = 0$ case) when there exist discontinuities to blindly deal with.

2. PUMA tends to outperform PEARLS when there are discontinuities. As we have previously referred, PEARLS implements a local polynomial approximation (LPA) with varying adaptive neighborhood. This adaptiveness trades bias with variance in such a way that the neighborhood's window stretches in areas where the underlying true phase is smooth and shrinks otherwise, namely in the presence of discontinuities.

It happens that, sometimes, this shrinkage is not enough, implying a few unwrapping errors near these discontinuities. This phenomenon is illustrated in the results for the clipped Gaussian.

3. PEARLS tends to outperform PUMA when there are no discontinuities and the SNR is low. The adaptive window selection technique jointly with LPA results very powerful. This is illustrated in the Gaussian experiment. In the Long's Peak experiment PUMA and PEARLS tend to behave very similarly (the slight difference in favor of PUMA is meaningless because, as we have already referred to, the error is evaluated in a subset of the image, which may have slight differences in the experiments using both PUMA and PEARLS).

To our knowledge PEARLS is a state-of-the-art absolute phase estimation algorithm. From all the held experiments, PUMA can also be considered state-of-the-art. Finally we remark that PUMA has been consistently observed to be quite faster than PEARLS (we should note that, even so, the code is a mix of matlab and C++, therefore is not optimized).

Chapter 6

Frequency Diversity

6.1 Introduction

Frequency diversity is an acquisition strategy where more than one phase image is acquired, each one corresponding to a different frequency of the sinusoidal nonlinearity. By acquiring more than one phase image, the number of absolute phase solutions compatible with the observations decreases and, therefore, the hardness of the phase estimation problem is lightened. Frequency diversity based phase unwrapping algorithms are scarce. We are aware only of the ones presented in [104], [100], and [81] published in 1994, 1998 and 2002, respectively. Regarding the first, [104], it proposes three very simple and appealing algorithms that, nonetheless, are error prone. With respect to the second [100], it is a multidimensional (accounting for multifrequency) version of the minimum L^2 norm type of PU algorithm [49], with relaxation to the continuum that is well-known [49] to give rise to solving a Poisson equation. The weaknesses of this approach are long-familiar, in particular the oversmoothing of high phase rate slopes and discontinuities, which is further amplified by the proposed previous low-pass filtering stage (see [36] for a deeper discussion on this problem). Concerning [81], it consists of an algorithm based on a maximum likelihood estimation technique, whose goal is to approximate the unknown (absolute) surface by means of local planes. The approach assures the uniqueness of the solution, even accounting for high phase rates or discontinuities. However, the global optimization required to compute the maximum likelihood, by suggestion of the authors, is to be achieved by simulated annealing, which is a (nowadays) too much slow optimization technique to tackle this problem, for which, *e.g.*, graph-cuts techniques are much more

suited.

6.2 Diversity

The data model which we consider throughout our work has been introduced in Section 3.1. We recall that it is given by expression (6.1)

$$\begin{aligned} z &= Ae^{jF\phi} + n, \quad A > 0 \\ &= |z|e^{jF(\phi+\phi_n)}, \end{aligned} \tag{6.1}$$

where A is an amplitude, ϕ is the true phase value, $n = n_I + jn_Q$ is a complex-valued zero-mean circular white additive noise, and ϕ_n is the phase due to n. This time we have introduced a constant F, without loss of generality, which has attached to it the meaning of a frequency, namely, the observation frequency. Now we are interested in considering frequency diversity, namely, let us (for the sake of simplicity) consider two frequencies $F_1 = p/q$, $F_2 = r/s$, where $\{p, q, r, s\} \in \mathbb{N}$[1]. Assuming that observations (6.1) are independent for each frequency, and similarly to what we have shown for one frequency only, in Section 3.1, we have that the MAP estimation of the absolute phase is obtained by minimizing the energy

$$E(\phi) \equiv \sum_{i \in \nu} -\lambda_{1_i} \cos\left(\psi_{1_i} - F_1\phi_i\right) - \lambda_{2_i} \cos\left(\psi_{2_i} - F_2\phi_i\right) + \mu \sum_{\{i,j\} \in \mathcal{E}} V\left(\phi_i, \phi_j\right), \tag{6.2}$$

which is analogous to the single frequency energy.

We have referred that with frequency diversity the number of candidates to be the phase estimate decreases. An equivalent statement is that the unambiguity interval $[-\pi, \pi)$ gets extended. Stating it more clearly, it is easy to show that the sum of two cosine functions, having as in (6.2) different frequencies $F_1 = p/q$ and $F_2 = r/s$, where $\{p, q\}$, $\{p, r\}$, $\{q, s\}$, and $\{r, s\}$ are coprime integers[2], results in a third periodic function whose period is $q \times s$; as the initial functions do have periods of respectively q and s, we conclude that the period is, in general, extended and so the ambiguity reduced. Figure 6.1 illustrates this effect by

[1] Rigorously, F_1 and F_2 can be irrational as long as their quotient is rational. However, not considering it does not make any loss of generality in what follows.

[2] Two integer numbers are said to be coprime if their greatest common divisor is the unity.

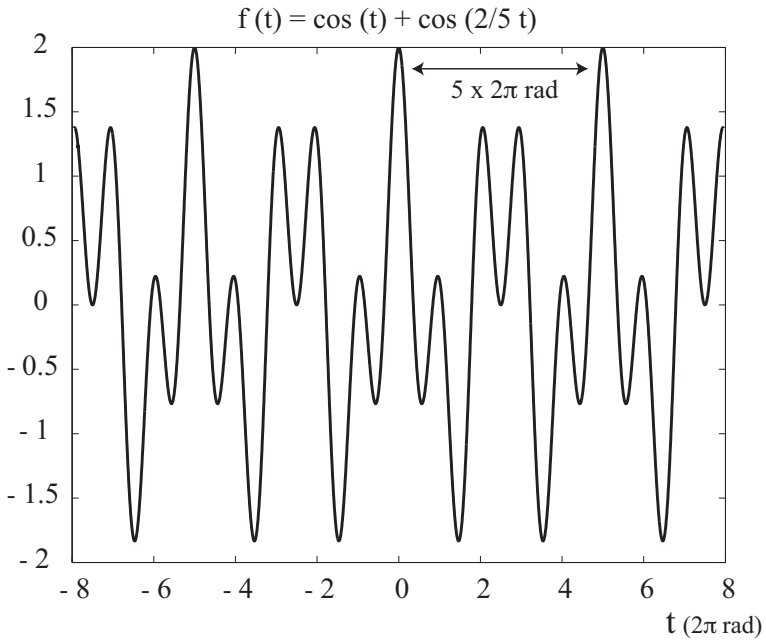

Figure 6.1: Ambiguity reduction by summing two periodic functions: the beat effect.

plotting the function $f(t) = \cos(t) + \cos(2/5\ t),\ t \in [-8\ \ 8]$ with t in 2π rad units. It can be seen that the period has been extended five times (the initial periods were 2π rad and $5 \times 2\pi$ rad). This "beat production", well known in wave physics, can also be understood by the Chinese remainder theorem [59].

It is a well known behavior, *e.g.*, from wave phenomena, that the greater the beat period extension, the smaller the difference between global and local optima. Furthermore, it is also well known that beat period extension brings noise amplification. This trade-off should then be taken into account. We further add that if the requirement of the quotient of F_1 and F_2 to be rational is not met, then the sum of the two cosines will in fact result in a non periodic (namely, quasi-periodic) function. Accordingly, the above referred first side effect will be enhanced (*i.e.*, there will be local optima arbitrarily close to global optima).

6.3 Phase Unwrapping with Diversity

Looking back at (6.2) and analogously to what we have shown for single frequency, if we admit a noiseless environment we may consider that the unwrapped phase ϕ satisfies the constraints:

$$F_1\phi = \psi_1 + 2k_1\pi, \tag{6.3}$$

and

$$F_2\phi = \psi_2 + 2k_2\pi, \tag{6.4}$$

for the two independent observations with frequencies F_1 and F_2, respectively. For the sake of simplicity we can deal with (6.3) only, and (6.2) turns[3] into:

$$\begin{aligned} E(k) &\equiv \sum_{i\in\mathcal{V}} -\cos\left(\psi_{2_i} - \frac{F_2}{F_1}(\psi_{1_i} - 2k_{1_i}\pi)\right) \\ &+ \mu \sum_{\{i,j\}\in\mathcal{E}} V\left(\psi_{1_i} - 2k_{1_i}, \psi_{1_j} - 2k_{1_j}\right), \end{aligned} \tag{6.5}$$

with a correspondingly combinatorial optimization (minimization) to be done on variables k_{1_i}.

Unlike what we have been considering in previous chapters, now the energy has this nonconvex sinusoidal term and, accordingly, PUMA does not apply. We now take $V\left(\psi_{1_i} - 2k_{1_i}, \psi_{1_j} - 2k_{1_j}\right) = |k_i - k_j|$ the, so-called, non-isotropic total variation (TV); in spite of such a potential being convex, which confers some optimization "easiness" (see, *e.g.*, [67] for a nice view on this "easiness" in combinatorial optimization problems), it still has some discontinuity preservability properties.

We are aware of only three approaches, [60], [106], and [29], that are able to provide (in polynomial time) a global minimum for a posterior energy like (6.5), which is composed by a non-convex data fidelity term and a convex prior potential. Herein we refer to [29], as it deals with our non-isotropic TV prior. The authors reformulate, there, the energy in terms of independent binary Markov random fields attached to each level set of the solution (in our case it is the unwrapped image solution). Then, the exact minimization is obtained by using a min cut/max flow algorithm. More precisely, using their notation, they show that the posterior energy may be written as

$$E_{\alpha,v}(\{u^\lambda\}) = E_v(\{u^\lambda\}) + \alpha \sum_{\lambda=0}^{L-2} \sum_s H(u_s^\lambda - u_s^{\lambda+1}), \tag{6.6}$$

where $\boldsymbol{u}$ is the solution image (our $\boldsymbol{\Phi}$), $\boldsymbol{v}$ is the data image (our $\boldsymbol{\Psi}$), $\alpha > 0$ is high enough (see [29]), $u_s^\lambda = \mathbb{1}_{u_s \leq \lambda}$ is the level set image (λ level) at site s, L is the number of levels, H is the heaviside function, and where

$$E_v(\{u^\lambda\}) = \sum_{\lambda=0}^{L-2} \{ \sum_{i=1}^{I} \sum_{\substack{(s,t) \\ \tau(s,t)=i}} R_i(\lambda)|u_s^\lambda - u_t^\lambda| + \sum_s \delta(\lambda, v_s)(1 - u_s^\lambda) \} \tag{6.7}$$

[3] We could have dealt with both observations simultaneously. For simplicity we do not.

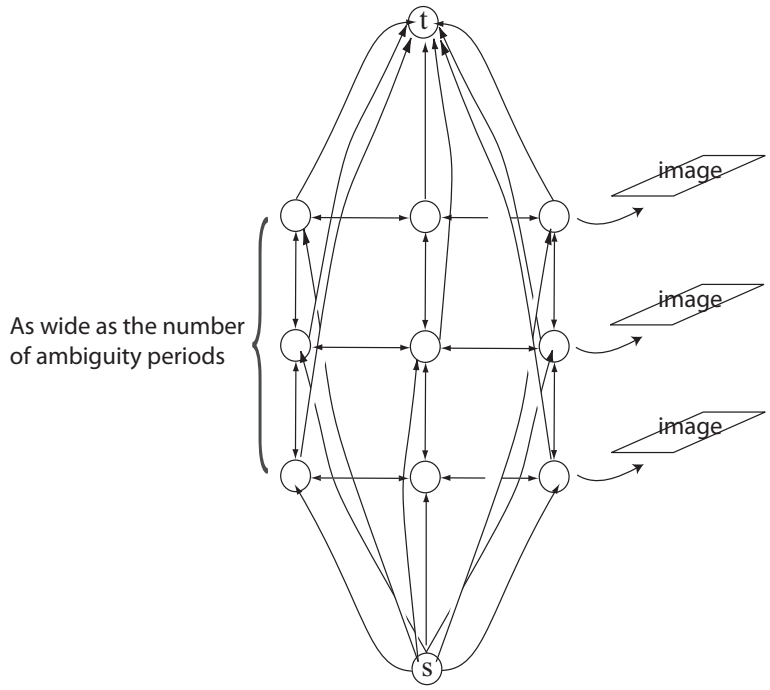

Figure 6.2: Sketch of the graph used to perform phase unwrapping. Toy example.

with (s,t) defining a general clique involving sites s and t, and $\tau(s,t) = i$ determining the size of the clique, and $R_i(\cdot)$ being a positive non decreasing function. Concerning the decomposition on level sets, the original image can be obtained back according to $u_s = \min\{\lambda, u_s^\lambda = 1\}$. Having decomposed the energy as a function of binary variables, the authors then show that it is graph representable and, hence, its global minimum is given by the max flow min cut of the graph built according to the prescription given in [67], which we ourselves used in previous chapters.

Figure 6.2 shows a sketch of the graph obtained for a toy example. We highlight that each node (except source and sink) corresponds to a binary variable (a level set per *layer*), and that there will be as many *image layers* as k_i values in our case. Furthermore, each node besides being linked to the nodes corresponding to its neighboring pixels, is also linked to the node immediately above or beneath, which corresponds to plus one or minus one level set. We should also advert that each node is linked to both source and sink directly, although for simplicity, we do not depict all those edges.

In Subsection 6.4 we present some experimental results where, again, we have used the augmenting path type maxflow/min-cut algorithm proposed in [18], whose worst case complexity is $O(n^2m)$ [4], where n and m are the number of vertices and edges, respectively.

Denoise

For denoising we follow the multiprecision framework that we setup in Chapter 5. So our frequency diversity phase unwrapping plus denoising algorithm is described by the following two lines high level pseudo-code:

Algorithm 4 PUMA (phase unwrapping with frequency diversity plus denoising)

1: Do phase unwrapping with frequency diversity by computing a max-flow/min-cut
2: Do denoising with multi-precision

In the next section we show some relevant experimental results.

6.4 Experimental Results

In this section we briefly illustrate the performance of the above presented algorithm on two representative problems, for which phase unwrapping is a hard task due to high phase rates of the absolute phase images. With these experiments, the important feature that we want to emphasize is frequency diversity and we deal with denoising in a qualitative degree only. We remark that the matlab (mixed with C++) code has been run in a 2.2 GHz Intel dual core processor, in a maximum of few dozens of seconds.

Figure 6.3 (a) displays an image which is given by a Gaussian having maximum height of 50π rad height. Figures 6.3 (b) and (c) show the corresponding wrapped images acquired with frequencies $F_1 = 1/1$ and $F_2 = 1/5$, respectively, and having signal-to-noise ratio (SNR $\equiv 1/\sigma_n^2$) of 4 dB. We note that the Gaussian's height of 50π rad plus the noise turns this into a hard task for which a single frequency approach is not enough. Figure 6.3 (d) displays an image of the unwrapped Gaussian. Figure 6.4 (a) shows a 3-D mesh of the unwrapped image in Figure 6.3 and Figure 6.4 (b) a 3-D mesh after the denoising. It is clear that the algorithm made a perfect phase unwrapping (up to a no-meaning additive constant) for which the diversity information was crucial. The result of the denoising step is reflected in Figures 6.4 (c) and (d), which show the histograms (the axis are in rad) corresponding to the surfaces rendered in Figures 6.4 (a) and (b), respectively. It is noticeable that the denoising erases the secondary modes in the histogram.

Figures 6.5 and 6.6 are similar to Figures 6.3 and 6.4, respectively, but the starting image is a sheared parabolic ramp having maximum height of 225 rad. The frequencies of acquisition are $F_1 = 1/1$ and $F_2 = 1/11$, respectively, and the acquired images have SNR

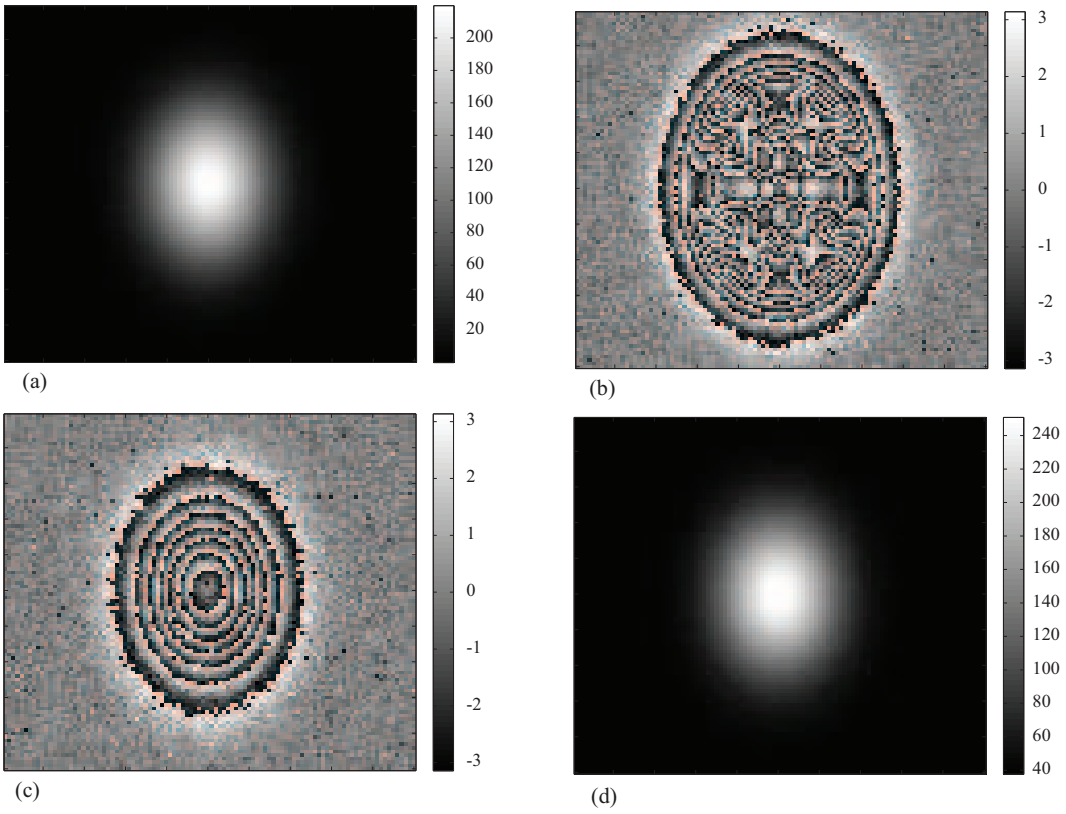

Figure 6.3: (a) Original Gaussian ramp phase image. (b) Image in (a) wrapped with a relative frequency of 1. (c) Image in (a) wrapped with a relative frequency of 1/5. (d) Unwrapped image from the previous wrapped images shown in (b) and (c).

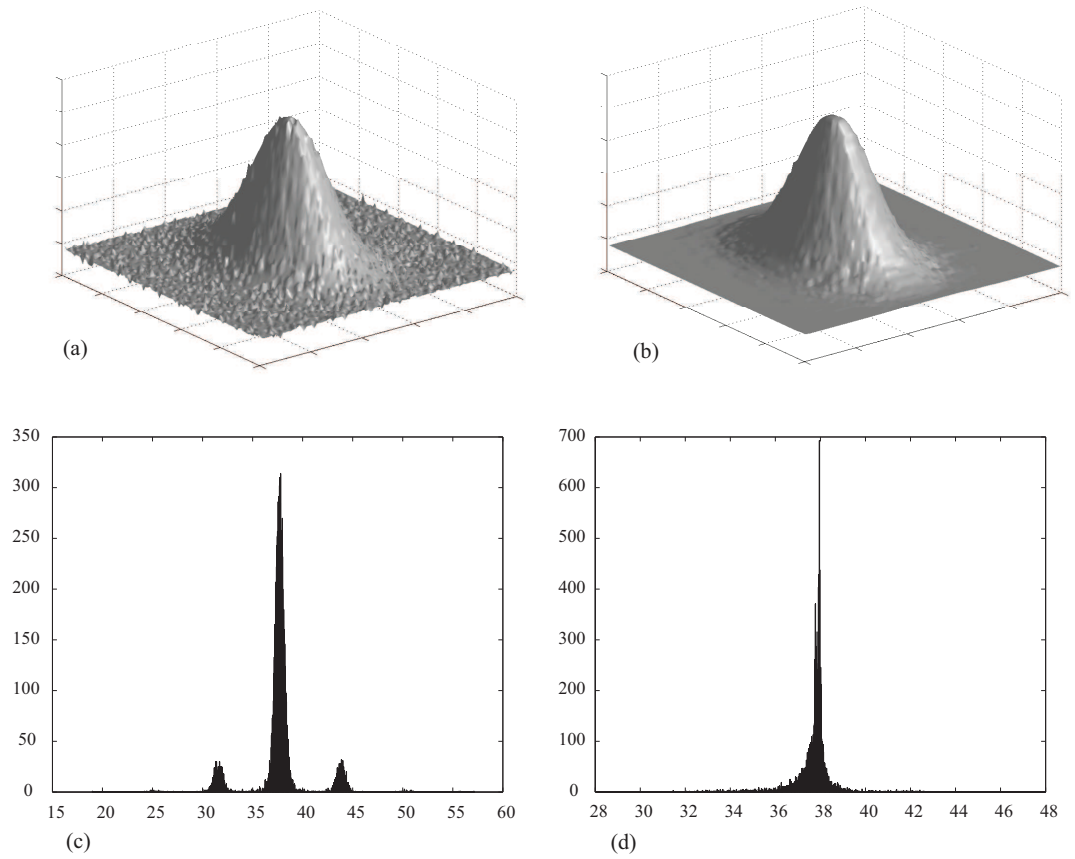

Figure 6.4: (a) 3-D mesh of the image in Figure 6.3 (d). (b) 3-D mesh of the image in Figure 6.3 (d) after the denoising step. (c) Histogram corresponding to the surface rendered in (a). (d) Histogram corresponding to the surface rendered in (b).

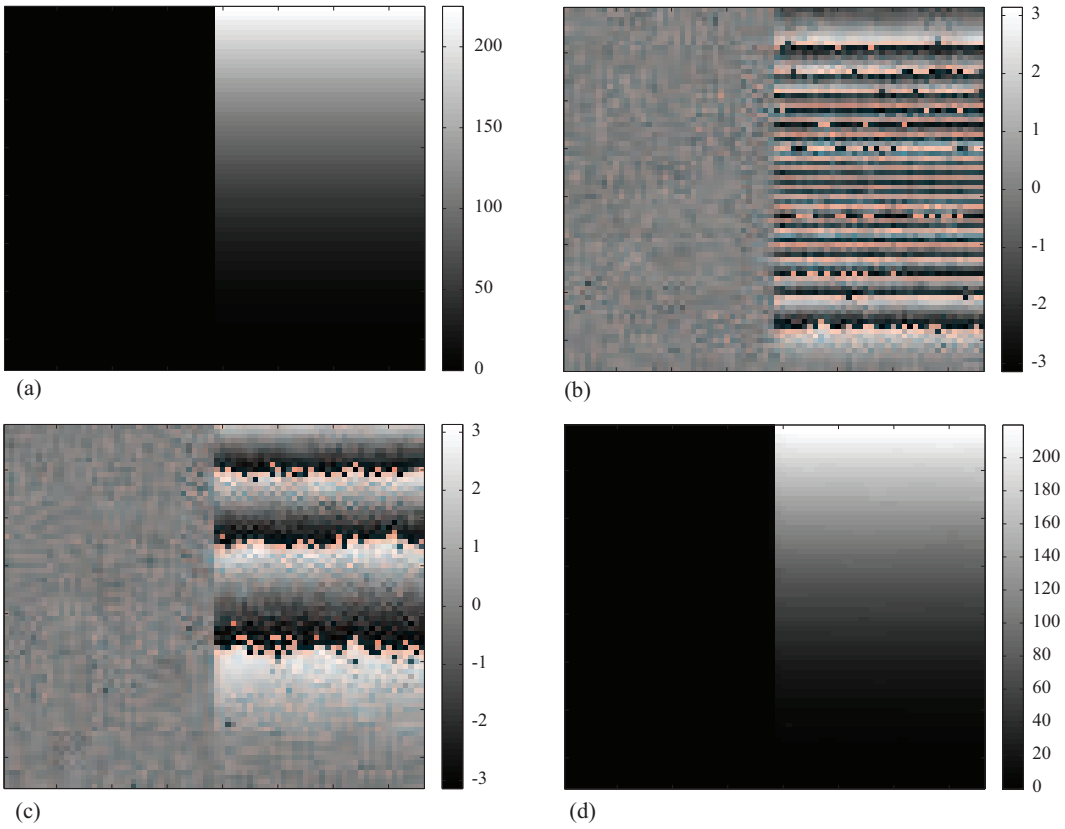

Figure 6.5: (a) Original sheared quadratic ramp phase image. (b) Image in (a) wrapped with a relative frequency of 1. (c) Image in (a) wrapped with a relative frequency of 1/11. (d) Unwrapped image from the previous wrapped images shown in (b) and (c).

= 7 dB. We note that the parabolic's phase rates plus the noise turns phase unwrapping a hard task. Again the algorithm made a perfect phase unwrapping, for which the diversity information was crucial. We emphasize that the unwrapping preserves the discontinuity between the horizontal and the parabolic ramps. Concerning the denoising step, it is noticeable that the denoising erases the secondary modes in the first histogram.

Still referring to the histograms, the ones corresponding to the noisy images show, in general, a multi modal shape. Besides the central mode around zero, there are some modes around multiples of -2π and 2π. Those correspond to "spikes" as a result of the data observation model. After denoising they do disappear.

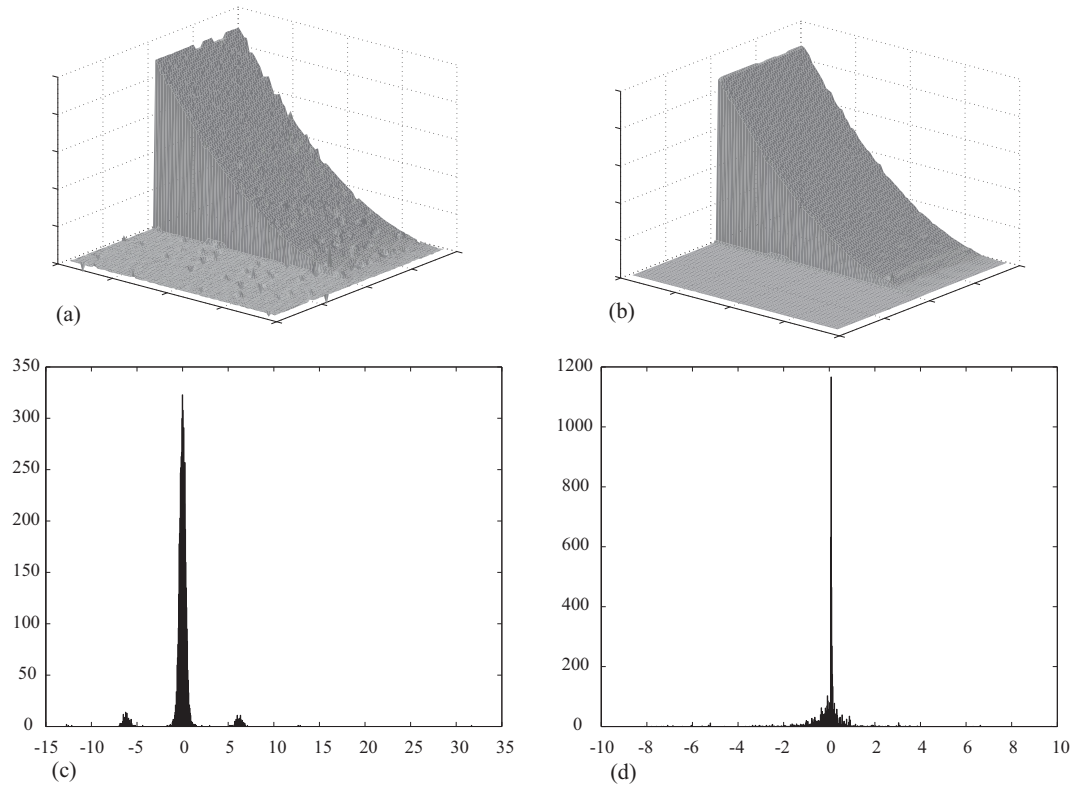

Figure 6.6: (a) 3-D mesh of the image in Figure 6.5 (d). (b) 3-D mesh of the image in Figure 6.5 (d) after the denoising step. (c) Histogram corresponding to the surface rendered in (a). (d) Histogram corresponding to the surface rendered in (b).

Chapter 7

Conclusion

7.1 Summary

In this thesis we have introduced an approach to 2D phase unwrapping which is based on energy minimization. By adopting a MAP-MRF rationale we ended up with an integer minimization problem. Typically, the number of variables of that optimization is high (usually the number of pixels of the images involved), which contributes to make the optimization a hard task. We proposed to solve this optimization problem through a succession of binary minimizations, tackling each one of those binary problems by using graph cuts techniques. We derived a set of low-order pseudo polynomial complexity minimization algorithms, and we have shown the performance of these algorithms to be similar or better than state-of-the-art, or otherwise worthy of note, phase unwrapping algorithms, on representative problems.

7.2 Contributions

Next we list our main contributions.

- A new, state-of-the-art competitive, approach to phase unwrapping. The approach adopts a Bayesian formulation where the prior probability is given by a Markov random field. The maximum *a posteriori* (MAP) computation leads to a discrete energy minimization, for which we propose discrete optimization algorithms based on graph cuts. For convex MRF potentials we prove that the algorithms always yield a global minimum and have a low-order pseudo-polynomial complexity. The

performance of the algorithms is fast in the sense that they can deal with hundreds of thousands or millions of discrete variables to optimize in, at the most, some tens of seconds (by employing a usual laptop) [10, 94, 11].

- Unification of the minimum L^p norm, $p \geq 1$, phase unwrapping problems in the sense that we propose a parametric family of algorithms that solves them exactly. For $p < 1$ we provide approximate algorithms that produce very good results. The proposed algorithms go, nevertheless, beyond minimum L^p norm criteria [9, 8, 95, 11].

- The establishment of approximate phase unwrapping algorithms which are capable to consider non-convex potentials in the MRF. The derived algorithms endow the proposed approach the possibility to blindly detect discontinuities and preserve them. This contribution is specially important since discontinuities play a fundamental role in phase unwrapping, and many times in applications we don't have prior information about their localization [9, 8, 95, 11].

- The introduction of a denoising procedure that shares the same discrete rationale of the phase unwrapping. That denoising is obtained through an extension of the phase unwrapping, by considering smaller steps with which the variables can vary. We adopt a greedy energy minimization given by a sequence of non increasing steps. Every time the energy gets stuck in a minimum we change into a smaller step, and proceed iteratively until a final chosen step is achieved [98, 97, 96].

- Frequency diversity phase unwrapping family of algorithms as a way to extend the unambiguous period $[-\pi, \pi)$ and, accordingly, to deal with higher phase rates in the phase unwrapping tasks. This frequency diversity method is well known, for instance, in radar interferometry. Its fundament can be explained through the chinese remainder theorem [59], according to which a certain number might be deduced from the remainders of the division by two other (certain) numbers [12, 13].

- Development of algorithms that are interesting *per se* and whose usefulness goes beyond the realm of phase unwrapping into other domains such as, *e.g.*, computer vision.

7.3 Future Work

Next we refer to some of the questions which we would like to address in the future:

- Besides graph cuts, there exist other efficient and widely used techniques to perform energy minimization, namely: Loopy Belief Propagation [105] and Tree-reweighted message-passing [101]. We intend to compare their performance in the application of phase unwrapping.

- The proposed algorithms have free parameters, namely, the regularization parameter, the scheduling, and the potentials. As much of the time for effective use of the algorithms is spent in tuning those parameters, it would be of much practical (and theoretical) interest to devise (unsupervised) procedures to learn them. We note here that, for instance, the decision to choose a convex or non-convex potential, when using our approach is to be made by the user, according to some *a priori* knowledge that he might have about the existence (or not) of discontinuities in the wrapped image. This knowledge may be obtained, *e.g.*, by visually inspection of the wrapped image. In the future we will explore this line of research on learning parameters.

- One important question is whether we are able to easily port the proposed approach into 3D, as it is useful for several applications. In the future we will work on our approach for such 3D problems.

- Finally, we would like, in the future, to extend the proposed algorithms in order to consider higher order MRF interactions and, accordingly, to deal with higher phase rates.

Appendix A

Proofs

Proof of Theorem 1

Define $\Delta k_i = [\mathbf{k}_2]_i - [\mathbf{k}_1]_i$, for $i \in \mathcal{V}$. Given that the energy $E(\mathbf{k}|\boldsymbol{\psi})$ depends only on differences between elements of $\mathbf{k}$, we take $\Delta k_i \geq 0$ for $i \in \mathcal{V}$. Define $n = \max_i(\Delta k_i)$ and the wrap-count image sequence $\left\{\mathbf{k}^{(t)}, t = 0, \ldots, n\right\}$, such that $\mathbf{k}^{(0)} = \mathbf{k}_1$, $\mathbf{k}^{(n)} = \mathbf{k}_2$, and

$$k_i^{(t)} = k_i^{(0)} + \min\left(t, \Delta k_i\right), t = 0, \ldots, n. \tag{A.1}$$

The energy variation $\Delta E \equiv E(\mathbf{k}_2|\boldsymbol{\psi}) - E(\mathbf{k}_1|\boldsymbol{\psi})$ can be decomposed as

$$\Delta E \equiv \sum_{t=1}^{n} \underbrace{\left[E(\mathbf{k}^{(t)}|\boldsymbol{\psi}) - E(\mathbf{k}^{(t-1)}|\boldsymbol{\psi})\right]}_{\Delta E^{(t)}}.$$

Since $\Delta E < 0$ by hypothesis, then at least one of the terms $\Delta E^{(t)}$ of the above sum is negative. The theorem is proved if we show that the variation $\delta E^{(t)} \equiv E(\mathbf{k}^{(0)} + \boldsymbol{\delta}^{(t)}|\boldsymbol{\psi}) - E(\mathbf{k}^{(0)}|\boldsymbol{\psi})$ satisfies $\delta E^{(t)} \leq \Delta E^{(t)}$, where $\boldsymbol{\delta}^{(t)} \equiv \mathbf{k}^{(t)} - \mathbf{k}^{(t-1)}$, for any $t = 1, \ldots, n$. This condition is equivalent to

$$0 \leq E(\mathbf{k}^{(t)}|\boldsymbol{\psi}) - E(\mathbf{k}^{(t-1)}|\boldsymbol{\psi}) - E(\mathbf{k}^{0} + \mathbf{k}^{(t)} - \mathbf{k}^{(t-1)}|\boldsymbol{\psi}) + E(\mathbf{k}^{0}|\boldsymbol{\psi}), \tag{A.2}$$

for $t = 1, \ldots, n$. Introducing (3.9) into (A.2), we obtain $0 \leq S$, where

$$S = \sum_{(i,j)\in\mathcal{E}} \left[V\left(\Delta\phi_{ij}^{(t)}\right) - V\left(\Delta\phi_{ij}^{(t-1)}\right) + V\left(\Delta\phi_{ij}^{(0)}\right) - V\left(\Delta\phi_{ij}^{(0)} + \Delta\phi_{ij}^{(t)} - \Delta\phi_{ij}^{(t-1)}\right)\right] d_{ij}, \tag{A.3}$$

where V is the clique potential, and $\Delta\phi_{ij}^{(t)}$ is given by (3.7) computed at the wrap-count image $\mathbf{k}^{(t)}$. To prove (A.2), we now show that the terms of S corresponding to a given edge $(i,j) \in \mathcal{E}$ have positive sum.

The difference $k_i^{(t)} - k_j^{(t)}$, for $t = 0, \ldots, n$, is a monotone sequence. This is a consequence of the definition (A.1): if $\Delta k_i > \Delta k_j$ the sequence is monotone increasing; if $\Delta k_i \leq \Delta k_j$ the sequence is monotone decreasing. Therefore the sequence $\left\{\Delta\phi_{ij}^{(t)}\right\}$, for $t = 0, \ldots, n$, is also monotone. Define $a \equiv \Delta\phi_{ij}^{(0)}$, $b \equiv \Delta\phi_{ij}^{(t-1)}$, and $c \equiv \Delta\phi_{ij}^{(t)}$, and without loss of generality let us assume[1] $a \geq b \geq c$. We will show that the sum of terms of S, corresponding to the edge (i,j), is positive:

$$\begin{aligned} &V(c) - V(b) + V(a) - V(a+c-b) \geq 0 \\ &V(a) + V(c) - V(b) \geq V(a+c-b). \end{aligned} \tag{A.4}$$

By hypothesis, V is convex. Also by hypothesis, $a \geq b \geq c$, so $\exists t \in [0,1] : b = at + c(1-t)$. Thus,

$$V(b) \leq tV(a) + (1-t)V(c) \tag{A.5}$$

$$V(a) + V(c) - V(b) \geq V(a) + V(c) - [tV(a) + (1-t)V(c)] \tag{A.6}$$

$$\geq (1-t)V(a) + tV(c). \tag{A.7}$$

As V is convex, $(1-t)V(a) + tV(c) \geq V[(1-t)a + tc]$. So, from (A.7),

$$V(a) + V(c) - V(b) \geq V[(1-t)a + tc] \tag{A.8}$$

$$\geq V(a + c - \underbrace{[at + c(1-t)]}_{b}) \tag{A.9}$$

$$\geq V(a+c-b). \tag{A.10}$$

■

Proof of Lemma 1

The proof is inspired in the Proposition 3.7 of [27]. The main difference is that the class of energies herein considered does not have unary terms. The implication of this is that our steepest descent algorithm, in each steep, finds a move in the set $\mathcal{B} = \{0,1\}^{|\mathcal{V}|}$,

[1]The only possibilities are either $a \geq b \geq c$ or $a \leq b \leq c$, because the sequence $\left\{\Delta\phi_{ij}^{(t)}\right\}$ is monotone as we have shown.

whereas the presence of unary terms imposes the search in the larger set $\{-1, 0, 1\}^{|\mathcal{V}|}$, as proposed in [27, Chap. 3.3] and in [66].

Define $\mathbf{u} = \mathbf{k}^t$, where $\mathbf{k}^t$ is a minimizer of $E(\cdot|\boldsymbol{\psi})$ on $\mathcal{D}_t$, and $E(\cdot) \equiv E(\cdot|\boldsymbol{\psi})$. Let $\mathcal{M}_{t+1}$ be the set of minimizers of $E(\cdot)$ on $\mathcal{D}_{t+1}$. If $E(\mathbf{v}) = E(\mathbf{u})$ for $\mathbf{v} \in \mathcal{M}_{t+1}$, then $\mathbf{u} \in \mathcal{M}_{t+1}$ and the lemma is proved by choosing $\boldsymbol{\delta} = \mathbf{0}$. Let us then assume that $E(\mathbf{v}) < E(\mathbf{u})$ for $\mathbf{v} \in \mathcal{M}_{t+1}$. We proceed by contradiction supposing that $\mathbf{v} - \mathbf{u} \notin \mathcal{B}$, for any (at least one) $\mathbf{v} \in \mathcal{M}_{t+1}$, *i.e.*, for some $\mathbf{v} \in \mathcal{M}_{t+1}$ there exists at least one site $i \in \mathcal{V}$ such that

$$v_i - u_i \notin \{0, 1\}. \tag{A.11}$$

Given $\mathbf{u} \in \mathcal{M}_t$ and $\mathbf{v} \in \mathcal{M}_{t+1}$, define image $\mathbf{h}$ with $h_i = 1$ if $v_i - u_i > 0$ and zero elsewhere. At least one element of $\mathbf{v}$ takes the value $t + 1$ and all elements of $\mathbf{u}$ are less ou equal to t. Therefore, we have $\mathbf{h} \neq \mathbf{0}$.

Since $E(\cdot)$ is a linear combination of convex terms, each one depending only on a difference of two components, then a reasoning based on (A.4) leads to

$$E(\mathbf{u}) - E(\mathbf{v} - \mathbf{h}) \geq E(\mathbf{u} + \mathbf{h}) - E(\mathbf{v}).$$

The right hand side of the above inequality is nonnegative, for $\mathbf{v}$ is a global minimizer in $\mathcal{D}_{t+1}$. If $E(\mathbf{u} + \mathbf{h}) = E(\mathbf{v})$, hypothesis (A.11) would be contradicted because $\mathbf{v} - \mathbf{u} \in \mathcal{B}$. We have then

$$E(\mathbf{u}) > E(\mathbf{v} - \mathbf{h}).$$

But $\mathbf{v} - \mathbf{h} \in \mathcal{D}_t$. To verify this, let us analyse the differences $v_i - h_i$, having in mind that $h_i \in \{0, 1\}$ and $0 < v_i \leq t + 1$. If $v_i = t + 1$, then $h_i = 1$ and $v_i - h_i = t$. Otherwise, $v_i - h_i \leq t$. Then $\mathbf{v} - \mathbf{h} \in \mathcal{D}_t$, contradicting the fact that $\mathbf{u}$ is a global minimizer of E on $\mathcal{D}_t$. This ends the proof.

■

Proof of Theorem 2

For the precision interval Δ, the pseudo code embraced by the "**while**" loop (lines between 2 and 19) finds a minimizer of $E(\phi)$ in $\left\{\phi \in \mathbb{R}^{|\mathcal{V}|} : \phi_i = \phi' + z_i\Delta,\ z_i \in \mathbb{Z}\right\}$, where ϕ' is the minimizer obtained in the previous precision. Proofs are given in Chapter 3, in the absence of unary terms, and in [66], [27], for the general case, *i.e.*, when E contains unary and pairwise terms. Since the successive precisions are powers of (1/2), we

can write $\phi'_i = \psi_i + l_i\Delta$, where ϕ'_i and ψ_i are the ith components of ϕ' and ψ, respectively, and l_i is an integer. Therefore, it follows that $\left\{\phi \in \mathbb{R}^{|\mathcal{V}|} : \phi_i = \phi' + z_i\Delta,\ z_i \in \mathbb{Z}\right\} = \left\{\phi \in \mathbb{R}^{|\mathcal{V}|} : \phi_i = \psi_i + z_i\Delta,\ z_i \in \mathbb{Z}\right\}$.

■

Bibliography

[1] R. Ahuja, T. Magnanti, and J. Orlin, *Network Flows: Theory, Algorithms and Applications*. Prentice Hall, 1993.

[2] S. Arashloo and J. Kittler, "Pose-invariant face matching using mrf energy minimization framework," in *EMMCVPR*, 2009, pp. 56–69.

[3] S. T. Barnard, "Stochastic stereo matching over scale," *International Journal of Computer Vision*, vol. 3, no. 1, pp. 17–32, 1989.

[4] D. Bertsekas, *Network Optimization: Continuous and Discrete Models*. Athena-Scientific, 1998.

[5] J. Besag, "Spatial interaction and the statistical analysis of lattice systems," *Journal of the Royal Statistical Society, Series B*, vol. 36, pp. 192–236, 1974.

[6] ——, "On the statistical analysis of dirty pictures (with discussion)," *Journal of the Royal Statistical Society, Series B*, pp. 259–302, December 1986.

[7] J. Bioucas-Dias, V. Katkovnik, J. Astola, and K. Egiazarian, "Absolute Phase Estimation: Adaptive Local Denoising and Global Unwrapping," *Applied Optics*, 2008.

[8] J. Bioucas-Dias and G. Valadão, "Discontinuity preserving phase unwrapping using graph cuts," in *Energy Minimization Methods in Computer Vision and Pattern Recognition-EMMCVPR'05*, A. Rangarajan, B. Vemuri, and A. Yuille, Eds., vol. 3757. York: Springer, 2005, pp. 268–284.

[9] ——, "Phase unwrapping: A new max-flow/min-cut based approach," in *Proceedings of the IEEE International Conference on Image Processing – ICIP'05*, 2005.

[10] ——, "Phase unwrapping via graph cuts," in *Proceedings of the Second Iberian Conference - IbPRIA2005*, vol. 1, Estoril, Portugal, June 2005, pp. 360–367.

[11] ——, "Phase unwrapping via graph cuts," *IEEE Transactions on Image Processing*, vol. 16, no. 3, pp. 698–709, March 2007.

[12] ——, "Phase unwrapping via diversity and graph cuts," in *Proceedings of the IWSSIP 2008 (15th International Workshop on Signals, Systems and Image Processing*, Bratislava, Slovak Republic, June 2008.

[13] ——, "Multifrequency absolute phase estimation via graph cuts," in *Proceedings of the 17th European Signal Processing Conference - EUSIPCO2009*, Glasgow, Scotland, August 2009.

[14] A. Blake and A. Zisserman, *Visual Reconstruction*. Cambridge, M.A.: MIT Press, 1987.

[15] M. Born and E. Wolf, *Principles of Optics*. Wiley-Interscience, 1970, pp. 260–261.

[16] C. Bouman and K. Sauer, "A generalized Gaussian image model for edge-preserving MAP estimation," *IEEE Transactions on Image Processing*, vol. 2, no. 3, pp. 296–310, July 1993.

[17] Y. Boykov and M.-P. Jolly, "Interactive graph cuts for optimal boundary and region segmentation of objects in n-d images," in *Eighth International Conference on Computer Vision (ICCV 2001)*, Vancouver, 2001, pp. 105–112.

[18] Y. Boykov and V. Kolmogorov, "An experimental comparison of min-cut/max-flow algorithms for energy minimization in vision," *IEEE Transactions on Pattern Analysis and Machine Intelligence*, vol. 26, no. 9, pp. 1124–1137, 2004.

[19] Y. Boykov, O. Veksler, and R. Zabih, "Markov random fields with efficient approximations," in *Proceedings of the IEEE Computer Society Conference on Computer Vision and Pattern Recognition - CVPR'98*, 1998, pp. 648–655.

[20] ——, "Fast approximate energy minimization via graph cuts," *IEEE Transactions on Pattern Analysis and Machine Intelligence*, vol. 23, no. 11, pp. 1222–1239, 2001.

[21] C. Chen, "Statistical-cost network-flow approaches to two-dimensional phase unwrapping for radar interferometry," Ph.D. dissertation, Stanford University, 2001.

[22] C. Chen and H. Zebker, "Network approaches to two-dimensional phase unwrapping: intractability and two new algorithms," *Journal of the Optical Society of America*, vol. 17, no. 3, pp. 401–414, 2000.

[23] J. Cordeiro and J. Dias, "Contour estimation on piecewise homogeneous random fields," in *First International Conference on Enterprise Information Systems, ICEIS'99*, 1999, pp. 184–194.

[24] M. Costantini, "A novel phase unwrapping method based on network programing," *IEEE Transactions on Geoscience and Remote Sensing*, vol. 36, no. 3, pp. 813–821, May 1998.

[25] G. Crow, E. Crow, and M. Crow, *Statistics Manual*. Courier Dover Publications, 1960.

[26] R. Cusack, J. Huntley, and H. Goldrein, "Improved noise-immune phase unwrapping algorithm," *Applied Optics*, vol. 34, no. 5, pp. 781–789, 1995.

[27] J. Darbon, "Composants logiciels et algorithmes de minimisation exacte d'énergies dédiés au traitement des images," Ph.D. dissertation, Ecole Nationale Supérieure des Télécommunications, 2005.

[28] J. Darbon and M. Sigelle, "Image restoration with discrete constrained total variation part I: Fast and exact optimization," *Journal of Mathematical Imaging and Vision*, 2006.

[29] ——, "Image restoration with discrete constrained total variation part II: Levelable functions, convex priors and non-convex cases," *Journal of Mathematical Imaging and Vision*, pp. 277–291, 2006.

[30] J. Darbon, "Global optimization for first order markov random fields with submodular priors," *Discrete Applied Mathematics*, vol. 157, no. 16, pp. 3412–3423, 2009.

[31] J. Darbon and M. Sigelle, "A fast and exact algorithm for total variation minimization," in *IbPRIA (1)*, 2005, pp. 351–359.

[32] M. Datcu and G. Palubinskas, "Multiscale bayesian height estimation from insar using a fractal prior," in *SAR Image Analysis, Modelling, and Techniques, Proceedings of the SPIE*. Bellingham, WA: Society of Photo-Optical Instrumentation Engineers, 1998, pp. 155–163.

[33] B. de Senneville, C. Mougenot, B. Quesson, I. Dragonu, N. Grenier, and C. Moonen, "MR thermometry for monitoring tumor ablation," *European Radiology*, vol. 17, no. 9, pp. 2401–2410, 2007.

[34] D. Derauw, "Phase unwrapping using coherence measurements," *Synthetic Aperture Radar and Passive Microwave Sensing, Proceedings SPIE*, vol. 2584, pp. 319–324, 1995.

[35] A. Devaney, "Diffraction tomographic reconstruction from intensity data," *IEEE Transactions on Image Processing*, vol. 1, no. 2, pp. 221–228, 1992.

[36] J. Dias and J. Leitão, "The $\mathbb{Z}\pi$M algorithm for interferometric image reconstruction in SAR/SAS," *IEEE Transactions on Image Processing*, vol. 11, pp. 408–422, April 2002.

[37] J. Dias and J. Leitão, "Simultaneous phase unwrapping and speckle smoothing in SAR images: A stochastic nonlinear filtering approach," in *EUSAR'98 European Conference on Synthetic Aperture Radar*, Friedrichshafen, May 1998, pp. 373–377.

[38] P. Ferrari, M. Gubitoso, and E. Neves, "Reconstruction of gray-scale images," *Methodology and Computing in Applied Probability*, vol. 3, pp. 255–270, 2001.

[39] A. Ferretti, C. Prati, and F. Rocca, "Permanent scatterers in SAR interferometry," *IEEE Trans. Geosci. Remote Sens.*, vol. 39, no. 1, pp. 8–20, 2001.

[40] T. Flynn, "Consistent 2-D phase unwrapping guided by a quality map," in *Proceedings of the 1996 International Geoscience and Remote Sensing Symposium-IGARSS'96*, vol. 4, Lincoln, NE, 1996, pp. 2057–2059.

[41] ——, "Two-dimensional phase unwrapping with minimum weighted discontinuity," *Journal of the Optical Society of America A*, vol. 14, no. 10, pp. 2692–2701, 1997.

[42] D. Fried, "Least-squares fitting a wave-front distortion estimate to an array of phase-difference measurements," *Journal of the Optical Society of America*, vol. 67, no. 3, pp. 370–375, 1977.

[43] B. Friedlander and J. Francos, "Model based phase unwrapping of 2-D signals," *IEEE Transactions on Signal Processing*, vol. 44, no. 12, pp. 2999–3007, 1996.

[44] M. Garey and D. Johnson, *Computers and Intractability : A Guide to the Theory of NP-Completeness*, ser. Series of Books in the Mathematical Sciences. New York: W. H. Freeman, 1979.

[45] S. Geman and D. Geman, "Stochastic relaxation, Gibbs distribution, and Bayesian restoration of images," *IEEE Trans. Pattern Anal. Machine Intell.*, vol. 6, pp. 721–741, 1984.

[46] S. Geman and D. McClure, "Statistical methods for tomographic image reconstruction," in *Proceedings of the* 46^{th} *Session of the International Statistical Institute*. Bulletin of the ISI, Vol. 52, 1987, pp. 353–356.

[47] R. Gens, "Two-dimensional phase unwrapping for radar interferometry: developments and new challenges," *International Journal of Remote Sensing*, vol. 24, no. 4, pp. 703–710, 2003.

[48] D. Ghiglia, G. Mastin, and L. Romero, "Cellular automata method for phase unwrapping," *Journal of the Optical Society of America*, vol. 4, no. 1, pp. 267–280, 1987.

[49] D. Ghiglia and M. Pritt, *Two-dimensional phase unwrapping: theory, algorithms, and software (hardcover)*. Wiley-Interscience, 1998.

[50] D. Ghiglia and L. Romero, "Robust two-dimensional weighted and unweighted phase unwrapping that uses fast transforms and iterative methods," *Journal of the Optical Society of America A*, vol. 11, pp. 107–117, 1994.

[51] G. Glover and E. Schneider, "Three-point dixon technique for true water/fat decomposition with inhomogeneity correction," *Magnetic Resonance Medicine*, vol. 18, pp. 371–383, 1991.

[52] A. Goldberg and R. Tarjan, "A new approach to the maximum-flow problem," *Journal of the Association for Computing Machinery*, vol. 35, no. 4, pp. 921–940, October 1988.

[53] R. Goldstein, H. Zebker, and C. Werner, "Satellite radar interferometry: two-dimensional phase unwrapping," in *Symposium on the Ionospheric Effects on Communication and Related Systems*, vol. 23. Radio Science, 1988, pp. 713–720.

[54] D. Greig, B. Porteous, and A. Seheult, "Exact maximum a posteriory estimation for binary images," *Jounal of Royal Statistics Society B*, vol. 51, no. 2, pp. 271–279, 1989.

[55] W. E. L. Grimson and T. Pavlidis, "Discontinuity detection for visual surface reconstruction," *Computer Vision, Graphics, and Image Processing*, vol. 30, no. 3, pp. 316–330, 1985.

[56] J. Hadamard, "Sur les problèmes aux dérivées partielles et leur signification physique," *Princeton University Bulletin*, no. 13, 1902.

[57] R. Hudgin, "Wave-front reconstruction for compensated imaging," *Journal of the Optical Society of America*, vol. 67, no. 3, pp. 375–378, 1977.

[58] J. Huntley, "Noise-immune phase unwrapping algorithm," *Applied Optics*, vol. 28, no. 15, pp. 3268–3270, 1989.

[59] K. Ireland and M. Rosen, *A Classical Introduction to Modern Number Theory, 2nd ed.* Springer-Verlag, 1990.

[60] H. Ishikawa, "Exact optimization for Markov random fields with convex priors," *IEEE Transactions on Pattern Analysis and Machine Intelligence*, vol. 25, no. 10, pp. 1333–1336, October 2003.

[61] H. Ishikawa and D. Geiger, "Segmentation by grouping junctions," in *IEEE Conference on Computer Vision and Pattern Recognition (CVPR)*, 1998.

[62] K. Itoh, "Analysis of the phase unwrapping problem," *Applied Optics*, vol. 21, no. 14, 1982.

[63] C. Jakowatz, D. Wahl, P. Eichel, D. Ghiglia, and P. Thompson, *Spotlight-Mode Synthetic Aperture Radar: A Signal Processing Approach.* Boston: Kluwer Academic Publishers, 1996.

[64] V. Katkovnik, J. Astola, and K. Egiazarian, "Phase local approximation (phasela) technique for phase unwrap from noisy data," *IEEE Transactions on Image Processing*, vol. 17, no. 6, pp. 833–846, 2008.

[65] S. Kirkpatrick, C. Gelatt, and M. Vecchi, "Optimization by Simulated Annealing," *Science*, vol. 220, 4598, no. 4598, pp. 671–680, 1983.

[66] V. Kolmogorov, "Primal-dual Algorithm for Convex Markov Random Fields," Microsoft Research, Cambridge, UK, Tech. Rep., 2005.

[67] V. Kolmogorov and R. Zabih, "What energy functions can be minimized via graph cuts?" *IEEE Transactions on Pattern Analysis and Machine Intelligence*, vol. 26, no. 2, pp. 147–159, February 2004.

[68] L. Rudin, S. Osher, and E. Fatemi, "Nonlinear total variation based noise removal algorithm," *Physica D.*, vol. 60, pp. 259–268, 1992.

[69] K. Lange, *Optimization.* New York: Springer Verlag, 2004.

[70] J. Leitão and M. Figueiredo, "Absolute phase image reconstruction: A stochastic non-linear filtering approach," *IEEE Transactions on Image Processing*, vol. 7, no. 6, pp. 868–882, June 1997.

[71] S. Li, *Markov random field modeling in computer vision.* Secaucus, NJ: Springer-Verlag New York, 1995.

[72] ——, *Markov random field modeling in image analysis.* New York: Springer-Verlag, 2001.

[73] H. Lim, W. Xu, and X. Huang, "Two new practical methods for phase unwrapping," in *Proceedings of the 1995 International Geoscience and Remote Sensing Symposium-IGARSS'95*, 1995, pp. 196–198.

[74] ——, "Two new practical methods for phase unwrapping," in *Proccedings of the 1995 International Geoscience and Remote Sensing Symposium-IGARSS'95*, Firenze, Italy, 1995, pp. 196–198.

[75] B. Mercer and Q. Zhang, "Recent advances in airborne InSAR for 3D applications," in *The International Archives of the Photogrammetry, Remote Sensing and Spatial Information Sciences. Vol. XXXVII. Part B1*, Beijing, China, 2008.

[76] K. Murota, *Discrete Convex Analysis.* Philadelphia: Society for Industrial and Applied Mathematics, 2003.

[77] M. Nikolova, "Analysis of the recovery of edges in images and signals by minimizing nonconvex regularized least-squares," *SIAM Journal on Multiscale Modeling and Simulation*, vol. 4, pp. 960–991, 2005.

[78] P. Orbanz, S. Braendle, and J. Buhmann, "Bayesian order-adaptive clustering for video segmentation," in *EMMCVPR*, 2007, pp. 334–349.

[79] P. Kohli, "Minimizing dynamic and higher order energy functions using graph cuts," Ph.D. dissertation, Oxford Brookes University, 2007.

[80] R. Palmer, T. Yu, and P. Chilson, "Range imaging using frequency diversity," *Radio Science*, vol. 34, no. 6, pp. 1485–1496, 1999.

[81] V. Pascazio and G. Schirinzi, "Multifrequency insar height reconstruction through maximum likelihood estimation of local planes parameters," *IEEE Transactions on Image Processing*, vol. 11, pp. 1478–1489, December 2002.

[82] A. Patil and P. Rastogi, "Moving ahead with phase," *Optics and Lasers in Engineering*, vol. 45, no. 2, pp. 253–257, 2007, guest Editorial.

[83] C. Prati, M. Giani, and N. Leuratti, "SAR interferometry: A 2-D phase unwrapping technique based on phase and absolute values information," in *Proceedings of the 1990 International Geoscience and Remote Sensing Symposium-IGARSS'90*, 1990, pp. 2043–2046.

[84] B. Reddy, *Introductory Functional Analysis*, ser. Texts in Applied Mathematics Series. New York: Springer-Verlag, 1997, vol. 27.

[85] J. Reichenbach, M. Essig, E. Haacke, W. K. B. Lee, C. Przetak, and L. Schad, "High-resolution venography of the brain using magnetic resonance imaging," *Magnetic Resonance Materials in Physics, Biology and Medicine*, vol. 6, no. 1, pp. 62–69, August 1998.

[86] M. Rivera and J. Marroquin, "Half-Quadratic Cost Functions for Phase Unwrapping," *Optics Letters*, vol. 29, no. 5, pp. 504–506, 2004.

[87] W. Rockward, A. Thomas, B. Zhao, and C. DiMarzio, "Quantitative phase measurements using optical quadrature microscopy," *Appl. Opt.*, vol. 47, no. 10, pp. 1684–1696, 2008.

[88] M. Roth, "Phase unwrapping for interferometric SAR by the least-error path," Johns Hopkins University Applied Physics Lab Technical Report, Laurel, MD, Tech. Rep., 1995.

[89] L. Rudin, "Images, numerical analysis of singularities and shock filters," California Institute of Technology, Pasadena, CA, USA, Tech. Rep., 1987.

[90] J. Rydell, H. Knutsson, J. Pettersson, A. Johansson, G. Farnebäck, O. Dahlqvist, P. Lundberg, F. Nyström, and M. Borga, "Phase sensitive reconstruction for water/fat separation in MR imaging using inverse gradient," in *Medical Image Computing and Computer-Assisted Intervention – MICCAI 2007*, ser. Lecture Notes in Computer Science, vol. 4791/2007, 2007, pp. 210–218.

[91] G. Sansoni and E. Redaelli, "A 3D vision system based on one-shot projection and phase demodulation for fast profilometry," *Measurement Science and Technology*, vol. 16, pp. 1109–1118, 2005.

[92] R. Szeliski, R. Zabih, D. Scharstein, O. Veksler, V. Kolmogorov, A. Agarwala, M. F. Tappen, and C. Rother, "A comparative study of energy minimization methods for Markov random fields with smoothness-based priors," *IEEE Trans. Pattern Anal. Mach. Intell.*, vol. 30, no. 6, pp. 1068–1080, 2008.

[93] D. Terzopoulos, "Regularization of inverse visual problems involving discontinuities," *IEEE Trans. Pattern Anal. Mach. Intell.*, vol. 8, no. 4, pp. 413–242, 1986.

[94] G. Valadão and J. Bioucas-Dias, "Phase unwrapping via graph cuts," in *Global Developments in Environmental Earth Observation from Space: 25th EARSEL Symposium - EARSEL2005*, Porto, Portugal, 2005.

[95] ——, "Puma: Phase unwrapping via max flows," in *Proceedings of the 6th Conference on Telecommunications - ConfTele2007*, Peniche, Portugal, May 2007.

[96] ——, "Cape: Combinatorial absolute phase estimation," *Journal of the Optical Society of America A*, vol. 26, no. 9, pp. 2093–2106, 2009.

[97] ——, "Phase imaging: Unwrapping and denoising with diversity and multi-resolution," in *Proceedings of the 7th Conference on Telecommunications - ConfTele2009*, Santa Maria da Feira, Portugal, May 2009.

[98] G. Valadão and J. Bioucas-Dias, "Phase imaging: Unwrapping and denoising with diversity and multi-resolution," in *LNLA 2008, the International Workshop on Local and Non-Local Approximation in Image Processing*, August 2008, pp. 205–212.

[99] O. Veksler, "Efficient graph-based energy minimization methods in computer vision," Ph.D. dissertation, Cornell University, 1999.

[100] M. Vinogradov and I. Elizavetin, "Phase unwrapping method for the multifrequency and multibaseline interferometry," in *Proceedings of the 1998 International Geoscience and Remote Sensing Symposium-IGARSS'98*, vol. 2, Seattle, WA, USA, 1998, pp. 1103–1105.

[101] M. J. Wainwright, T. Jaakkola, and A. S. Willsky, "Map estimation via agreement on trees: message-passing and linear programming," *IEEE Transactions on Information Theory*, vol. 51, no. 11, pp. 3697–3717, 2005.

[102] T. Walker and J. Walker, *Fourier Analysis*. Oxford University Press US, 1988.

[103] Z. Wu and R. Leahy, "An optimal graph theoretic approach to data clustering: Theory and its application to image segmentation," *IEEE Transactions on Pattern Analysis and Machine Intelligence*, vol. 15, no. 11, pp. 1101–1113, November 1993.

[104] W. Xu, E. Chang, L. Kwoh, H. Lim, and W. Heng, "Phase-unwrapping of sar interferogram with multi-frequency or multi-baseline," in *Proceedings of the 1994 International Geoscience and Remote Sensing Symposium-IGARSS'94*, vol. 2, 1994, pp. 730–732.

[105] J. S. Yedidia, W. T. Freeman, and Y. Weiss, "Generalized belief propagation," in *NIPS*, 2000, pp. 689–695.

[106] B. Zalesky, "Efficient determination of gibbs estimators with submodular energy functions," *arXiv:math/0304041*, 2003.